The Masses of the Neutron Stars in Cen X-3 and Vela X-1.

Thesis

UNRESTRICTED

The Masses of the Neutron Stars in Cen X-3 and Vela X-1.

Timothy David Curtis Ash, B.Sc., M.Sc.

Submitted for the degree of Doctor of Philosophy

Department of Physics

The Open University

DATE OF SUBMISSION: 16 MARCH 1999

DATE OF AWARD: 25 JUNE 1999

Contents

Abstract

This thesis deals with observations, and subsequent analysis made of the high-mass X-ray binary systems Cen X-3 and Vela X-1. By making precise radial velocity measurements of the supergiant components, and combining these results with previous X-ray data, the masses of the neutron star components can be determined. The mass of the neutron star in Cen X-3 is found to be $1.21 \pm 0.21 M_{\odot}$, while the mass of the neutron star in Vela X-1 is found to be $1.77^{+0.55}_{-0.29} M_{\odot}$. The thesis concludes with an account of an attempt to detect radio emission from the Vela X-1 bowshock.

List of Figures

List of Tables

Acknowlegements

First off, I'd like to thank Andy Norton and Paul Roche, my supervisors, Jocelyn Bell Burnell and Sarah Unger, my examiners, and thanks to Starlink for giving me a job. I'd also like to thank Rich, office-mate and drinking partner for three long years, as well as Pete, Rob, Mark, Diana, Hannah, No-Teeth, Matt, Big Chris, Mond, Dippy and Natalie. Thanks to Mum, Dad, Granny, and my brother Chris (for encouraging me to imbibe near-fatal amounts of alcohol). Thanks also to Tom, Ingrid, Andy the landlord, Matthew, Simon, Iru Bru, Red Bull, Henekien, Mark Thomas, Jello Biafra, James Randi, Pam Spam, and Bod. I'd also like to take this opportunity to apologise to all the guests at Rob and Linda's wedding. Lastly, special thanks to Kaz and Ollie Octopus.

Chapter 1

Introduction

"When people are asleep, we must all become alarm clocks."

Jello Biafra; The Power of Lard

1.1 Thesis Layout

The first chapter of this thesis consists of a discussion of the historical background to X-ray binaries, a description of the various types of system, a discussion of the importance of neutron star masses, and an explanation of the techniques used to make the radial velocity measurements required. It concludes with a discussion of the various methods of neutron star mass determination, and the obtained values. The second and third chapters contain accounts of the optical observations made of Cen X-3 and Vela X-1, the data reduction and analysis, and the results that were obtained. The fourth chapter consists of an account of radio observations made of the Vela X-1 bowshock. The fifth and final chapter contains the conclusions drawn, and suggests directions for future work.

1.2 Historical Background

On the 18th June 1962, an Aerobee rocket carrying a payload of three large area Geiger counters took off from White Sands Missile Range in New Mexico. The experiment was intended to study fluorescence X-rays produced on the lunar surface by stellar radiation, and to explore the sky for any other X-ray sources. However, it is alleged that the lunar studies were simply a ruse to secure funding from an establishment galvanised by the then President Kennedy's famous "man on the moon" pronoucement. An X-ray source, now known as Sco X-1, was detected with a flux of 5 photons $cm^{-2}s^{-1}$. The authors suggested

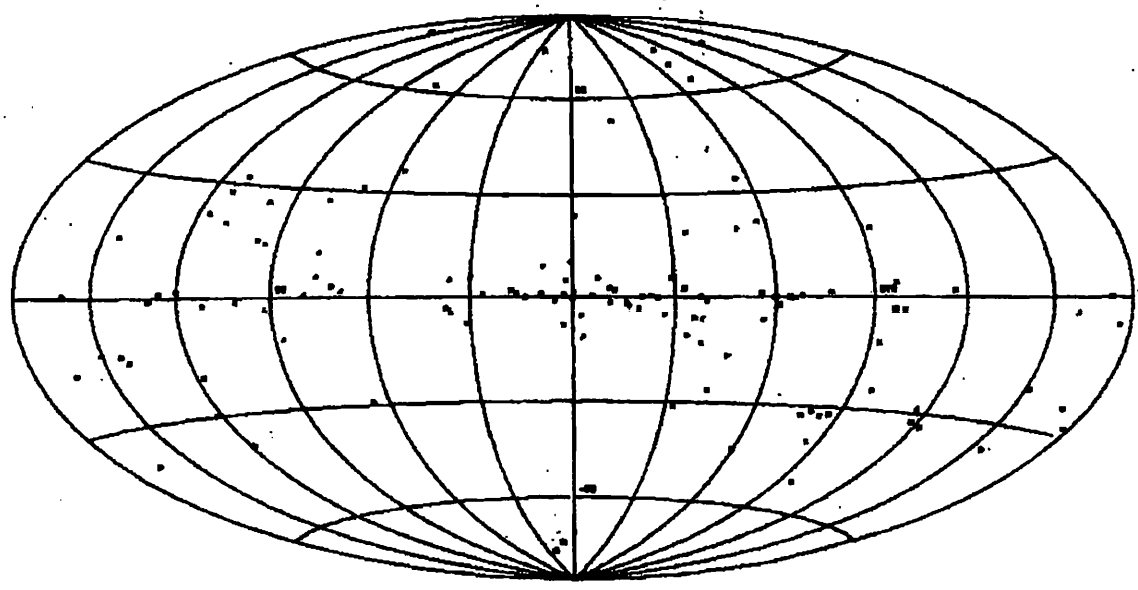

Figure 1.1 Whole-sky map showing the various X-ray sources detected by Uhuru (from Giacconi et al 1972)

synchrotron emission as a possible mechanism for the production of the X-rays, but also noted that ordinary stellar sources could contribute a significant fraction of the observed radiation (Giacconi et al 1962).

Further rocket flights were made and in December 1970, the first satellite-borne detector, the Small Astronomical Satellite 1 (SAS-1) was launched, from a platform off the coast of Kenya. It was later renamed Uhuru, Swahili for "freedom" in honour of being launched on Kenyian Independence Day. Uhuru performed the first complete X-ray survey of the sky (Giacconi et al 1972), and detected over 300 X-ray sources before the mission ended in March 1973.

The rapid rate of progress is this field is illustrated by the ROSAT satellite, which was launched in June 1990, less than twenty years after the launch of Uhuru. ROSAT's mission began with a six-month all-sky survey, during which approximately 10^5 X-ray sources were detected. ROSAT actually detected more X-ray sources in the Andromeda galaxy than Uhuru detected in the whole sky!

It was proposed that a possible mechanism for X-ray emission was mass transfer in a stellar binary system which contained a compact object. This hypothesis was supported by the identification of optical counterparts to two X-ray sources, Sco X-1 (Sandage et al 1966), and Cyg X-2 (Giacconi et al 1967), by their ultraviolet excess. The optical spectrum of Sco X-1 was similar to those of systems known to be binaries, namely old novae and U Gem type stars, while that of Cyg X-2 was found to consist of a late-type star and a highly-excited component.

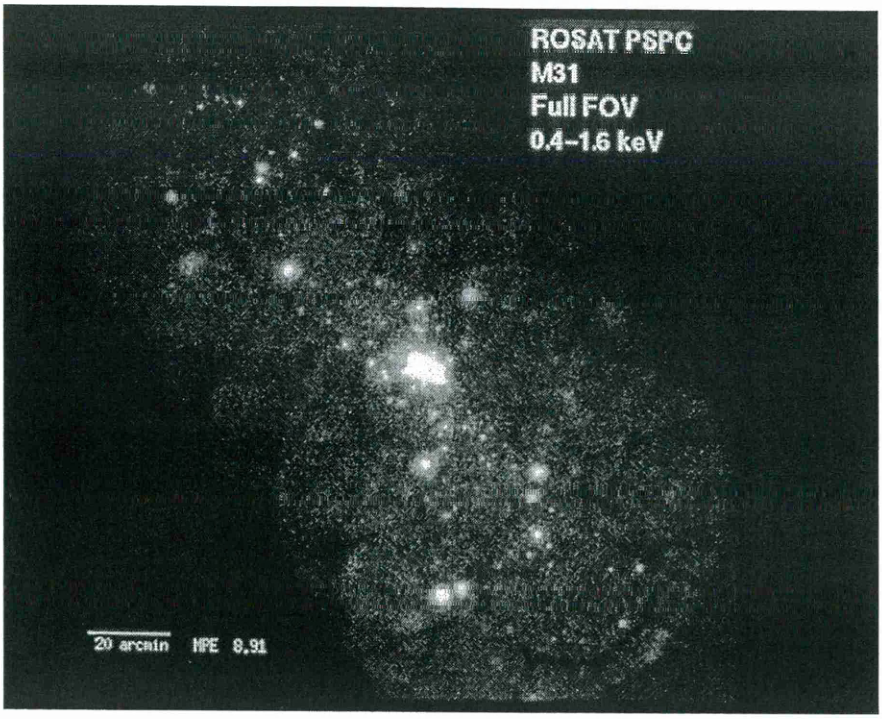

Figure 1.2 ROSAT image of the M31 galaxy, showing a number of X-ray sources.

The process of discovering the first X-ray binary began when Hjellming & Wade (1972) and Braes & Miley (1972) detected a radio source which appeared to be associated with the X-ray source Cyg X-1. The accurate position of this radio source allowed Rappaport et al (1972) to determine the position of Cyg X-1 to a precision of $\sim 30''$ with a rocket-borne rotating X-ray modulation collimator. The X-ray and radio emission were both coincident with the optical star HD226868, a B0Ib supergiant. Optical spectra of HD226868 showed that the system had a period of 5.6 days, and a radial velocity semi-amplitude of ~ 65 kms^{-1} (Webster & Murdin 1972, Bolton 1972). Assuming that the supergiant was of normal mass, $\geq 15 M_{\odot}$, the conclusion was that the compact star in Cyg X-1 had a mass of $\geq 3 M_{\odot}$. This value was greater then the theoretical maximum mass of a neutron star (Rhoades & Ruffini 1972), and led to speculation that the X-ray binary Cyg X-1 contained a black hole.

Meanwhile, another important discovery was taking place. A source which emitted regular radio pulses with a period of 1.337s had been detected at the Mullard Radio Astronomy Observatory by Hewish et al (1968). This pulsing star, or pulsar, was thought to be a rapidly rotating neutron star which was emitting tightly beamed radiation. The appearance of pulsing was due to a "lighthouse effect" as the beam swept over the observer. This discovery was quickly followed by the detection of 33ms pulsations from the Crab Nebula at soft (Boldt et al 1969, Fritz et al 1971), and hard (Fishman et al 1969) X-ray energies, as well

as in the optical, infra-red, and radio regions (see Nagase 1989).

The Crab pulsar is now known to be an isolated neutron star with a strong magnetic field located in a young supernova remnant. The discovery of the first X-ray pulsar was in turn followed by the observation, in Cen X-3, of the first X-ray pulsar in an X-ray binary (Giacconi et al 1971, Schreier et al 1972). The pulse period of 4.8s varied sinusoidally over a period of around two days, due to Doppler-shifting caused by the orbital motion of the pulsar, and X-ray eclipses were observed as the pulsar moved behind its massive companion. A small number of similar systems such as Her X-1 (Tananbaum et al 1972) and Vela X-1 (McClintock et al 1976) have subsequently been discovered. As will be demonstrated later, these eclipsing, pulsing X-ray binaries are extremely important as they allow the masses of the binary components to be directly measured.

1.3 Origin and Evolution of X-Ray Binaries

An X-ray binary consists of either a neutron star or a black hole accreting material from a companion star. The X-ray emission is powered by the potential energy released as the material from the companion falls down the gravitational well of the compact object. Generally, X-ray binaries fall into one of two groups, depending on the mass of the compact object's companion. The high mass X-ray binaries (HMXRBs) are systems in which the mass of the companion is greater than around $10M_{\odot}$, while low mass X-ray binaries (LMXRBs) are systems in which the companion is less massive than around $1M_{\odot}$ (see review by Verbunt & van den Heuvel 1995). The systems can also be classified on the basis of their ratio of X-ray to optical luminosity (Bradt & McClintock 1983). The value of L_x/L_o, where the energy range for L_x is 2-10keV, and the wavelength range for L_o is 3000-7000 Å, is $\leq$10 for a HMXRB, while it is $\geq$10 for a LMXRB. A third means of distinguishing between the two groups is by age. HMXRBs are relatively young population I objects, and are generally found in the galactic disc, while LMXRBs are older population II objects and tend to be found in the galactic bulge and globular clusters.

Figure 1.2 shows the various groups and subgroups of X-ray binaries. These will be discussed in more detail below.

1.3.1 HMXRBs

High mass X-ray binaries can be divided into two sub-groups. The "classical" HMXRBs, such as Cen X-3 and Vela X-1, consist of an OB supergiant (mass $\geq 20M_{\odot}$) in close orbit with a neutron star companion. With the exception of GX301-2, these systems have orbital

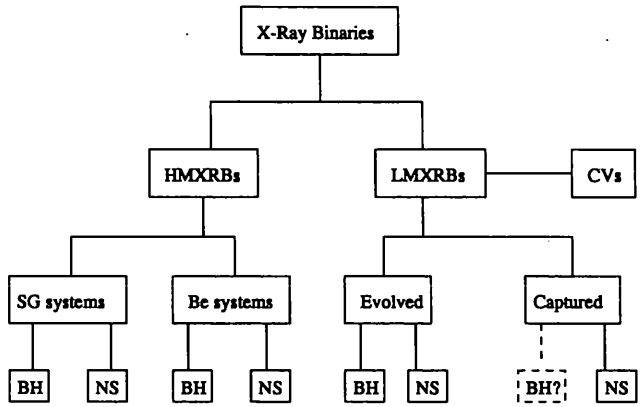

Figure 1.3 The various classes and sub-classes of X-ray binaries. NS indicates the compact object is a neutron star, while BH denotes a black hole. Note that no LMXRB globular cluster sources containing a black hole have been observed to date, hence the dashed border around the captured black hole catagory.

periods of between 1.4 and 10 days. The supergiants are tidally-deformed by the close proximity of the neutron star, as shown by double-wave ellipsoidal light variations. OB supergiants have strong winds, and accretion onto the neutron star is via this wind and/or caused by Roche lobe overflow.

The other sub-group are the Be HMXRBs, where the companions are main-sequence B-emission (Be) stars, with masses of around 8-20$M_{\odot}$. Be stars have a number of emission lines in their optical spectra, hence the designation, and are thought to be rotating close to break-up velocity. These systems have much longer orbital periods of between 15 and 180 days, there is no evidence of tidal distortion, and the orbits tend to be somewhat eccentric. Accretion onto the neutron star occurs either continuously or at periastron via the ejection of material from the equatorial regions of the Be star in outbursts. These outbursts are also observed optically.

1.3.2 HMXRB evolution

Neutron stars are formed by the collapse of the degenerate core of an evolved massive ($\geq$ 8$M_{\odot}$) star, undergoing a Type II supernova explosion. During a Type II supernova explosion, the outer layers, and most of the mass, of the exploding star are blown off into space. This causes difficulties for XRB evolution, since the more massive star will evolve more quickly and hence go supernova sooner, and dynamical studies have shown that if over half the total system mass is lost in a binary system, the system itself is very likely to be disrupted. To result in a bound system containing a neutron star after the supernova, evolutionary senarios include a period of mass transfer before the formation of the neutron star. This has

the effect of transfering some of the material in the outer layers of the more massive star onto its companion, so that when what was originally the more massive star goes supernova, less than half the total system mass is lost and the binary is likely to remain bound.

There are two main evolution scenarios for HMXRBs, the conservative scenario which assumes the mass and angular momentum are conserved, and the non-conservative scenario in which significant amounts of mass and angular momentum are lost from the system.

The conservative scenario (Figure 1.4) is most applicable to binary systems whose components are of roughly equal mass and have a relatively wide orbit. The more massive star will evolve more quickly, expand to fill its Roche lobe, and begin to transfer mass onto its companion. As mass is being transfered from the more massive to the less massive star, the orbital separation will shrink at first. However, as the mass ratio is close to unity, the transfer of mass will soon reverse the mass ratio, with the Roche-lobe-filling star now being the less massive of the two. This situation will cause the orbit to expand. Eventually, only the He core of the Roche-lobe-filling star will be left, while the other star will now be somewhat more massive, and rotating rapidly due to the transfer of angular momentum. Eventually, the He core will go supernova, and as less than half the total system mass will be lost, the binary is likely to remain bound, although the orbit may now be very eccentric. The newly-formed neutron star may now start to accrete material from the stellar wind of its companion, and produce X-ray emission. This scenario is a likely explanation for the formation of Be HMXRBs, as it appears to account for many of the characteristics of these systems: wide, eccentric orbits; and a rapidly rotating optical companion.

The non-conservative scenario (Figure 1.5) assumes that significant amounts of mass and angular momentum are lost from the system during its evolution. It is more applicable to fairly close orbits with a large mass ratio. As before, the more massive star evolves more quickly, but is losing mass via its stellar wind, widening the orbit. Eventually, the larger star will expand to fill its Roche lobe, and begin to transfer mass onto its companion, which will have the effect of shrinking the orbit once more. As the two stars spiral towards each other, the envelope of the larger star will be thrown off into space, leaving a He core, which is less massive than its companion. When the core goes supernova, less than half the total system mass will be lost and so the system will remain bound. The neutron star may produce X-ray emission by accreting material via the stellar wind of its companion, or via Roche-lobe overflow, which will cause the orbit to shrink further. As the orbit shrinks, tidal effects become much more significant, and will tend to circularise the orbit. This scenario is a likely explanation for the formation of supergiant HMXRBS, and accounts for the characteristics of these systems: small, circular orbits, and an optical companion which does not appear to

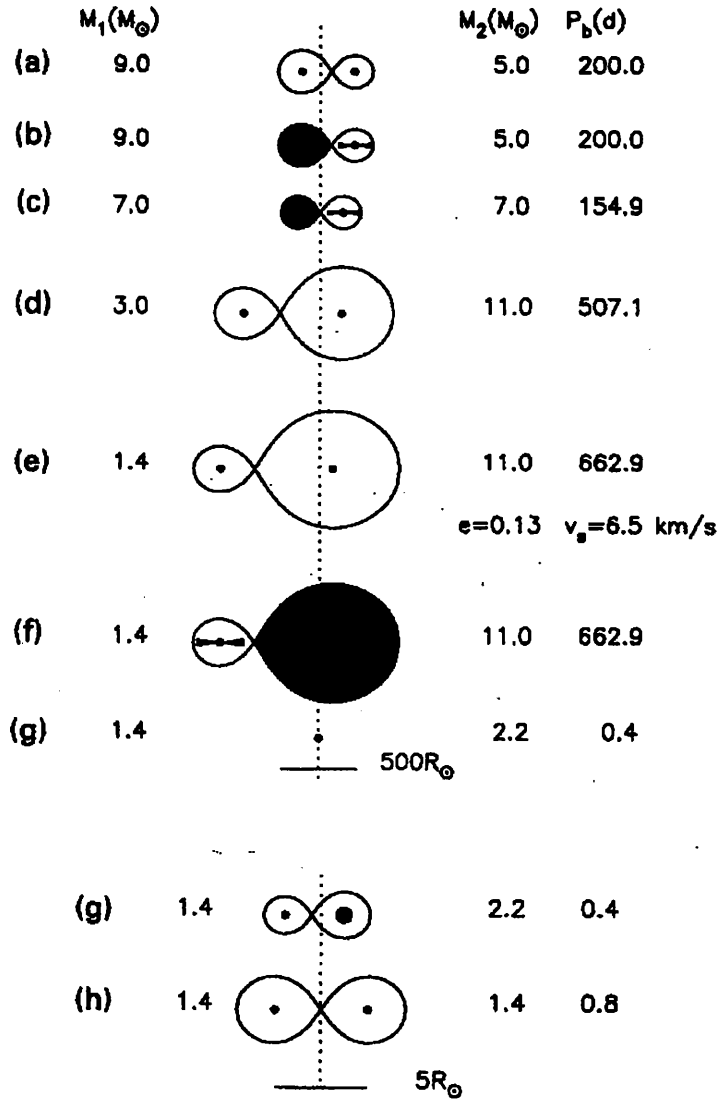

Figure 1.4 The evolution of a wide high-mass binary into a high-mass X-ray binary, according to the conservative scenario (Verbunt & van den Heuvel, 1995).

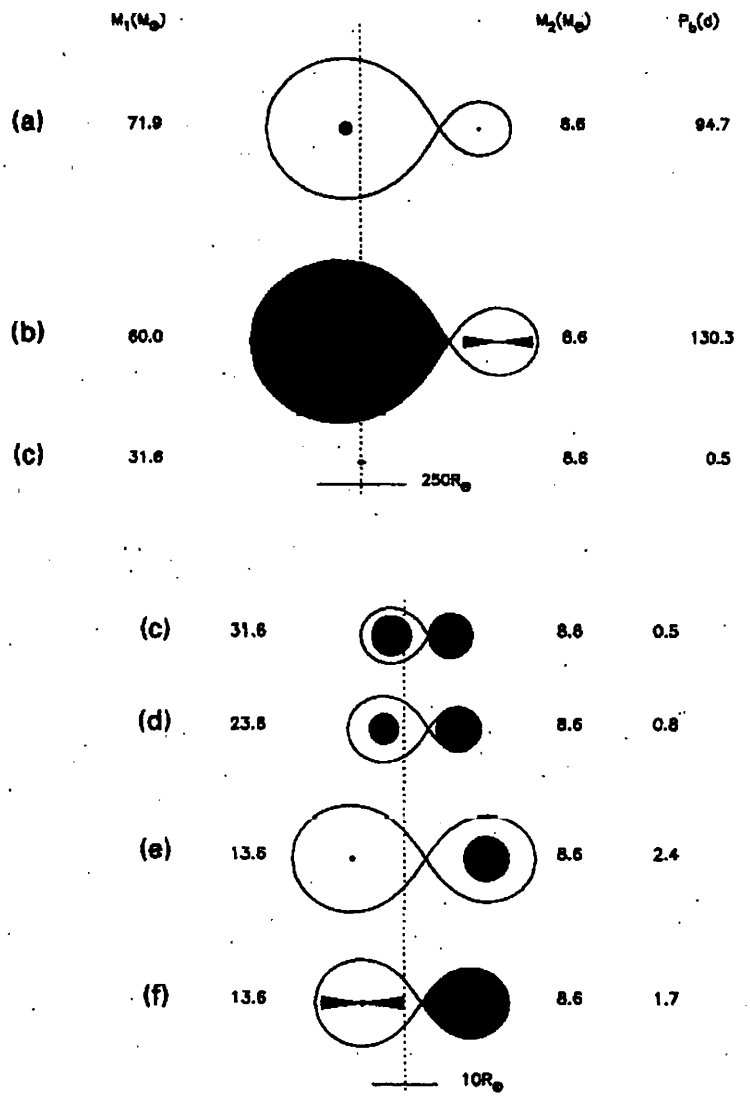

Figure 1.5 The evolution of a high-mass binary into a high-mass X-ray binary, according to the non-conservative scenario (Verbunt & van den Heuvel, 1995).

be rotating rapidly.

1.3.3 LMXRBs

LMXRBS consist of a neutron star or black hole accreting materal via Roche-lobe overflow from a donor of $\leq 1 M_{\odot}$. The companions are generally found to be population II main-sequence G or K type stars, although in a few systems (eg 4U1820-30), the donor star is thought to be a white dwarf. The orbital periods of LMXRBs vary from 11 minutes to 17 days. Cataclysmic Variables (CVs) are a subset of LMXRBs in which the compact object is a white dwarf, rather than a neutron star or black hole candidate.

1.3.4 LMXRB evolution

The evolution of LMXRBs presents some additional problems to those encountered with HMXRBs. The compact object and its accretion disc can obscure any optical emission from the donor, making investigating it difficult. The problem of system disruption after the first supernova explosion is also exacerbated, as the donor is very much smaller than a star capable of producing a neutron star. There are three main evolution scenarios for LMXRB evolution: the spiral-in scenario, the "quiet" supernova senario, and globular cluster scenarios where the neutron star is formed first, then acquires a companion.

The spiral-in scenario assumes an initial binary with quite an extreme mass ratio - the more massive star must be at least $8 M_{\odot}$ to produce a neutron star, and its companion around $1 M_{\odot}$. As before, the more massive star evolves more rapidly, expands, and begins to transfer mass onto its companion via Roche-lobe overflow. This will cause the companion to spiral towards the more massive star, but due to the companion's small mass, it will only be able to provide enough angular momentum to throw off the more massive star's envelope if the initial orbit was very wide. Disruption of the binary system can also be overcome if, by chance, the neutron star receives a kick velocity in the right direction.

The "quiet" supernova scenario assumes an initial binary in which the larger star is not quite massive enough to go supernova, and produce a neutron star, but instead produces a white dwarf. Later, as the smaller star expands, it fills its Roche lobe and begins to transfer mass onto the white dwarf. If this additional mass is sufficient to bring the white dwarf over the Chandrasekhar limit, the maximum mass which can be supported by a degenerate electron gas, a Type I supernova will occur. A neutron star will thus be formed with little mass loss, and the binary system is unlikely to be disrupted.

Around 10% of LMXRBs are found in globular clusters, even though globular clusters

account for only around 0.1% of stars in the Galaxy. A similar situation is found for the nearby galaxy M31. This suggests that LMXRBs are much more likely to form in globular clusters, and this is probably due to the extremely high density of stars which allows a solitary neutron star to acquire a companion. Neutron stars, at around $1.4M_{\odot}$ are more massive than the average member of a globular cluster. This means they will gravitate towards the dense centre of the cluster, making a close encounter more likely. There are two means by which a neutron star can acquire a companion: tidal capture, and three body capture. In tidal capture, the neutron star and a main-sequence star have a close encounter which causes tidal waves on the surface of the main-sequence star. This dissipates enough orbital energy to bring the two stars into a binary orbit. Three body capture involves the neutron star encountering an existing binary system composed of two main-sequence stars. The most likely outcome of this is that the least massive star will be ejected, and the remaining main-sequence star and the neutron star form a binary system.

1.4 Neutron Star Masses

As shown previously, a neutron star is formed by the collapse of the degenerate core of an evolved massive star undergoing a supernova explosion. Such high densities are reached that inverse-beta decay occurs - protons and electrons are crushed together ($p + e^{-} \rightarrow n + \nu_e$) to form a degenerate neutron gas. It is the pressure from this gas which balances the inward gravitational force, and prevents the star collapsing further. Thus the attributes of these intriguing objects are determined by all four of the fundamental forces: the strong and weak nuclear forces, electromagnetism, and gravity.

Neutron stars have central densities ($\rho > 5 \times 10^{15}$g cm^{-3}) several times greater than those the nuclear matter saturation density ($\rho_{nm} \sim 2.7 \times 10^{14}$g cm^{-3}), and so potentially allow the properties of matter at these extreme densities to be examined. They also allow investigations of General Relativity in the "strong-field" regime, as a significant proportion of the neutron star's mass is due to gravitational self-energy. It has even been suggested that observations of neutron stars may allow insights as whether the gravitational constant, G, is variable with time, as neutron star masses will contain a record of past values of G (Thorsett 1997).

A number of neutron star properties can be potentially observed, either directly or indirectly. These include spin frequency, radii, cooling histories, rotational instabilites, and mass. Each of these properties is governed by the equation of state (EOS) of the neutron star matter, though this thesis is concerned only with mass.

Neutron stars were being modelled decades before the first neutron star was observed (Oppenheimer & Volkoff 1939). It is even claimed by some that Landau proposed the existence of neutron stars on the same day he heard of the discovery of the neutron. Most modern EOSs require that the mass of a neutron star must lie in the range $\sim$0.1–3$M_\odot$ (Salgado et al 1994, Thorsett et al 1993). These EOSs are derived from numerical solutions of the quantum mechanical nuclear many-body problem coupled with experimental nucleon-nucleon scattering data (see, for example Kalogera & Baym 1996). The EOSs are assumed to be accurate up to $\sim 2\rho_{nm}$, but extrapolation to the much higher densities required is difficult due to the lack of knowledge of baryon-baryon strong interactions, particularly hyperon*-nucleon and hyperon-hyperon interactions.

A different approach to modelling neutron star masses was followed by Rhoades & Ruffini (1974). An unknown EOS is assumed that allows a neutron star mass limited only by the requirements that the neutron star is in hydrostatic equilibrium, and that the speed of sound within the star does not exceed c (which would violate the principle of causality). This results in an absolute maximum neutron star mass of $\sim 3M_\odot$. This approach has been refined and extended by subsequent authors to take into account the rotation of the neutron star (see, for example, Chitre & Hartle 1976, Friedman & Ipser 1987).

However, it is important to note that the range of physically possible neutron star masses may be very different to the range of neutron star masses it is possible to produce during a supernova.

As the neutron star in a HMXRB accretes mass, its total mass will obviously increase. However, this mass increase occurs at a relatively slow rate: Tsuruta (1978) quotes a typical accretion rate of $\dot{M} \sim 10^{16} \mathrm{gs}^{-1}$, which corresponds to around $3.2 \times 10^{-10} M_\odot \mathrm{year}^{-1}$. An absolute maximum accretion rate of around $3 \times 10^{-8} M_\odot \mathrm{year}^{-1}$ can be obtained by assuming that the gravitional potential energy of the infalling material is converted to X-ray with perfect efficiency, and that the neutron star is radiating at the Eddington Limit. Given the accretion onto the neutron star occurs over a timescale of thousands of years, this means the mass of the neutron star in a HMXRB does not increase significantly over the lifetime of the system.

1.5 Optical Radial Velocity Meaurements

We now turn to a discussion of how neutron star masses may be obtained.

*Hyperons are non-nucleon baryons which do not decay via the strong interaction

Consider two stars of masses M_x and M_o, orbiting their stationary centre of mass at distances a_x and a_o with a period P. The mass ratio of the system, q, is simply given by the ratio of the radial velocity semi-amplitudes for each component:

$$q = \frac{M_x}{M_o} = \frac{a_o}{a_x} = \frac{K_o}{K_x} \tag{1.1}$$

where K_o is the semi-amplitude of the radial velocity of the optical component, and K_x is the semi-amplitude of the radial velocity of the neutron star.

This system can also be described by Newton's form of Kepler's third law:

$$P^2 = \frac{4\pi^2(a_o + a_x)^3}{G(M_o + M_x)} \tag{1.2}$$

This can be rearranged to give:

$$\frac{GP^2(M_o + M_x)}{4\pi^2} = a_o^3\left(1 + \frac{a_x}{a_o}\right)^3 \tag{1.3}$$

Since from Equation 1.1,

$$\frac{a_x}{a_o} = \frac{M_o}{M_x}, \tag{1.4}$$

we obtain,

$$\frac{GP^2(M_o + M_x)}{4\pi^2} = a_o^3\left(1 + \frac{M_o}{M_x}\right)^3 \tag{1.5}$$

which can be rewritten,

$$\frac{GP^2(M_o + M_x)}{4\pi^2} = a_o^3\left(\frac{(M_o + M_x)^3}{M_x}\right) \tag{1.6}$$

Now if i is the inclination of the orbital axis to the line of sight, and a_o' is the *projected* distance from the centre of mass of the optical component to the centre of mass of the system,

$$a_o = \frac{a_o'}{\sin i} \tag{1.7}$$

This means,

$$\frac{GP^2(M_o + M_x)}{4\pi^2} = \frac{(a_o')^3(M_o + M_x)^3}{M_x^3 \sin^3 i} \tag{1.8}$$

We therefore obtain the mass function equations,

$$\frac{M_x^3 \sin^3 i}{(M_o + M_x)^2} = \frac{(a_o')^3 4\pi^2}{GP^2} \tag{1.9}$$

$$\frac{M_o^3 \sin^3 i}{(M_x + M_o)^2} = \frac{(a_x')^3 4\pi^2}{GP^2} \tag{1.10}$$

The circumference of an elliptical orbit with semi-major axis, a, and eccentricity, e, is given by,

$$\frac{2\pi a}{(1-e^2)^{\frac{1}{2}}} \tag{1.11}$$

and so the average orbital speed, $\overline{v}$, of the orbiting object will be given by,

$$\overline{v} = \frac{2\pi a}{P(1-e^2)^{\frac{1}{2}}} \tag{1.12}$$

and since,

$$\frac{a}{a'} = \frac{\overline{v}}{K} \tag{1.13}$$

where a' is the *projected* semi-major axis, and K the *projected* radial velocity semi-amplitude, we obtain

$$K = \frac{2\pi a'}{P(1-e^2)^{\frac{1}{2}}} \tag{1.14}$$

and, rearranging,

$$a' = \frac{KP(1-e^2)^{\frac{1}{2}}}{2\pi} \tag{1.15}$$

if this is substituted into the mass function equation 1.9 we obtain,

$$\frac{M_x^3 \sin^3 i}{(M_o + M_x)^2} = \frac{K_o^3 P(1-e^2)^{\frac{3}{2}}}{2\pi G} \tag{1.16}$$

which can be rearranged to give,

$$M_x^3 = \frac{K_o^3 P(1-e^2)^{\frac{3}{2}}(M_o + M_x)^2}{2\pi G \sin^3 i} \tag{1.17}$$

and thus,

$$M_x = \frac{K_o^3 P(1-e^2)^{\frac{3}{2}}}{2\pi G \sin^3 i}\left(1 + \frac{M_o}{M_x}\right)^2 \tag{1.18}$$

and similarly,

$$M_o = \frac{K_x^3 P(1-e^2)^{\frac{3}{2}}}{2\pi G \sin^3 i}\left(1 + \frac{M_x}{M_o}\right)^2 \tag{1.19}$$

and substituting from Equation 1.1, we obtain,

$$M_o = \frac{K_x^3 P(1-e^2)^{\frac{3}{2}}}{2\pi G \sin^3 i}(1+q)^2 \tag{1.20}$$

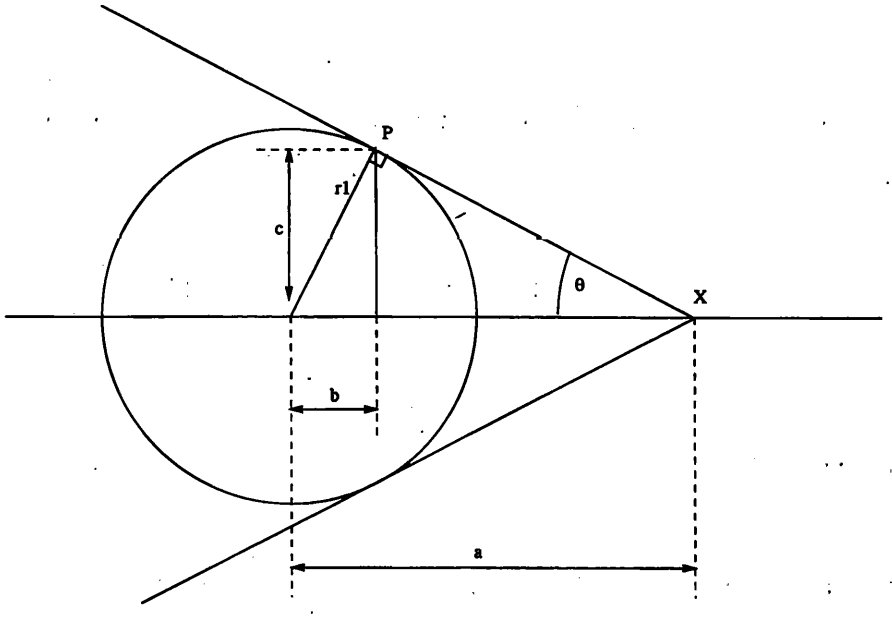

Figure 1.6 Overhead view of eclipse geometry.

and,

$$M_x = \frac{K_o^3 P(1-e^2)^{\frac{3}{2}}}{2\pi G \sin^3 i}\left(1+\frac{1}{q}\right)^2 \tag{1.21}$$

We therefore have a means of calculating the mass of the neutron star if the orbits of the two components and the inclination of the system are known. This is possible in an eclipsing X-ray binary system, in which the neutron star is a pulsar. X-ray pulse timing delays around the neutron star orbit yield the value of K_x, and conventional radial velocity measurements from optical spectra yield K_o.

A value for i can be obtained from the eclipse half-angle, θ_e, which is obtained by timing the X-ray eclipse:

$$\theta_e = \frac{E}{P}\pi \tag{1.22}$$

where E is the X-ray eclipse time, and P is the orbital period. Figure 1.6 shows the geometry of the eclipsing system. It can be seen that,

$$a^2 = r_1^2 + PX^2 \tag{1.23}$$

$$\Rightarrow PX^2 = a^2 - r_1^2 \tag{1.24}$$

and also that,

$$\sin\theta_e = \frac{r_1}{a} = \frac{b}{r_1} \tag{1.25}$$

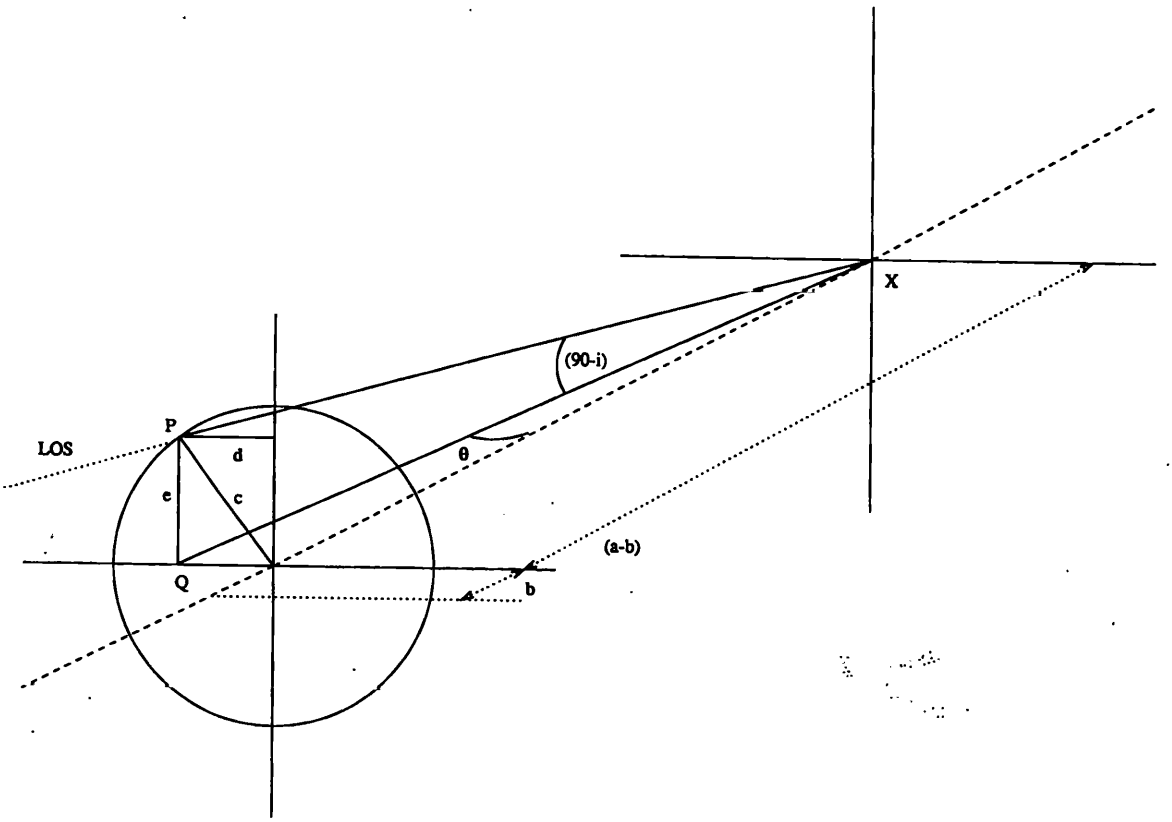

Figure 1.7 Isometric view of eclipse geometry (LOS is line of sight at mid-eclipse).

$$\Rightarrow b = \frac{r_1^2}{a} \tag{1.26}$$

Figure 1.7 shows the "X ray silhouette" of the eclipsing star the projection of the star onto a plane normal to the line of sight. For the point P,

$$r_1^2 = b^2 + d^2 + e^2 \tag{1.27}$$

Also from Figure 1.7,

$$\sin(90^o - i) = \cos i = \frac{e}{PX} \tag{1.28}$$

From equation 1.24,

$$e^2 = \cos^2 i(a^2 - r_1^2) \tag{1.29}$$

Also,

$$d = \sin\theta_e QX \tag{1.30}$$

Again from Figure 1.7,

$$QX = PX\cos(90^o - i) \tag{1.31}$$

from Equation 1.24

$$QX^2 = (a^2 - r_1^2)\sin^2 i \tag{1.32}$$

Combining with equation 1.30

$$d^2 = \sin^2\theta_e(a^2 - r_1^2)\sin^2 i \tag{1.33}$$

Now, from equations 1.26, 1.27, 1.29, and 1.30,

$$r_1^2 = \frac{r_1^4}{a^2} + (a^2 - r_1^2)\sin^2 i \sin^2\theta_e + \cos^2 i(a^2 - r_1^2) \tag{1.34}$$

Now,

$$\frac{r_1^2}{a^2} - \frac{r_1^4}{a^4} = \frac{r_1^2}{a^2}\left(1 - \frac{r_1^2}{a^2}\right) = \left(1 - \frac{r_1^2}{a^2}\right)\sin^2 i \sin^2\theta_e + \left(1 - \frac{r_1^2}{a^2}\right)\cos^2 i \tag{1.35}$$

$$\Rightarrow \frac{r_1}{a} = (\sin^2 i \sin^2\theta_e + \cos^2 i)^{\frac{1}{2}} \tag{1.36}$$

$$\Rightarrow \sin^2 i \sin^2\theta_e = \frac{r_1^2}{a^2} - \cos^2 i \tag{1.37}$$

$$\Rightarrow \sin^2 i(1 - \cos^2\theta_e) = \frac{r_1^2}{a^2} - (1 - \sin^2 i) \tag{1.38}$$

$$\Rightarrow \sin i = \frac{(1 - \frac{r_1^2}{a^2})^{\frac{1}{2}}}{\cos\theta_e} \tag{1.39}$$

This can be rewritten as

$$\sin i \approx \frac{[1 - \beta^2(\frac{R_L}{a})^2]^{\frac{1}{2}}}{\cos\theta_e} \tag{1.40}$$

where R_L is the radius of the eclipsing star's Roche lobe, and β is the fraction of the Roche lobe that the star occupies. The approximation sign is used since previously it was assumed that the eclipsing star was a perfect sphere, and the shape of Roche lobes deviate from this. Rappaport and Joss (1983) have determined numerically that,

$$\frac{R_L}{a} \approx A + B\log q + C\log^2 q \tag{1.41}$$

A, B, and C have been calculated by Rappaport & Joss (1983) to be:

$$A \approx 0.398 - 0.026\Omega^2 + 0.004\Omega^3 \tag{1.42}$$

$$B \approx -0.264 + 0.052\Omega^2 - 0.015\Omega^3 \tag{1.43}$$

$$C \approx -0.023 - 0.005\Omega^2 \tag{1.44}$$

where Ω is the ratio of the rotational frequency of the optical component to the orbital period.

It has been shown that direct mass measurements can be made of the neutron star in a pulsing, eclipsing X-ray binary by determining the radial velocity semi-amplitudes of both components, and the duration of the X-ray eclipse. This thesis will concentrate on arguably the most challenging of these three parameters, the radial velocity semi-amplitude of the X ray pulsar's companion, K_o. X-ray observations can result in very precise values for the radial velocity semi-amplitude of the X-ray pulsar, and the X-ray eclipse duration. However, there are a number of difficulties in making accurate measurements of K_o, and the uncertainties in K_o are the major source of uncertainties in the neutron star mass (see, for example, Clark et al 1988).

One problem is due to the large mass of the optical component relative to that of the neutron star. As we have seen, in supergiant HMXRB systems the optical componet will have a mass of at least $20M_\odot$, while the neutron star will have a mass of around $1.4M_\odot$. As Equation 1.1 shows, the ratio of the orbital radial velocities of the two stars is the inverse of the ratio of their masses. As a consequence, the optical component is going to have a relatively small radial velocity variation, making accurate measurements of it more difficult.

An accretion disc surrounding the neutron star can cause further difficulties. The accretion disc may have an intrinsic optical emission, which can contaminate the companion's spectra. Also the hemi-sphere of the optical companion closest to the neutron star may suffer from X-ray heating from the pulsar's emissions. Reynolds et al (1997) gives an example of how these two problems affected radial velocity measurements of Her X-1.

Another problem is due to tidal distortion of the optical companion. In most supergiant HMXRBs, the supergiant is filling, or nearly filling, its Roche lobe, a surface which deviates significantly from a perfect sphere. When the emitted light from a spherical object is collected and analysed, the average radial velocity measured will be that of the centre of mass of the sphere. If the shape of the star deviates from that of a sphere, however, this is no longer the case, and corrections based on assumptions of the system's Roche geometry have

to be applied to the measured radial velocity.

Stellar wind can also affect radial velocity measurements; and all OB-supergiants will have a strong stellar wind. When a significant amount of stellar material is streaming from the surface of a star at high velocity, the shape of most spectral lines will contain some degree of distortion. Material which is moving in a direction close to the observer's line of sight will cause spurious absorption at relatively high Doppler shift, while material more-or-less perpendicular to the observer's line of sight will cause spurious emission.Tidal distortion causes variation in the surface gravity of the supergiant, which affects the density and velocity of the wind, which in turn affects the extent of the resulting line distortion. If the line shape varies with orbital phase, any Doppler-shifting of the photospheric lines due to orbital motion may be obscured..

Another potential complication is due to the mass of the accretion disk. The inner parts of the accretion disk may contain a significant amount of mass relative to the mass of the neutron star. This mass will exert its own gravitional force on the supergiant component, and might, in effect, be included in the apparent mass of the neutron star. This would have the result of making the neutron star appear slightly more massive than in reality.

1.6 The Reduction Process

Stellar spectra are obtained using a three component system: a telescope which collects and focuses the stellar radiation; a spectrograph which disperses this radiation to form a spectrum; and a detector which records this spectrum. As long as the telescope is well-sited and large enough to collect a useful amount of starlight from the desired target, its design has little influence on the stellar spectra. There are two main types of spectrograph, the standard, and the echelle. In a standard spectrograph the light passes through a narrow slit and is dispersed perpendicular to this slit, using a grating or a prism, producing an image with a spatial axis and a wavelength axis. An echelle spectrograph is much more complex, and will be described in detail in Chapter 3. Modern CCD (Charged Couple Device) detectors have almost completely taken over from photographic plates as the detector of choice. A CCD consists of a piece of silicon crystal on which has been placed a grid of tiny electrodes, coated with a photosensitive material. When a current is applied to the electrodes, voltage wells are created. A photon incident on the photosensitive material will liberate one or more electrons which will be collected in one of the voltage wells. The CCD is read out by applying a pulsing voltage to the electrodes, which has the effect of passing the contained charge down the line of voltage wells, allowing the charges to be measured

one by one. CCDs have the advantage of a high quantum efficiency, and a highly linear response. The digital nature of their output makes them particularly convenient.

The process of reducing spectral CCD data has four main steps: bias subtraction, flat-fielding, extraction, and wavelength calibration (see, for example, Massey 1992). When a CCD is read out, a bias voltage is added, which has to be removed from each frame, along with any readout noise. At the telescope, several bias frames are taken at the beginning and end of each observing session. These are produced by setting the exposure, or integration, time to zero, and reading out the CCD. These bias frames are then averaged, and subtracted from all the frames used in the reduction process. As the bias frame may vary throughout the session, it is also possible to add an overscan region to each frame by reading out some extra columns after all the data has been read. This overscan region allows a check on the variation of the bias level.

Once the bias level has been removed, the frames must be corrected for the varying response of the individual pixels. At the telescope, so-called flat-fields are obtained by exposing the spectrometer to a spectrally-flat light source such as a high pressure mercury lamp or the twilight sky. These flat-fields are averaged and normalised. The resultant flat-field is then averaged in the wavelength direction, to produce a flat-field which varies only in the spatial direction. Each frame is then divided by this flat-field to correct for the varying response of the pixels in the spatial direction. Modern CCDs have much less pixel-to-pixel variation than older CCDs, so careful flat-fielding is now less important when reducing spectroscopic CCD frames.

There are two effects which must be corrected for at this stage. A cosmic ray strike on the CCD during an observation will cause a large number of spurious counts in a very localised area. These "spikes" can usually be detected automatically by the reduction software, and the values of the affected pixels are replaced by an average of the surrounding pixels. A similar problem is that of bad pixels and columns. Nearly all CCD chips contain a number of defects which manifest themselves as pixels which do not respond to incident radiation. Sometimes a pixel will block the transfer of charge across it, rendering a whole column useless. These bad pixels and columns are fixed in a similar way to cosmic ray strikes.

The spectra of interest can now be extracted from the processed frames. A function is fitted to the path of the desired spectrum across the frame, and an algorithm such as optimal extraction (Horne 1986) is used to produce a stellar spectrum. The conventional extraction procedure is to sum the range of pixels enclosing the object spectrum in the spatial dimension. The problem with this is that pixels containing only a small fraction of the light, and hence a poor signal-to-noise ratio are included, wasting information. Optimal

extraction overcomes this by applying varying weights to the summed pixels in order to reduce statistical noise to a minimum. The algorithm can also be used to automatically remove cosmic rays strikes.This technique can offer up to a 70% gain in effective exposure time when compared to conventional procedures.

A sky spectrum is also extracted, then subtracted from the stellar spectrum to rid the stellar spectrum of lines due to the Earth's atmosphere.

The next step is to wavelength calibrate the spectrum. Between each observation at the telescope, frames are taken of an arc-lamp which has a number of easily identifiable lines. These arc-frames are processed identically to the stellar frames (except that optimal extraction is not generally used), and the emission lines they contain can be identified and assigned a wavelength. This allows a wavelength scale to be established which can simply be copied onto the stellar spectra. It is crucial that this step be performed very carefully when looking for small Doppler shifts in the stellar spectra.

Radial velocity changes between two spectra (the observed spectra and the template) are determined using a technique known as cross-correlation (see, for example, Tonry & Davis 1979). To begin with, both spectra have to be mapped to a logarithmic scale, $f(\lambda) \rightarrow f(n), n = A \ln \lambda + B$, where A and B are constants. A Doppler shift in $f(n)$ will now correspond to a uniform shift in $f(n)$. Let

$$c_{f,t}(s) \equiv K \int_a^b f(n)t(n-s)dn \tag{1.45}$$

where K is a normalisation factor, s is the amount by which the template is shifted, $f(n)$ is the spectrum, and $t(n-s)$ is the template. When $f(n)$ matches $t(n-s)$ exactly, $c_{f,t}(s) = 1$, and s is the relative Doppler shift between the spectrum and the template. However, since CCD spectra are not continuous, we replace the integrations with summations over N bins,

$$c_{f,t}(s) \equiv K \sum_{n=1}^{N} f(n)t(n-s) \tag{1.46}$$

As before, the shift, s, which maximises $c_{f,t}(s)$ corresponds to the Doppler shift of the spectrum relative to the template. The problem with the above method is that it requires $c_{f,t}(s)$ to be calculated for a wide range of values for s, and this is very computationally intensive. Instead if we now let

$$F(k) \equiv \sum_{n=1}^{N} f(n) \exp(\frac{-2\pi ink}{N}) \tag{1.47}$$

Now define the normalised cross-correlation function,

$$c(n) \equiv f(n) \times t(n) = \frac{1}{N\sigma_f\sigma_t} \sum_{m=1}^{N} g(m)t(m-n) \tag{1.48}$$

where $\times$ is the cross-correlation product (not commutative). It is defined so that if $g(n)$ is exactly the same as $t(n)$, $g \times t(n)$ will have a peak of 1 at $n = d$. If we take the Fourier transform of Equation 1.48 we obtain,

$$C(k) = \frac{1}{N\sigma_f\sigma_t} F(k)T^*(k) \tag{1.49}$$

where $T^*(k)$ is the complex conjugate of $T(k)$. The cross-correlation function, $c(n)$, can then be obtained by performing a reverse Fourier transform on $C(k)$. The peak of $c(n)$ is then fitted by a smooth symmetric function. The central position of the fit gives the amount by which the spectrum has been shifted relative to the template.

A problem often encountered when using this technique on actual stellar spectra is that of noise auto-correlation. Every spectrum contains a non-zero level of noise, and the noise present in the object and template spectra tends to produce a secondary peak at a position equivalent to a zero Doppler shift (see, for example, van Kerkwijk 1993). Figure 1.5 shows a cross-correlation peak taken from van Kerkwijk et al (1995). The top panel shows the "raw" cross-correlation peak, while the middle panel shows the residuals after a Gaussian has been fitted and subtracted. There is quite an obvious peak at zero velocity.

1.7 Current HMXRB Neutron Star Masses

There are seven HMXRB systems for which it is possible to determine the mass of the neutron star, although the uncertainties involved are usually quite large. The mass values below are summarised in Table 1.1.

1.7.1 LMC X-4

This system has a 1.4 day orbital period, and exhibits a 30.4 day period variation, thought to be due to a precessing accretion disc. Levine et al (1991) determined the mass of the neutron star to be $1.38 \pm 0.25 M_\odot$ using X-ray pulse-timing measurements and a Monte Carlo error analysis. van Kerkwijk et al (1995) re-examained the available data, and revised the mass estimate to $1.47^{+0.44}_{-0.39} M_\odot$.

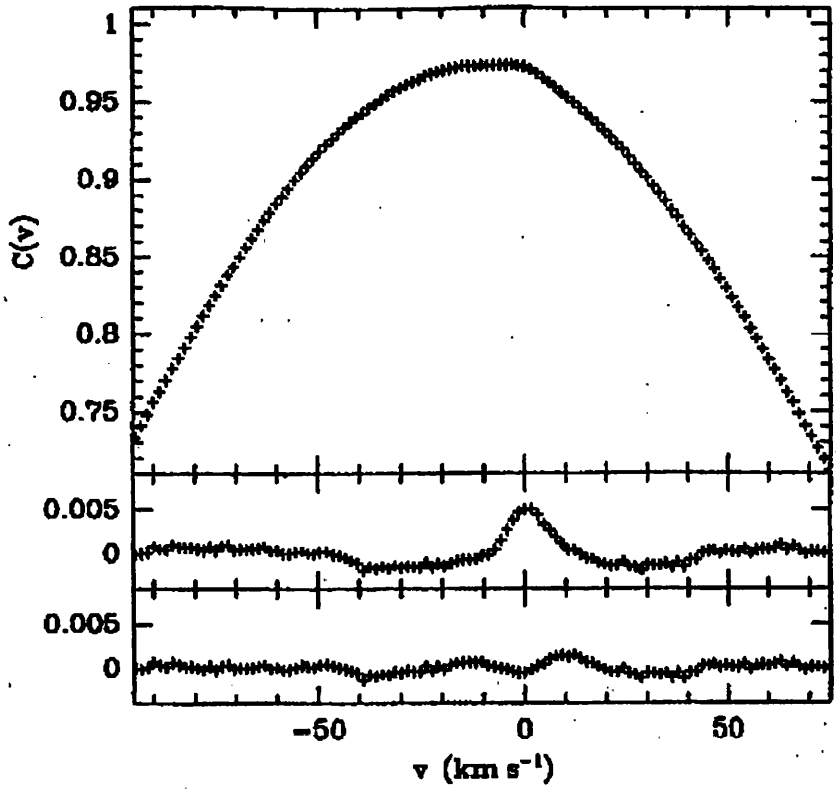

Figure 1.8 Cross correlation peak data taken from van Kerkwijk et al (1995). The top panel shows the "raw" cross correlation peak, while the middle panel shows the residuals after a Guassian has been fitted and subtracted. There is an obvious peak at zero velocity.

1.7.2 Cen X-3

Cen X-3 has an orbital period of 2.1 days, and accretion onto the neutron star is via incipient Roche-lobe overflow and stellar wind. Previous values for the mass of the neutron star are $1.0\pm0.3M_{\odot}$ (Hutchings et al 1979), and $1.23\pm0.60M_{\odot}$ (Clark et al 1988), both derived from X-ray pulse-timing measurements and optical radial velocity measurements. van Kerkwijk (1993) obtains a value of $1.09^{+0.58}_{-0.51}$. The mass determination for the neutron star in Cen X-3 is dealt with in detail in Chapter 2, and is found to be $1.21\pm0.21M_{\odot}$.

1.7.3 4U1538-52

This system has an orbital period of 3.7 days. Accretion is wind-fed, and there is no evidence of an accretion disc (Reynolds et al 1992). Makishima et al (1987) obtain a mass for the neutron star of $1.8\pm0.5M_{\odot}$ via X-ray pulse-timing measurements, while Reynolds et al (1992) obtain a value of $1.3\pm0.2M_{\odot}$ from optical observations of the neutron star's companion. van Kerkwijk et al's (1995) re-examination of the available data obtain a value of $1.06^{+0.41}_{-0.34}M_{\odot}$.

1.7.4 SMC X-1

This system has an orbital period of 3.9 days. Accretion is via Roche-lobe overflow, and there is evidence of a precessing accretion disc (Reynolds et al 1993). Levine et al (1993) obtain a value of $1.1\pm0.2M_{\odot}$ for the mass of the neutron star from X-ray pulse timing measurements and a Monte Carlo analysis, whereas Reynolds et al (1993) obtain a value of $1.6\pm0.1M_{\odot}$ from optical radial velocity measurements. van Kerkwijk et al (1995) obtain a value of $1.17^{+0.36}_{-0.32}M_{\odot}$.

1.7.5 Vela X-1

This system is the only eclipsing, pulsing HMXRB with a eccentric orbit ($e = 0.089 \pm 0.03$). The mass of its neutron star is not well established: van Kerkwijk et al (1993) obtains a value of $1.9^{+0.7}_{-0.5}M_{\odot}$ from optical radial velocity measurements, while Stickland et al (1997) give a value of $1.34\text{-}1.53M_{\odot}$, based on space-based UV observations. A value of $1.77^{+0.55}_{-0.29}M_{\odot}$ is obtained in Chapter 3.

1.7.6 Her X-1

Her X-1 is distinct from the above systems, as the donor star is of relatively low mass ($\sim 2M_{\odot}$), and can be regarded as a sort of intermediate between the HMXRBs and the LMXRBs. The orbital period is 1.7 days, accretion onto the neutron star is via Roche-lobe overflow, and the donor is subject to considerable tidal distortion and X-ray heating. van Kerkwijk et al (1995) quote two mass estimates for the neutron star, based on different methods. The first method, involving optical spectroscopy of the donor, yields a mass of $1.01^{+0.75}_{-0.58}M_{\odot}$. The second method is based on analysis of the optical pulses which are due to reprocessing of the X-ray pulses from the neutron star by the surface of its companion. This method yields a mass value of $1.47^{+0.23}_{-0.37}M_{\odot}$, and van Kerkwijk et al (1995) state that this appears to be more accurate than the first method. Reynolds et al (1997) present new optical spectroscopy of the companion, and find a neutron star mass of $1.5\pm0.3M_{\odot}$, which agrees very well with the previous optical pulsations method.

1.7.7 4U1700-37

This system differs from all the above, as although it is an X-ray eclipsing system believed to contain a neutron star, it does not exhibit X-ray pulses or bursts. This means radial velocity data for the neutron star cannot be obtained by pulse timing measurements, and so various assumptions about the mass and radius of the donor star must be made based on

System	Mass estimates
LMC X-4	1.38 ± 0.25[1],$1.47^{+0.44}_{-0.39}$[2]
Cen X-3	1.0 ± 0.3[3],1.23 ± 0.60[4],1.21 ± 0.21[5],$1.09^{+0.58}_{-0.51}$[2]
4U1538-52	1.8 ± 0.5[6],1.3 ± 0.2[7],$1.06^{+0.41}_{-0.34}$[2]
SMC X-1	1.1 ± 0.2[8],1.6 ± 0.1[9],$1.17^{+0.36}_{-0.32}$[2]
Vela X-1	$1.9^{+0.7}_{-0.5}$[10],$1.34 - 1.53$[11], $1.77^{+0.55}_{-0.29}$[12]
Her X-1	$1.04^{+0.75}_{-0.58}$ or $1.47^{+0.23}_{-0.37}$[2], 1.5 ± 0.3[13]
4U1700-37	1.8 ± 0.4[14], $2.6^{+2.3}_{-1.4}$[15]

Table 1.1 Summary of HMXRB neutron star masses. References: [1] Levine et al (1991), [2] van Kerkwijk (1993), [3] Hutchings et al (1979), [4] Clark et al (1988), [5] Ash et al (1999) and Chapter 2, [6] Makishima et al (1987), [7] Reynolds et al (1992), [8] Levine et al (1993), [9] Reynolds et al (1993), [10] van Kerkwijk et al (1995), [11] Stickland et al (1997), [12] Chapter 3, [13] Reynolds et al (1997), [14] Heap & Corcoran (1992), [15] Rubin et al (1996)

stellar models. Heap & Corcoran (1992) obtain a value of $1.8 \pm 0.4 M_\odot$ for M_x, the mass of the neutron star, by assuming that $i \geq 80°$. By contrast, Stickland & Lloyd (1993) assume that $M_x = 1.4 M_\odot$, which leads them to a pair of solutions for the companion star mass and inclination, namely $M_o \sim 15\ M_\odot$ and $i \sim 19°$, or $M_o \sim 72\ M_\odot$ and $i \sim 62°$.

However, Rubin et.al (1996), challenge these assumptions, claiming that an inclination as low as 60° would still be compatible with the observed X-ray eclipses. Instead they quote a value of $M_x = 2.6^{+2.3}_{-1.4} M_\odot$, and $i = 66^{\circ +7}_{-5}$.

1.8 Neutron star masses from radio pulsars

Another type of system which can yield neutron star masses are binary systems containing radio pulsars. There are approximately fifty such systems known, including five double neutron star binaries, and radio pulsars with white dwarf or main sequence companions (Thorsett & Chakrabarty 1999).

The most accurate neutron star mass values are obtained from timing measurements of relativistic corrections to the Keplerian orbital equations. In several cases, the associated uncertainties exceed those of the constant G, and masses are quoted in solar units of $GM_\odot$ to retain the full accuracy. However, this is only possible for close eccentric binary orbits, or when the orbital inclination, i, is close to 90°. In the majority of cases, timing observations

only provide the information described in Section 1.5, and to obtain a value for the neutron star mass, observations of the companion must be performed. For main-sequence companions this involves radial velocity measurement as described in Section 1.6, but in the case of white dwarfs, several other techniques can be used. Given a theoretical relationship between the mass and radius of the white dwarf, the mass can be obtained by determining the radius. This can be done, for example, by fitting a model atmosphere to the observed spectrum to find $\log g$ (Bergeron et al 1991).

All of the mass values determined from double radio pulsar systems are consistent with a very narrow distribution: $1.35 \pm 0.04 M_{\odot}$.

1.9 Neutron star masses from kilo-Hertz QPOs

Zhang et al (1997) describe kHz quasi-periodic oscillations (QPOs) discovered during X-ray observations of LMXRBs by the Rossi X-ray Timing Explorer. They propose that the highest observed QPO frequency can be taken as the orbital frequency of the marginally stable orbit - the closest stable orbit to the surface of the neutron star. Knowing this quantity leads to a value for the mass of the neutron star. Neutron star masses have been obtained for eight LMXRB systems in this way, and the values are all in the vicinity of $2.0 M_{\odot}$. It is suggested that these neutron stars were formed with masses of $1.4 M_{\odot}$, and have subsequently accreted the additional material.

1.10 Measuring the radius of an isolated neutron star

Another method for ruling out some of the various neutron star EOSs, was suggested by Walter & Matthews (1997), who discovered the first optical counterpart to an isolated neutron star using the Hubble Space Telescope. Spectral evidence, and the fact that there appeared to be little variability, suggested that the radiation was due to thermal emission from the neutron star's surface. If this was the case, the radius of the neutron star could be determined if its distance was known. A molecular cloud of known distance lay in the same line-of-sight as the neutron star, and as it was reasonable to assume the neutron star was a foreground object, the distance to the cloud could be taken as an upper limit to the distance to the neutron star. It was found that the radius of the neutron star cannot exceed 14km, which is inconsistent with a number of proposed EOSs.

Chapter 2

The mass of the neutron star in Centaurus X-3

"The great tragedy of science - the slaying of a beautiful hypothesis by an ugly fact"

Aldous Huxley

2.1 Summary

This chapter will deal with the attempts to determine the mass of the neutron star in Cen X-3, starting with the historical background. The various observations and the data reduction process will then be described, followed by a discussion of the analysis, results, and conclusion.

2.2 Historical Background

Centaurus X-3 was first detected by a pair of rocket-bourne proportional counters (Chodil 1967). The launch of the Uhuru satellite allowed the discovery of regular pulsations from the system, with a ~5 s period (Giacconi et al 1971). Additionally an intensity increase of factor 10, and variations in the pulse period were observed. Further Uhuru observations revealed that the intensity changes were regular and that the pulse period variations were sinusoidal. This suggested that these phenomena were due to Cen X-3 having a massive binary companion. It was proposed that the intensity changes were due to the occultation of the X-ray source by the companion, while the pulsation period variations were due to the orbital motion of the X-ray source Dopper-shifting the pulse signals.

Despite detailed Uhuru data, the search for an optical counterpart was hampered by the location of Cen X-3 in the Galactic plane, in the direction of the Carina spiral arm.

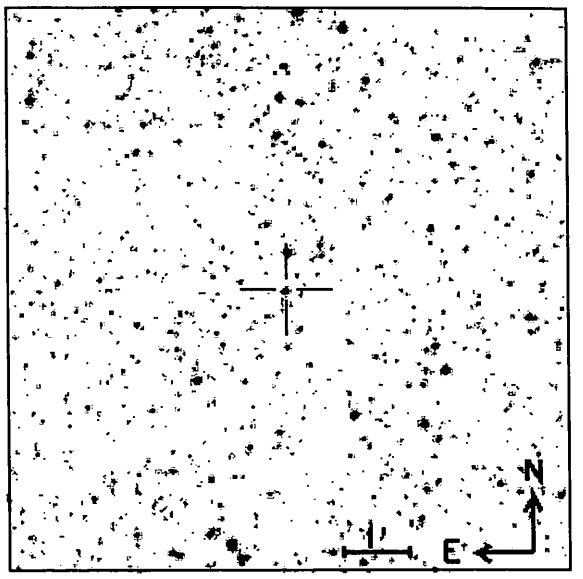

Figure 2.1 Optical finding chart for Cen X-3.

This meant observers were forced to search among the large number of faint stars contained within the X-ray position error box. Eventually, a 13th magnitude star with a double-peaked light curve was found during a photometric survey (Kreminski 1973a,1973b). The period and phase of the light curve matched that of the X-ray emission, demonstrating it was the optical counterpart to Cen X-3.

The system is now known to consist of the star V779 Cen, an O6.5 supergiant, in a 2.09 day circular orbit with an accreting neutron star companion, which emits X-ray pulses with a period of 4.84 s. The luminosity of the X-ray source ($\approx 5.0 \times 10^{37}$ erg s^{-1}) suggests that the predominant mode of accretion is via a disk, fed by incipient Roche-lobe overflow, although a strong stellar wind does emanate from the supergiant (Van Paradijs 1998, Nagase 1992).

2.3 Neutron star mass determination

In Chapter 1.5, it was shown that pulsing, eclipsing XRBs such as Cen X-3 allow direct measurements to be made of the mass of the neutron star. Equations 1.1 – 1.44 can be used to determine values for the neutron star mass, M_x, and the mass of its companion,

M_o, given values for K_x, the semi-amplitude of the radial velocity of the neutron star; K_o, the semi-amplitude of the radial velocity of its companion; θ_e, the eclipse half-angle; β, the ratio of the radius of the companion to the radius of its Roche lobe; and Ω, the ratio of the rotational frequency of the optical companion to the orbital period.

In the case of Cen X-3, K_x has been measured as 414.1 ± 0.9 km s^{-1} by X-ray pulse-timing observations (Nagase et al 1992), and θ_e has been determined to be $32°.9 \pm 0°.5$ by Clark et al (1988), who made a detailed model of the optical component's atmosphere in order to accurately determine the point at which the X-ray source entered eclipse. As the neutron star is accreting material by Roche-lobe overflow, the optical component must be filling its Roche lobe, so $\beta \approx 1$. We also argue that tidal dissipation will have forced the system into approximately synchronous rotation, so $\Omega \approx 1$ (Rappaport & Joss 1983, and references therein). This means the rotation period of the supergiant exactly matches the orbital period of the system, and so the supergiant always presents to same side to the neutron star. To an intrepid observer on the surface of the supergiant, the neutron star would appear to remain at a fixed position in the sky. On the scale of the supergiant, the neutron star is essentially a point mass, and so is not subject to tidal forces. Thus the rotation period of the neutron star is not synchronised with the orbital period, and continues to rotate on its axis every 4.84 seconds.

However, large uncertainties exist in values for K_o. The semi-amplitude of the optical radial velocity curve has previously been quoted as 24 ± 5 km s^{-1} (Hutchings et al 1979), 26 ± 3 km s^{-1} (Aslanov & Cherepashchuk 1982), and more recently as 61 ± 9 km s^{-1} (Reynolds 1991).

Values for the neutron star mass determined from these parameters have been quoted as > 3 M$_\odot$ (Mauder 1975), 2.5 ± 1.1 M$_\odot$ (Petro 1975), 1.0 ± 0.3 M$_\odot$ (Hutchings et al 1979), and 1.23 ± 0.60 M$_\odot$ (Clark et al 1988). It is hoped that new observations with modern CCD detectors and improved analysis techniques can reduce these uncertainties.

2.4 Observations

Thirty spectra of Cen X-3 were obtained during 1990 March 4–10 by Bell and Reynolds using the Anglo-Australian Telescope. The instrumental setup consisted of the RGO Spectrograph in combination with the 25 cm camera, the 1200B grating, and the GEC CCD detector (Tinney 1996). The wavelength range chosen was 4300–4700 Å, and the dispersion was 0.7 Å pixel^{-1}. Another 10 spectra were obtained on 1994 February 26 by Roche, Reynolds and Jupp with the same instrument and camera, but using the 1200V grating and the TEK

CCD detector. The wavelength range in this case was 4150–4770 Å, while the dispersion was 0.62 Å pixel^{-1}. The exposure times for both sets of observations were 1800s. A further 11 spectra were obtained on 1997 April 12–13 by Ash and Still, using the same instrument, camera, grating and detector as the 1994 observations. The wavelength range was 4150–4900 Å, with a dispersion of 0.75 Å pixel^{-1}. The exposure times for these observations were 900s.

2.5 Analysis

The three datasets were reduced consistently using the Starlink *FIGARO* software package (Shortridge & Meyerdierks 1996). The reduction process consisted of subtracting a mean bias frame from each flat, arc and object frame, dividing each object frame by a normalised mean flat frame, wavelength calibrating the object frames by identifying features on the arc frames, then re-binning the extracted object spectra into a linear wavelength range. Each of the three datasets was treated identically. Spectra of Cen X-3 from the various observations are shown in Figure 2.2.

Phases were assigned to the object spectra according to the quadratic ephemeris of Nagase et al (1992), determined from X-ray measurements:

$$\begin{aligned} T_N &= 2440958.85 + 2.08713845N \\ &\quad -(1.0362642 \times 10^{-8})N^2 \end{aligned} \tag{2.1}$$

Three radial velocity standard stars were observed in both 1990 and 1994, but unfortunately no radial velocity standards were observed in 1997. The 1990 and 1994 radial velocity standards yield a mean (Observed–Catalogue) velocity of 2.0 ± 6.0 km s^{-1}, demonstrating that the velocities are on the IAU standard system. If there is no systematic change in the radial velocity of Cen X-3 between 1990 and 1994, we can therefore combine these two datasets to produce a single radial velocity curve. Note, however, that since the spectra obtained in 1990 and 1994 do not overlap in phase coverage, we cannot be certain that no systematic change in velocity occurred, and so the radial velocity amplitude obtained from these data must be suspect. Furthermore, as there were no radial velocity standards observed on the 1997 run, only relative radial velocity values could be obtained for these spectra, and so they could not be combined with the 1990/1994 data, despite overlapping in phase with them. However, we *can* still use the 1997 data on their own to determine the semi-amplitude of the radial velocity, as the spectra obtained during this run spanned both

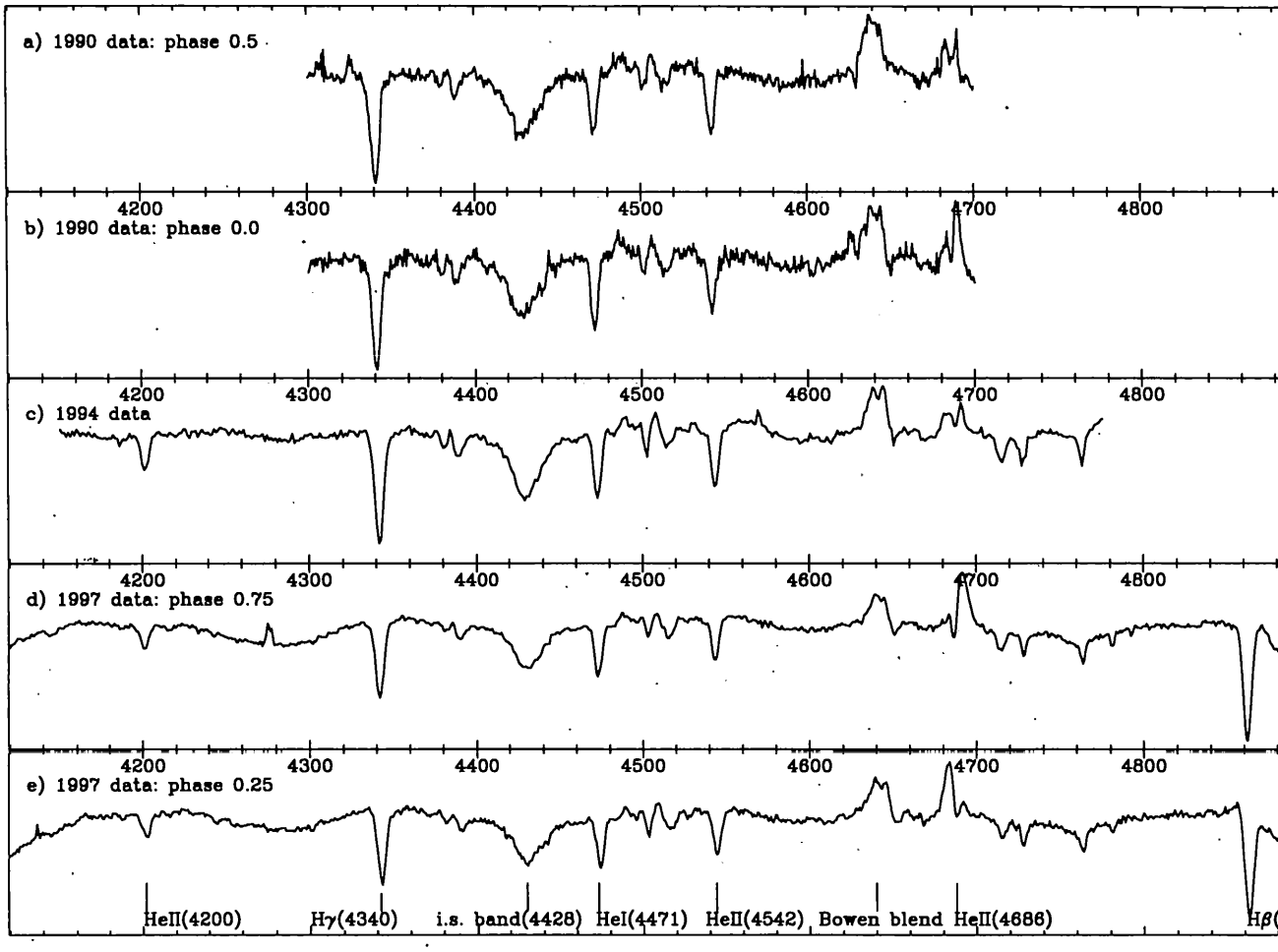

Figure 2.2 Mean rectified spectra of V779 Cen for a) the 1990 data ($\phi \sim 0.5$), b) the 1990 data ($\phi \sim 0.0$) c) the 1994 data, d) the 1997 data ($\phi \sim 0.75$), and e) the 1997 data ($\phi \sim 0.25$). Principle features are identified. Note the unidentified emission feature at ~ 4275Å in panel d) is only present in *one* of the individual spectra and we cannot be sure if it is a genuine line.

quadrature phases of the system, during a single binary orbit.

The radial velocity values were calculated as follows, using the cross-correlation facilities in *IRAF* (Barnes 1993). First, a mean spectrum was created for the combined 1990/1994 dataset by averaging all the spectra taken during these two runs; another mean spectrum was created for the 1997 dataset by averaging all the spectra during that run. For each individual spectrum, a region 10Å wide, centred on the spectral line to be examined, was cross-correlated against the corresponding region of the appropriate mean spectrum, to obtain the radial velocity values relative to the respective mean spectrum. (See Chapter 1 for a description of the process of cross-correlation.) A barycentric correction was applied automatically by the *IRAF* software.

The main advantage of this technique is that no radial velocity standard star was required, allowing the 1997 dataset to be analysed in an identical manner to the combined 1990/1994 dataset. Also, any systematic errors due to spectral type mis-matches between the observed star and the radial velocity standard are eliminated. Note however, that van Kerkwijk (1993) states that cross-correlating a number of spectra against their average, as we have done, produces a small peak in the cross-correlation function at zero velocity, so causing a slight systematic error towards zero velocity.

As cross-correlation techniques are essentially pattern-matching operations, and are usually used on a number of spectral lines, it may seem odd to cross-correlate over a single spectral feature. However, V779 Cen, as an early type supergiant, has relatively few spectral lines, and I was very concerned to minimise the effects of emission-line contamination from the strong stellar wind. By cross-correlating over single lines, it was hoped to isolate the effects of any contaminated features.

All the cross-correlation results are contained in the appendix to this chapter.

2.5.1 The 1990/1994 data

In order to investigate the significance of emission-line contamination and X-ray heating effects, separate radial velocity curves were obtained for the Hγ, HeI (4471Å), and HeII (4542Å) lines. The resulting sets of velocities were then fitted with a circular orbit solution. The period and phase zero were fixed at the values given by Nagase et al (1992) whilst K_0 and a bias velocity were allowed as free parameters. This bias velocity should not be confused with the systemic velocity. The systemic velocity is the velocity of the centre of mass of the system relative to the solar system barycentre, while the bias velocity is simply the difference between the velocity of the mean spectrum and the velocity at phases 0.0 and

0.5 of the fit.

Having found the best-fit solution (no points were rejected during the fits), the errors on the individual data points were rescaled (i.e. made larger) so as to give a reduced χ^2 of $\sim$1 for each radial velocity curve. This was done because the original error bars were a reflection of the uncertainty of the fit to the cross-correlation function (performed internally be *IRAF*). However, uncertainties calculated in this way do not reflect how well the points fit the theoretical curve. A useful measure of how well a theoretical curve fits a set of data points is the χ^2 statistic, defined as:

$$\chi^2 = \sum_{i=1}^{n} \frac{(D(i) - M(i))^2}{\sigma(i)^2} \tag{2.2}$$

where n is the number of data points, D are the observed data values for each point, M is the fitted data values, and σ are the errors in the observed data values. Additionally, the "reduced χ^2" statistic is defined as:

$$\chi^2_{reduced} = \frac{\chi^2}{\nu} \tag{2.3}$$

where ν is the number of degrees of freedom, the number of model parameters subtracted from the number of data points. As a general rule, a reduced χ^2 value of one indicates a good fit. A χ^2 value of much greater than one indicates a poor fit, and a χ^2 value much less than one indicates the errors in the data have been overestimated. (See Bevington et al 1992.)

In order to determine the uncertainty in the fitted parameters, a Monte Carlo analysis was carried out. This involved randomly assigning each radial velocity point to a position somewhere along its (rescaled) error bar, and then re-fitting the orbit solution to this randomised set of data. This procedure was repeated one thousand times for each curve. The uncertainty in each parameter was then taken to be the difference between the best-fit value and the extreme (upper and lower) values which resulted from the Monte Carlo process. The radial velocity curves are shown in Figure 2.3, with the best fits represented by the sinusoidal curve in each case.

2.5.2 The 1997 data

As before, separate radial velocity curves were obtained for the Hγ, HeI (4471Å), and HeII (4542Å) lines. The resulting sets of velocities were fitted with a circular orbit solution with K_0 and a bias velocity as free parameters, and as above both the period and phase zero were

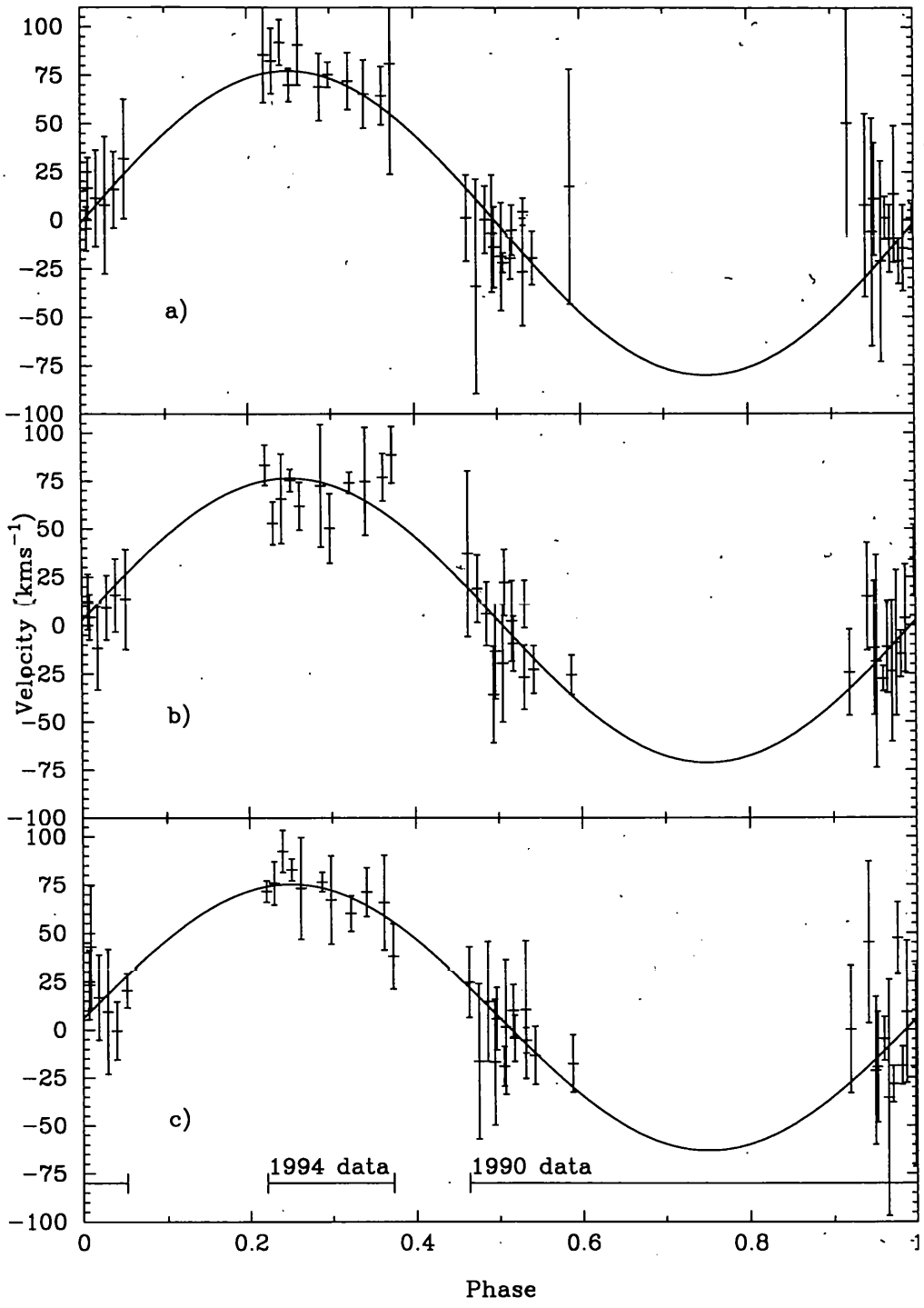

Figure 2.3 1990/1994 radial velocity curves of V779 Cen for a) Hγ, b) HeI (4471Å), and c) HeII (4542Å). Error bars have been rescaled such that the reduced χ^2 of the fit is equal to one.

fixed at the values given by Nagase et al (1992). Rescaling the error bars to give a reduced χ^2 of $\sim$1 for each radial velocity curve, and a subsequent Monte Carlo analysis, were carried out in exactly the same manner as with the earlier data set. The radial velocity curves for the 1997 data are shown in Figure 2.4 with the best fits represented by the curves as before.

A further radial velocity curve was obtained for the HeII (4686Å) emission line, following a similar analysis procedure except that phase zero was allowed as a third free parameter. The large radial velocity semi-amplitude indicated that this line did not originate from the optical companion, and so no assumptions could be made about its phasing. One possible origin for the observed emission could be a hot spot on the accretion disk due to the impact of the accretion stream. The data and fitted curve are shown in Figure 2.5.

2.6 Results

2.6.1 Spectral Classification

The spectral class of the optical component of Cen X-3 was determined to be O6-7II-III by comparison with the digital atlas of Walborn & Fitzpatrick (1990). In particular this is indicated by the relative strengths of the HeI (4471Å) and HeII (4542Å) lines. The relative strength of the Bowen blend (around 4640Å) at first led me to believe that the luminosity class might be Ia. However, a radial velocity curve for this emission feature was constructed following an identical analysis procedure to that used for the HeII(4686Å) emission line, and it was found that the Bowen blend has a semi-amplitude of $40 \pm 13 \mathrm{kms}^{-1}$, with a phasing that leads that of the measured absorption features by 0.21 ± 0.01. The data and fitted curve are shown in Figure 2.6. Both the relatively large radial velocity semi-amplitude and the phasing indicate that the Bowen blend emission does not originate from the optical companion, and so must be disregarded when making a spectral class determination.

The spectral classification obtained agrees with the accepted value of O6.5II-III (see, for example, van Paradijs 1995). Hutchings et al (1979) claim the spectral class may vary with phase, but our observations show no evidence for this.

2.6.2 The 1990/1994 radial velocity data

For each radial velocity curve, K_o was obtained as outlined earlier, then q was determined from Equation 1.1, and i was calculated from Equations 1.40-1.44. M_o and M_x could then be obtained from Equations 1.20 and 1.21. The results are shown in Table 2.1. For the H_γ results, i is undefined, as the right-hand-side of Equation 1.40 is slightly greater than unity

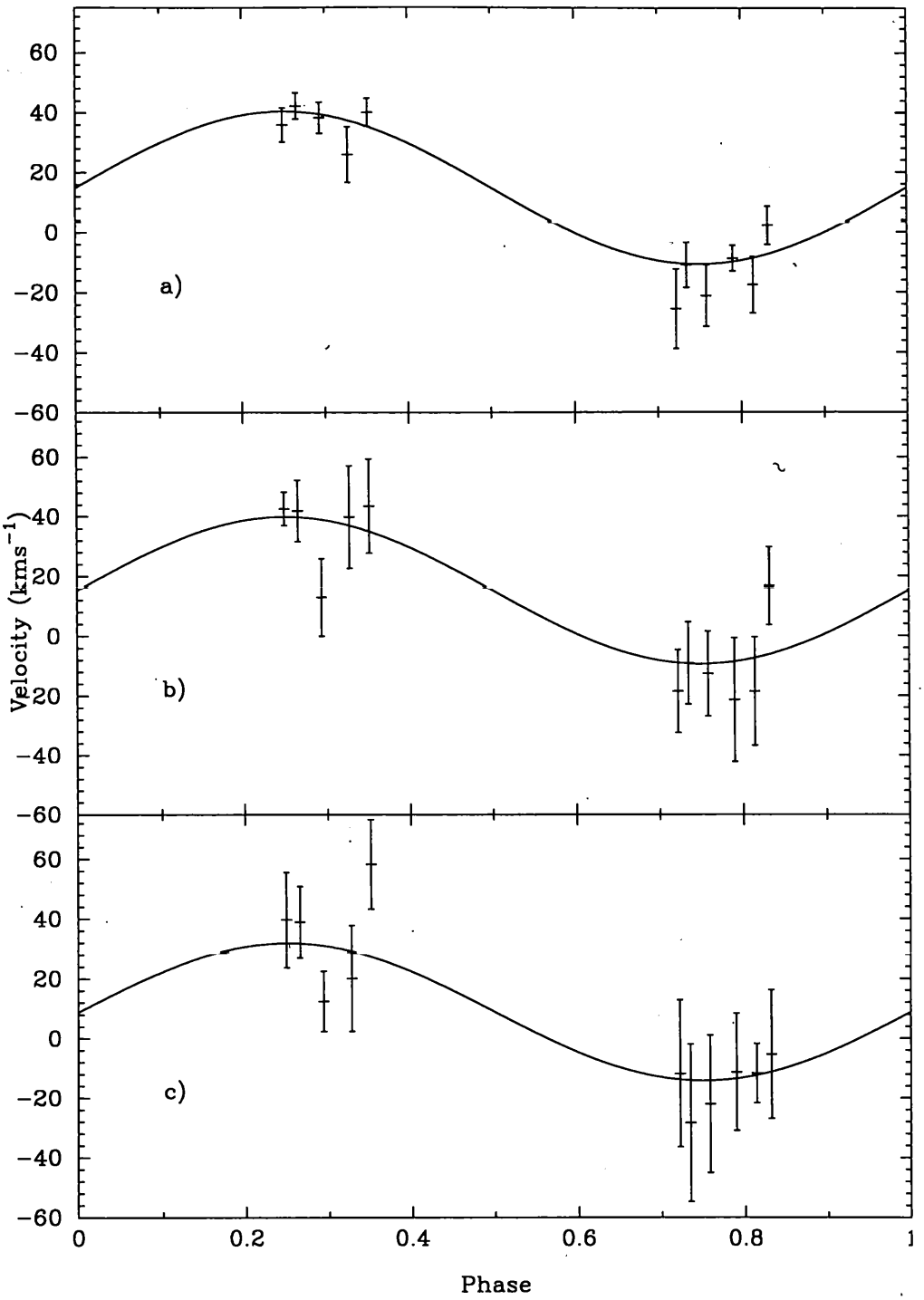

Figure 2.4 1997 radial velocity curves of V779 Cen for a) Hγ, b) HeI (4471Å), and c) HeII (4542Å). Error bars have been rescaled such that the reduced χ^2 of the fit is equal to one.

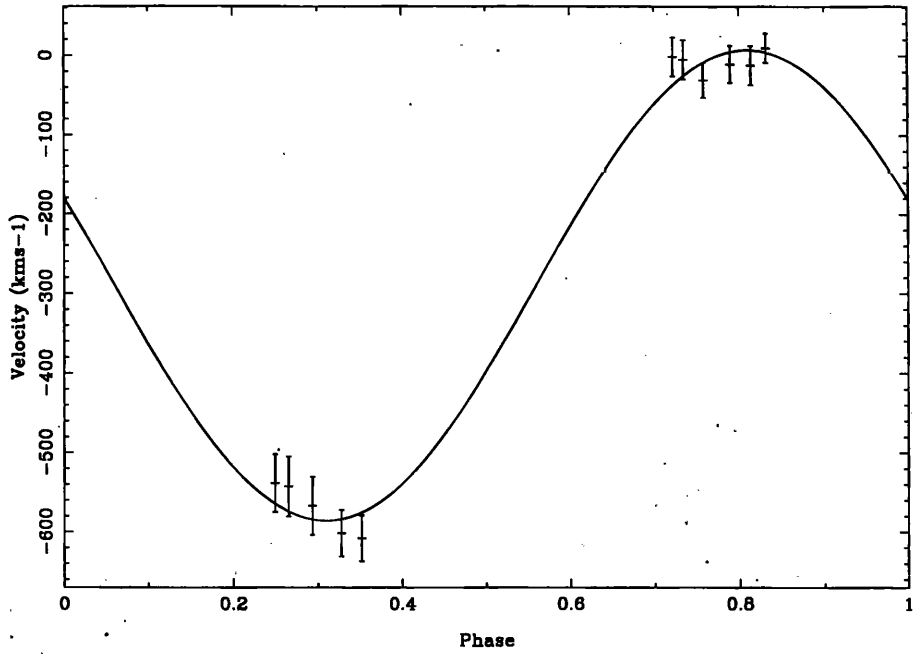

Figure 2.5 1997 HeII (4686Å) radial velocity curve of V779 Cen.

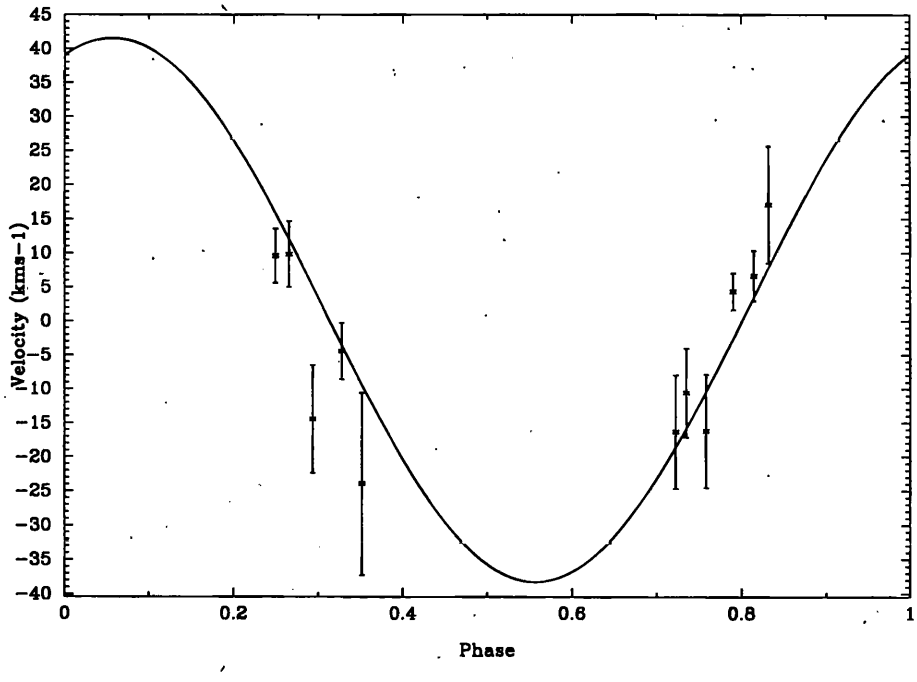

Figure 2.6 1997 Bowen blend radial velocity curve of V779 Cen.

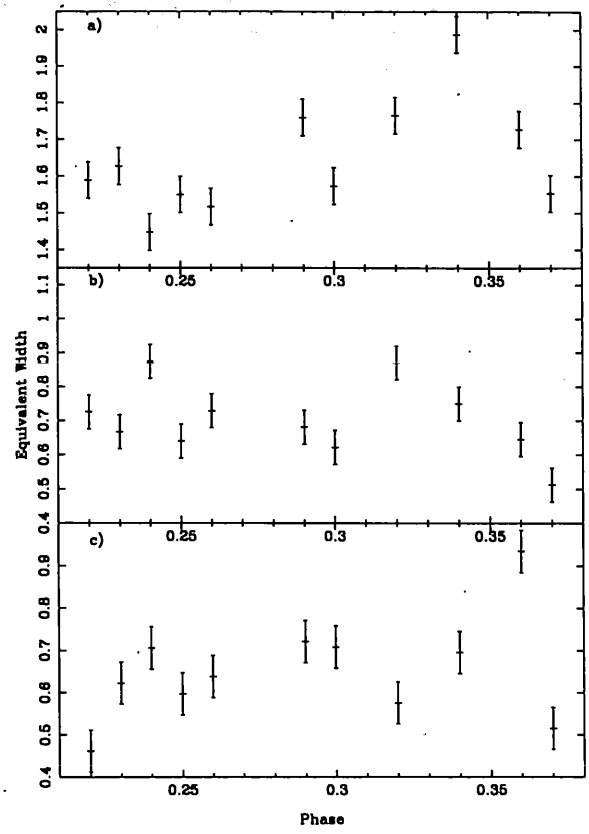

Figure 2.7 1994 dataset - equivalent width against phase for a) Hγ, b) HeI (4471Å), and c) HeII (4542Å).

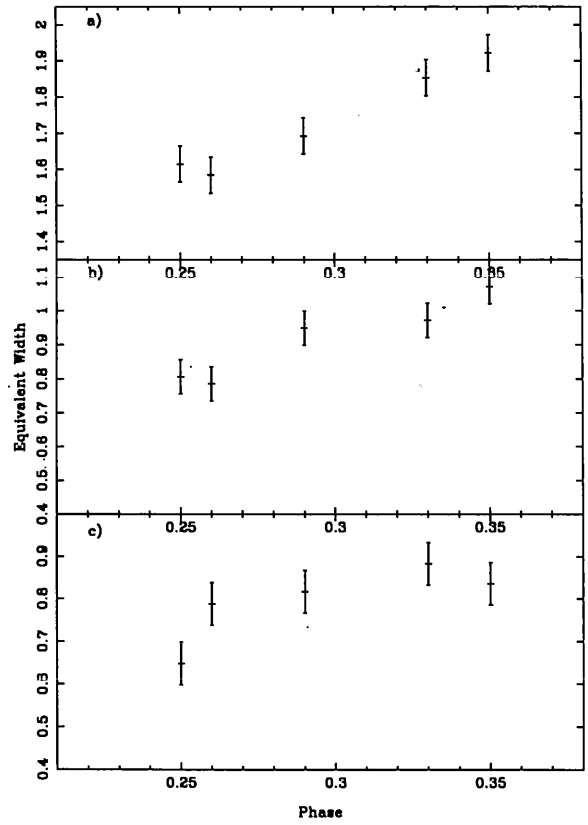

Figure 2.8 First night of 1997 dataset - equivalent width against phase for a) Hγ, b) HeI (4471Å), and c) HeII (4542Å).

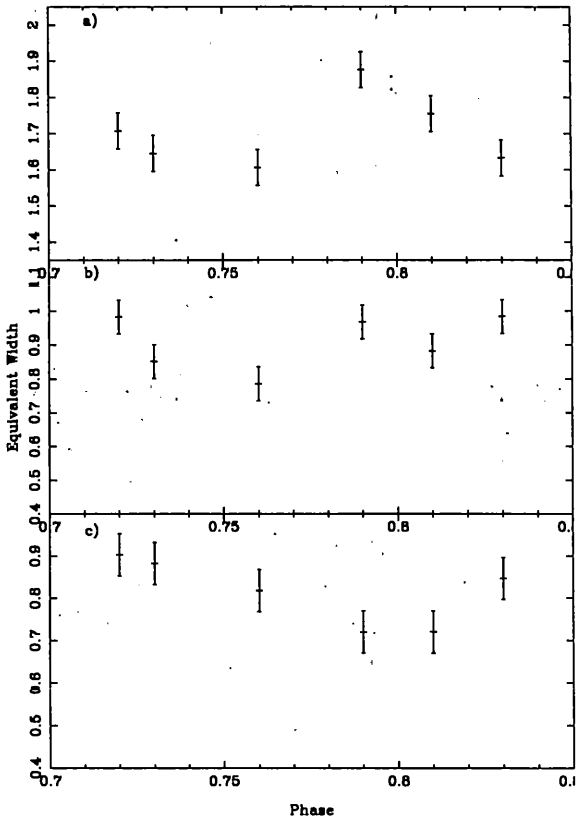

Figure 2.9 Second night of 1997 dataset - equivalent width against phase for a) Hγ, b) HeI (4471Å), and c) HeII (4542Å).

Table 2.1 Results for the 1990/94 dataset.

Line	K_o (km s^{-1})	M_o(M$_\odot$)	M_x (M$_\odot$)	i
Hγ	78.6 ± 9.0	21.62 ± 0.79	4.10 ± 0.62	undef.
HeI (4471Å)	73.9 ± 6.8	21.21 ± 0.59	3.78 ± 0.45	> 86°.8
HeII (4542Å)	72.9 ± 6.9	21.12 ± 0.60	3.72 ± 0.46	> 85°.9

Table 2.2 Results for the 1997 dataset.

Line	K_o (km s^{-1})	M_o (M$_\odot$)	M_x (M$_\odot$)	i
Hγ	25.6 ± 3.6	20.45 ± 0.60	1.26 ± 0.18	70°.8±2.5
HeI (4471Å)	24.6 ± 7.4	20.52 ± 0.96	1.22 ± 0.36	70°.3±4.2
HeII (4542Å)	23.0 ± 9.0	20.66 ± 1.27	1.15 ± 0.43	69°.6±5.1

(~1.01) although for the HeI and HeII lines, the lower limits to i are below 90°. Because of this, the mass values were calculated assuming $i = 90°$. Note that an undefined value for i corresponds to a situation where the system cannot produce eclipses of the observed length at *any* inclination angle.

2.6.3 The 1997 radial velocity data

For each radial velocity curve, K_o was obtained as outlined earlier and q, i, M_o, and M_x were determined using Equations 1.1, 1.20, 1.21, 1.40-1.44. The results are shown in Table 2.2.

The HeII (4686Å) curve (Figure 2.5) has a semi-amplitude of 296^{+19}_{-14} km s^{-1}, and its phasing leads the measured absorption features by 0.44±0.03. The phasing and relatively large radial velocity variations place the origin of this line near the neutron star. This feature was also noted by Mouchet et al (1980), who measured a semi-amplitude of ~ 400 km s^{-1}.

2.6.4 Equivalent width measurements

The equivalent width of a spectral line is a measure of the line's strength. If a spectral line is replaced by a rectangle of equal area with one dimension equal to the height of the continuum, the width of the rectangle represents the equivalent width. The equivalent width (EW) of an absorption line is sensitive to the temperature of the absorbing material. It was possible that the apparent temperature of the supergiant could vary, with phase due to X-ray heating and/or gravity darkening, or on another timescale due to wind variability. For this reason, it was decided to measure and compare the equivalent widths of the both nights of the 1997 dataset, to investigate EW variation with phase, and the 1994 dataset against the first night of the 1997 dataset, to investigate EW variation over a longer timescale.

The equivalent width measurements were made using the facilites available in the *IRAF*

splot package. This allows the user to interactively define the continuum level, then automatically normalises the region of interest, and calculates the equivalent width. These values were plotted against phase for the three cases of interest - Figures 2.7 - 2.9. It was found that the main source of error was in the initial definition of the continuum level, so the errors were estimated by examining the spread of results after performing the operation a number of times.

2.7 Discussion

When the 1990/1994 dataset K_o results are averaged, a value of $K_o = 75.1 \pm 4.4 \text{kms}^{-1}$ is obtained. The corresponding value for the 1997 dataset is $K_o = 24.4 \pm 4.1 \text{kms}^{-1}$. These two sets of results are clearly incompatible with each other and/or the assumption that the radial velocity of the lines chosen accurately reflect the radial velocity of the centre of mass of the supergiant. Either one or both of the data sets or the above assumption appears to be seriously flawed. Possible reasons for this discrepancy fall into two main groups - sources of error in the way the observations were made and the data reduced, and sources of error which are intrinsic to the system itself.

2.7.1 Observation and reduction

All the observations were made using from the same site, using the same telescope, spectrograph, although the grating and CCD detector varied. The Anglo-Australian telescope and the RGO spectrograph are heavily-used and over-subscribed instruments, and it is reasonable to assume that any systematic error present would be quickly detected and eliminated. It seems highly unlikely that the source of the error lies with any of the equipment used to make the observations and gone un-noticed.

All the data were reduced in an identical fashion using well-regarded pieces of software. The 1990 data were independantly reduced and analysised by Reynolds(1990), who obtained very similar results to my own. It also seems reasonable to assume that any error made at the reduction or analysis stages would affect both datasets equally whereas I am attempting to explain a mismatch between datasets. Therefore I believe that the source of error does not lie with either the way the observations were made or the data reduced, and so turn to possible sources of error which are intrinsic to the source.

2.7.2 Intrinsic sources of error

There are several possible sources of error when making radial velocity measurements of X-ray binaries, namely X-ray heating of the optical component by the compact component, contamination of the optical absorption spectrum by emission lines, tidal distortion of the optical component, the possibility of the system being in orbit around a third object, and stellar wind variations. Each of these will be discussed in turn.

X-ray heating occurs when the surface of the supergiant facing the neutron star experiences a temperature rise due to the X-ray flux from the neutron star. This can have the effect of changing the equivalent widths of the spectral lines originating from the heated area. To an observer, the equivalent widths of the spectral lines originating from the photosphere of the supergiant will appear to vary with phase. In the case of Her X-1 the X-ray heating effect is so extreme that the spectral class of the optical component appears to radically vary with phase. However, X-ray heating is an effect that is much more significant in systems in which the optical component is of relatively low mass and surface temperature, rather than a $\sim$ 20 $M_{\odot}$ O-type supergiant as in Cen X-3. Both Hutchings (1979) and Aslanov & Cherepashchuk (1982) claim there is evidence of X-ray heating in their spectra. Any X-ray heating effect would appear most strongly in the 1990 data, as it covers phases where the heated face would be at its most visible, and phases where the heated face would be completely hidden. However, Reynolds (1990) found no systematic variation of equivalent width with phase in this dataset. No spectral difference would be expected between the two phase-regions in the 1997 dataset if the optical companion was being heated symmetrically. Figures 2.8 and 2.9 appear to confirm this.

Another possibility is that of a change in X-ray heating which occured between the times the various datasets were obtained. The only way to investigate this is to compare the equivalent widths of lines from spectra observed at the different epochs, but which cover the same phase region. The only two datasets for which this is possible are the 1994 data, and the first night of the 1997 data, which occured at around phase 0.25 - 0.35. Figures 2.7 and 2.8 demonstrate that there is no great variation in equivalent width between the two epochs, and suggesting there was no change in the degree of X-ray heating. However, this approach cannot be extended to the 1990 dataset.

Due to the gravity of the neutron star, the shape of the supergiant will be distorted. As discussed in Chapter 1, this tidal distortion will introduce an error into the observed radial velocity. In the case of Cen X-3, these distortions were estimated by interpolating between model light curves calculated by Wilson & Sofia (1976). The resulting distortions

were small, < 5 km s^{-1}, and acted to lower the measured radial velocity semi-amplitude. Although this effect warrants further investigation in order to calculate the exact effect of the tidal distortion on our radial velocity curves, it cannot explain the anomalous results unless the distortions have changed in some way between the two epochs. To radically alter the distortions would mean a significant change in the masses of either the neutron star or the supergiant. It is highly unlikely that such a change could have occured between the 1990 and 1997 observations would have gone unnoticed.

Emission line contamination occurs when an emission line overlays an absorption line, and therefore alters its apparent shape. If the extent of the emission line contamination is variable, then the shape of the absorption line will vary too. This can introduce a very significant error if the line is used as part of a cross-correlation analysis to determine its radial velocity, as the apparent line centre may have been biased away from its "true" value.

In the case of our data, the extent of the effect of emission line contamination was gauged during the analysis of the data by cross-correlating over a number of different lines. However, since the difference between the 1990/1994 dataset and the 1997 dataset is much greater than the variation between the individual lines, there is no evidence that emission line contamination is the cause of the discrepancy between the two.

It is possible that a binary system may itself be orbiting a third object. A third object would cause a systematic error in the optical radial velocity curve, as the systemic velocity would be variable with time. This would introduce a low frequency modulation to the optical radial velocity curve, possibly explaining our incompatible datasets. However, although it is relatively common for binary systems to be in orbit around a third object, no X-ray binary has ever been observed to be orbiting a third object. A probable reason for this is that the supernova explosion that formed the compact object would provide enough kinetic energy for the binary to overcome the gravitational potential energy of any third object.

If Cen X-3 were to prove the exception to the above, then a third object would again cause a systematic error in the optical radial velocity curve, as the systemic velocity would be variable. In the case of Cen X-3, a third object would cause both the pulse-period history and the orbital-period history of the system to vary sinusoidally with a relatively long period. Both the pulse period and the orbital period of Cen X-3 have been monitored over the past twenty years using X-ray satellites, and indeed there is an apparent sinusoidal modulation of the pulse-period, with roughly a nine year cycle (Tsunemi et al 1996). Although this modulation is reminiscent of an orbit around a third body, Tsunemi et al (1996) discount this as there is no corresponding orbital-period modulation (Tsunemi 1989). So the possibility of a third object at a distance close enough to cause a non-negligible systematic error can

be ruled out.

The stellar wind of O-type supergiants such as found in Cen X-3 is highly variable both in density and structure. Any change in this outflow can change the apparent "rest" wavelength of a spectral line, causing a systematic error when spectra are collected over a period of time of the same order as the wind variation. This effect is unlikely to affect the 1997 dataset, but is a serious problem for the 1990/1994 dataset, where the spectra have been collected over a period of four years. The very poor phase coverage of the 1994 data, and the fact that it does not overlap in phase at any point with the 1990 dataset, means that it is impossible to determine if a change in the apparent systemic velocity has occurred. We believe this is the likely cause of the discrepant radial velocities observed in the 1990/1994 observations. The wind variation effect is clearly much less of a problem for the 1997 dataset, as all the spectra were obtained on two consecutive nights, during a single binary orbit. However, we note that there is no evidence for equivalent width variations between the 1994 data, and the $\phi \sim 0.25$ 1997 data.

The later dataset is also superior to the earlier dataset in that it samples both radial velocity maximum and minimum, the two regions which together best constrain the radial velocity curve. Finally, another problem with the 1990/1994 results is that they suggest that the system is unable to produce eclipses of the observed duration. Therefore the 1990/1994 results are disregarded in favour of the 1997 data.

2.7.3 A value for the mass of the neutron star

To arrive at a final result, a mean value for K_o was calculated for the three radial velocity curves obtained in 1997. We therefore take the radial velocity semi-amplitude of the optical component of Cen X-3 to be 24.4 ± 4.1 km s^{-1}. The eccentricity of the system, e, is known to be 0 (Nagase et al 1992), and it is assumed that Ω, the ratio of the rotational frequency of the optical component to the orbital period is equal to 1. This seems reasonable as the orbit has circularised, and the process of tidal locking takes place over a similar timescale. Additionally, Roche-lobe overflow is known to be taking place. Taking the value of K_x to be 414.1 ± 0.9km s^{-1} (Nagase et al 1992), this results in a mass ratio, q, of 0.059 ± 0.010, from Equation 1.1. Using this value for q, and a value of $32°.9 \pm 0°.5$ for θ_e (Clark et al 1988), a value of $70°.2 \pm 2°.7$, is obtained for the inclination of the system, i, from Equations 1.40-1.44. Thus from Equation 1.20, we obtain a value of 20.5 ± 0.7 M$_\odot$ for M_o, the mass of the optical companion, and from Equation 1.21, we obtain a value of 1.21 ± 0.21 M$_\odot$ for M_x, the mass of the neutron star. This value is consistent with the value of $M_x = 1.23 \pm 0.60$ M$_\odot$

of Clark et al (1988), but has a smaller uncertainty.

We have no reason to doubt the 1997 data, and the mass solution derived from them, as they stand. From these data alone there is no evidence to suggest that the mass of the neutron star in Cen X-3 is anything other than the canonical value of 1.4 $M_{\odot}$. However, since the 1990/1994 data show that Cen X-3 can undergo periods when the measured radial velocity is clearly anomalous and does not represent the orbital motion of the companion star, there must remain a concern about the validity of *any* mass determination carried out using this method on this particular object, and indeed on high mass X-ray binaries in general. The best that can be done is to acquire data over a single complete orbit (as we have done here in 1997) and, since the velocity excursions tend to increase the measured radial velocity, to believe the data that yield the *lowest* radial velocity amplitude. In the light of this, neutron star mass values determined for Cen X-3 using this technique may only represent upper limits to the true mass.

Appendix - Cross-correlation results for all datasets.

Table 2.3 Cross-correlation results for H_γ, HeI(4471Å) and HeII(4542Å). Uncertainties quoted are the raw uncertainties returned from the cross correlation, and have not been rescaled to force the reduced χ^2 of the fit to unity.

Date	JD	Phase	Radial velocities (km s^{-1})		
			H_γ	HeI (4471Å)	HeII (4542Å)
7/03/90	2447958.94	0.49	−6.9 ± 4.7	−35.7 ± 5.9	−16.9 ± 7.8
7/03/90	2447958.96	0.51	−18.8 ± 4.3	−19.3 ± 7.2	−19.1 ± 2.5
7/03/90	2447958.99	0.52	−19.8 ± 1.7	2.5 ± 4.9	9.9 ± 3.3
7/03/90	2447959.02	0.53	−26.8 ± 4.3	−26.7 ± 3.9	10.3 ± 8.5
7/03/90	2447959.14	0.59	17.5 ± 9.4	−25.4 ± 2.4	−17.7 ± 3.6
8/03/90	2447959.89	0.95	−6.1 ± 9.1	−11.6 ± 8.1	−21.4 ± 9.2
8/03/90	2447959.91	0.96	−21.3 ± 8.0	−27.6 ± 1.5	−4.8 ± 2.7
8/03/90	2447959.94	0.97	−9.6 ± 2.7	−23.7 ± 8.6	−28.4 ± 2.3
8/03/90	2447959.96	0.98	−21.2 ± 1.8	−14.8 ± 2.8	−18.7 ± 2.4
8/03/90	2447960.01	0.01	−4.5 ± 1.7	12.2 ± 3.3	23.3 ± 4.3
8/03/90	2447960.03	0.02	11.3 ± 3.8	−11.7 ± 5.0	16.8 ± 5.3
8/03/90	2447960.06	0.03	7.8 ± 5.5	9.2 ± 3.9	9.4 ± 7.7
8/03/90	2447960.08	0.04	15.8 ± 3.1	15.6 ± 4.4	−0.5 ± 3.6
8/03/90	2447960.10	0.05	31.7 ± 4.8	13.5 ± 6.0	20.4 ± 2.1
9/03/90	2447960.96	0.46	1.1 ± 3.4	37.4 ± 10.1	24.6 ± 4.4
9/03/90	2447960.99	0.47	−34.2 ± 8.5	19.2 ± 4.1	−16.5 ± 9.7
9/03/90	2447961.01	0.49	0.2 ± 2.7	6.2 ± 3.9	14.6 ± 7.4
9/03/90	2447961.03	0.50	−14.0 ± 3.2	−13.2 ± 5.8	5.7 ± 3.9
9/03/90	2447961.05	0.51	−22.0 ± 0.8	22.4 ± 4.0	1.4 ± 8.4
9/03/90	2447961.08	0.52	−5.3 ± 2.0	−9.3 ± 3.3	−4.5 ± 2.9
9/03/90	2447961.11	0.53	4.3 ± 1.1	11.2 ± 2.9	−5.5 ± 1.6
9/03/90	2447961.13	0.54	−19.5 ± 2.1	−22.7 ± 2.9	−13.4 ± 3.6
10/03/90	2447961.91	0.92	50.5 ± 9.1	−24.4 ± 5.2	0.1 ± 7.9
10/03/90	2447961.96	0.94	7.8 ± 7.3	15.0 ± 6.5	45.3 ± 10.0
10/03/90	2447961.98	0.95	11.0 ± 4.5	−18.7 ± 12.9	−19.6 ± 6.9
10/03/90	2447962.01	0.97	1.1 ± 1.7	−11.2 ± 5.6	−35.5 ± 14.7
10/03/90	2447962.03	0.98	13.6 ± 5.5	−9.1 ± 8.8	47.3 ± 4.4
10/03/90	2447962.06	0.99	−14.5 ± 3.4	3.7 ± 6.5	9.1 ± 8.8
10/03/90	2447962.08	1.00	1.1 ± 1.2	33.9 ± 4.3	−19.1 ± 12.5
10/03/90	2447962.10	0.01	16.6 ± 2.4	4.3 ± 2.7	42.9 ± 7.6
26/02/94	2449410.96	0.22	85.5 ± 3.8	83.4 ± 2.5	71.6 ± 1.3
26/02/94	2449410.98	0.23	82.4 ± 2.6	53.1 ± 2.6	75.9 ± 2.7
26/02/94	2449411.00	0.24	91.9 ± 1.8	65.9 ± 5.5	92.5 ± 2.6
26/02/94	2449411.03	0.25	69.9 ± 1.3	75.5 ± 1.4	82.9 ± 1.4
26/02/94	2449411.05	0.26	90.8 ± 3.2	62.1 ± 2.9	73.3 ± 6.3
26/02/94	2449411.10	0.29	69.0 ± 2.7	72.7 ± 7.5	76.5 ± 1.2
26/02/94	2449411.13	0.30	75.4 ± 1.0	50.5 ± 4.2	67.2 ± 5.5
26/02/94	2449411.18	0.32	72.1 ± 2.3	74.2 ± 1.3	60.2 ± 2.2
26/02/94	2449411.21	0.34	65.3 ± 2.7	74.9 ± 6.6	71.3 ± 3.0
26/02/94	2449411.26	0.36	64.5 ± 2.3	77.1 ± 2.9	65.8 ± 5.9
26/02/94	2449411.28	0.37	81.0 ± 8.8	88.8 ± 3.4	38.0 ± 4.0
12/05/97	2450580.86	0.25	36.0 ± 2.7	42.6 ± 1.4	39.6 ± 3.5
12/05/97	2450580.89	0.26	42.4 ± 2.1	42.0 ± 2.6	38.9 ± 2.6
12/05/97	2450580.95	0.29	38.3 ± 2.5	13.0 ± 3.3	12.4 ± 2.2
12/05/97	2450581.02	0.33	26.0 ± 4.4	39.9 ± 4.4	20.1 ± 3.9
12/05/97	2450581.07	0.35	40.2 ± 2.2	43.6 ± 4.0	58.2 ± 3.3
13/05/97	2450581.84	0.72	−25.6 ± 6.3	−18.5 ± 3.6	−11.8 ± 5.4
13/05/97	2450581.87	0.73	−11.1 ± 3.6	−9.1 ± 3.5	−28.3 ± 5.8
13/05/97	2450581.92	0.76	−21.3 ± 4.8	−12.6 ± 3.6	−22.0 ± 5.0
13/05/97	2450581.99	0.79	−8.9 ± 2.0	−21.4 ± 5.3	−11.3 ± 4.3
13/05/97	2450582.04	0.81	−17.7 ± 4.4	−18.5 ± 4.6	−11.7 ± 2.2
13/05/97	2450582.07	0.83	2.1 ± 3.0	16.8 ± 3.3	−5.4 ± 4.7

Table 2.4 Cross-correlation results for HeII(4686Å) and the Bowen blend. Uncertainties quoted are the raw uncertainties returned from the cross correlation, and have not been rescaled to force the reduced χ^2 of the fit to unity.

Date	JD	Phase	Radial velocities (km s^{-1})	
			HeII (4686Å)	Bowen blend
12/05/97	2450580.86	0.25	−538.5 ±11.8	9.6 ±1.5
12/05/97	2450580.89	0.26	−542.6± 12.2	9.8 ±1.9
12/05/97	2450580.95	0.29	−567.1± 11.9	−14.4±3.1
12/05/97	2450581.02	0.33	−601.9± 9.5	−4.4±1.6
12/05/97	2450581.07	0.35	−608.1± 9.4	−23.9±5.2
13/05/97	2450581.84	0.72	−1.4± 7.9	−16.3±3.2
13/05/97	2450581.87	0.73	−4.9± 8.0	−10.6±2.5
13/05/97	2450581.92	0.76	−30.8± 7.1	−16.2±3.2
13/05/97	2450581.99	0.79	−10.6± 7.5	4.3±1.0
13/05/97	2450582.04	0.81	−11.9± 7.9	6.6±1.4
13/05/97	2450582.07	0.83	9.7± 5.9	17.0±3.3

Table 2.5 Equivalent width results. All uncertainties are estimates based on the difficulty in defining the continuum.

Date	JD	Phase	Equivalent widths		
			Hγ	HeI (4471Å)	HeII (4542Å)
26/02/94	2449410.96	0.22	1.589 ± 0.050	0.725 ± 0.050	0.462 ± 0.050
26/02/94	2449410.98	0.23	1.627 ± 0.050	0.667 ± 0.050	0.623 ± 0.050
26/02/94	2449411.00	0.24	1.448 ± 0.050	0.874 ± 0.050	0.706 ± 0.050
26/02/94	2449411.03	0.25	1.550 ± 0.050	0.640 ± 0.050	0.597 ± 0.050
26/02/94	2449411.05	0.26	1.517 ± 0.050	0.729 ± 0.050	0.638 ± 0.050
26/02/94	2449411.10	0.29	1.761 ± 0.050	0.681 ± 0.050	0.721 ± 0.050
26/02/94	2449411.13	0.30	1.574 ± 0.050	0.621 ± 0.050	0.708 ± 0.050
26/02/94	2449411.18	0.32	1.766 ± 0.050	0.870 ± 0.050	0.576 ± 0.050
26/02/94	2449411.21	0.34	1.987 ± 0.050	0.750 ± 0.050	0.696 ± 0.050
26/02/94	2449411.26	0.36	1.728 ± 0.050	0.646 ± 0.050	0.934 ± 0.050
26/02/94	2449411.28	0.37	1.554 ± 0.050	0.512 ± 0.050	0.516 ± 0.050
12/05/97	2450580.86	0.25	1.614 ± 0.050	0.806 ± 0.050	0.648 ± 0.050
12/05/97	2450580.89	0.26	1.584 ± 0.050	0.786 ± 0.050	0.788 ± 0.050
12/05/97	2450580.95	0.29	1.692 ± 0.050	0.949 ± 0.050	0.817 ± 0.050
12/05/97	2450581.02	0.33	1.854 ± 0.050	0.972 ± 0.050	0.883 ± 0.050
12/05/97	2450581.07	0.35	1.922 ± 0.050	1.070 ± 0.050	0.836 ± 0.050
13/05/97	2450581.84	0.72	1.708 ± 0.050	0.982 ± 0.050	0.903 ± 0.050
13/05/97	2450581.87	0.73	1.646 ± 0.050	0.851 ± 0.050	0.882 ± 0.050
13/05/97	2450581.92	0.76	1.606 ± 0.050	0.785 ± 0.050	0.818 ± 0.050
13/05/97	2450581.99	0.79	1.876 ± 0.050	0.968 ± 0.050	0.720 ± 0.050
13/05/97	2450582.04	0.81	1.755 ± 0.050	0.882 ± 0.050	0.720 ± 0.050
13/05/97	2450582.07	0.83	1.632 ± 0.050	0.984 ± 0.050	0.846 ± 0.050

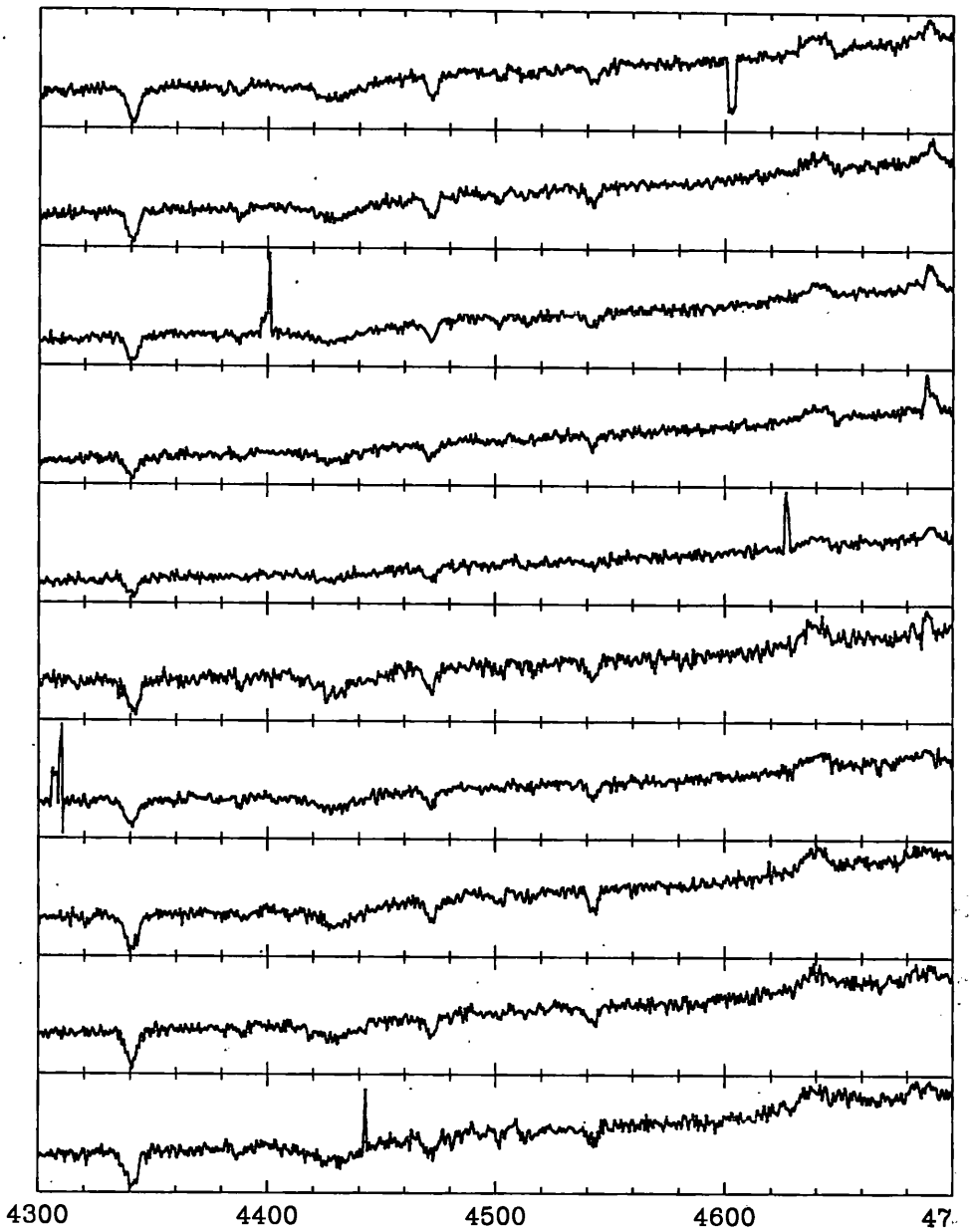

Figure 2.10 Cen X-3 spectra (March 1990)

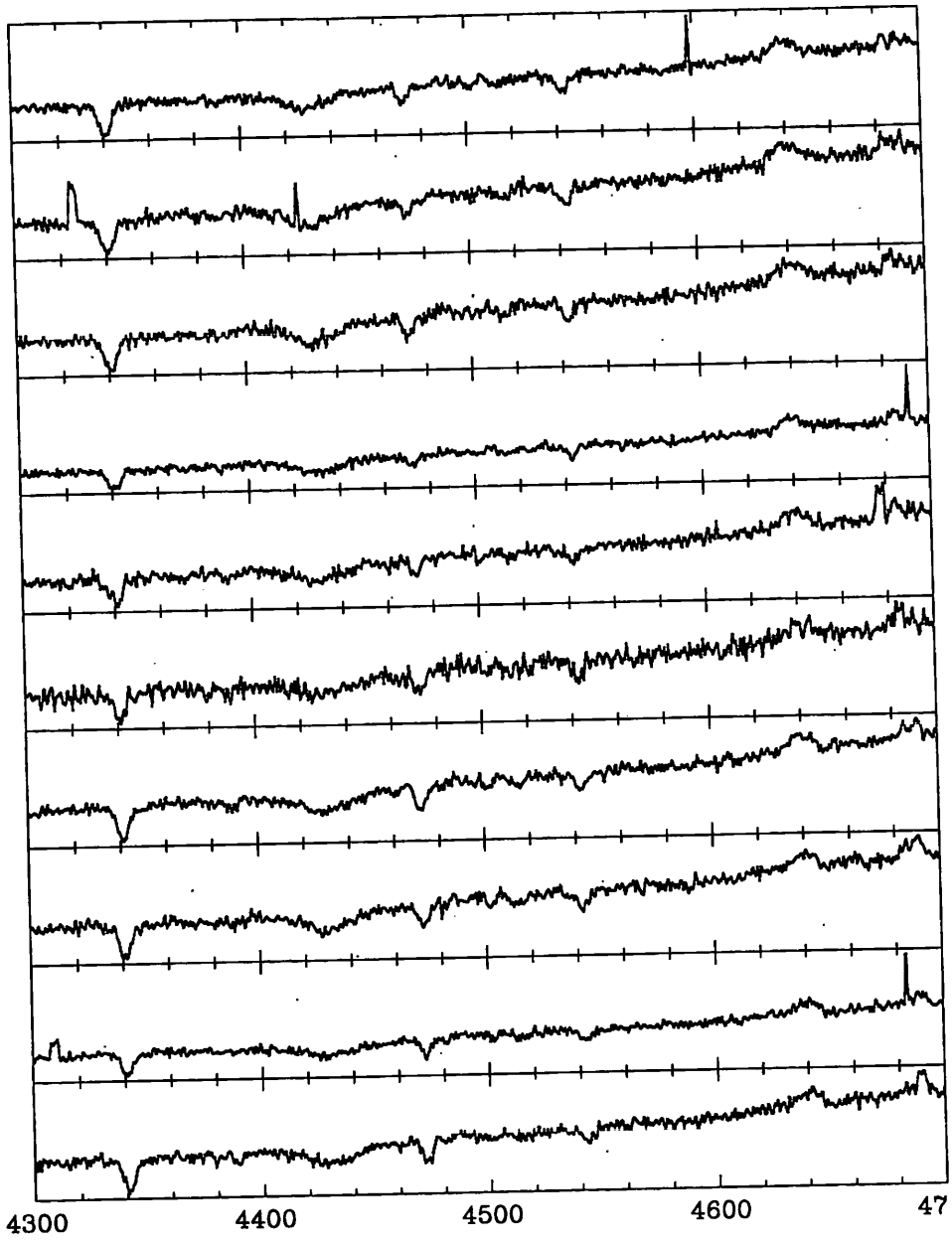

Figure 2.11 Cen X-3 spectra (March 1990) continued

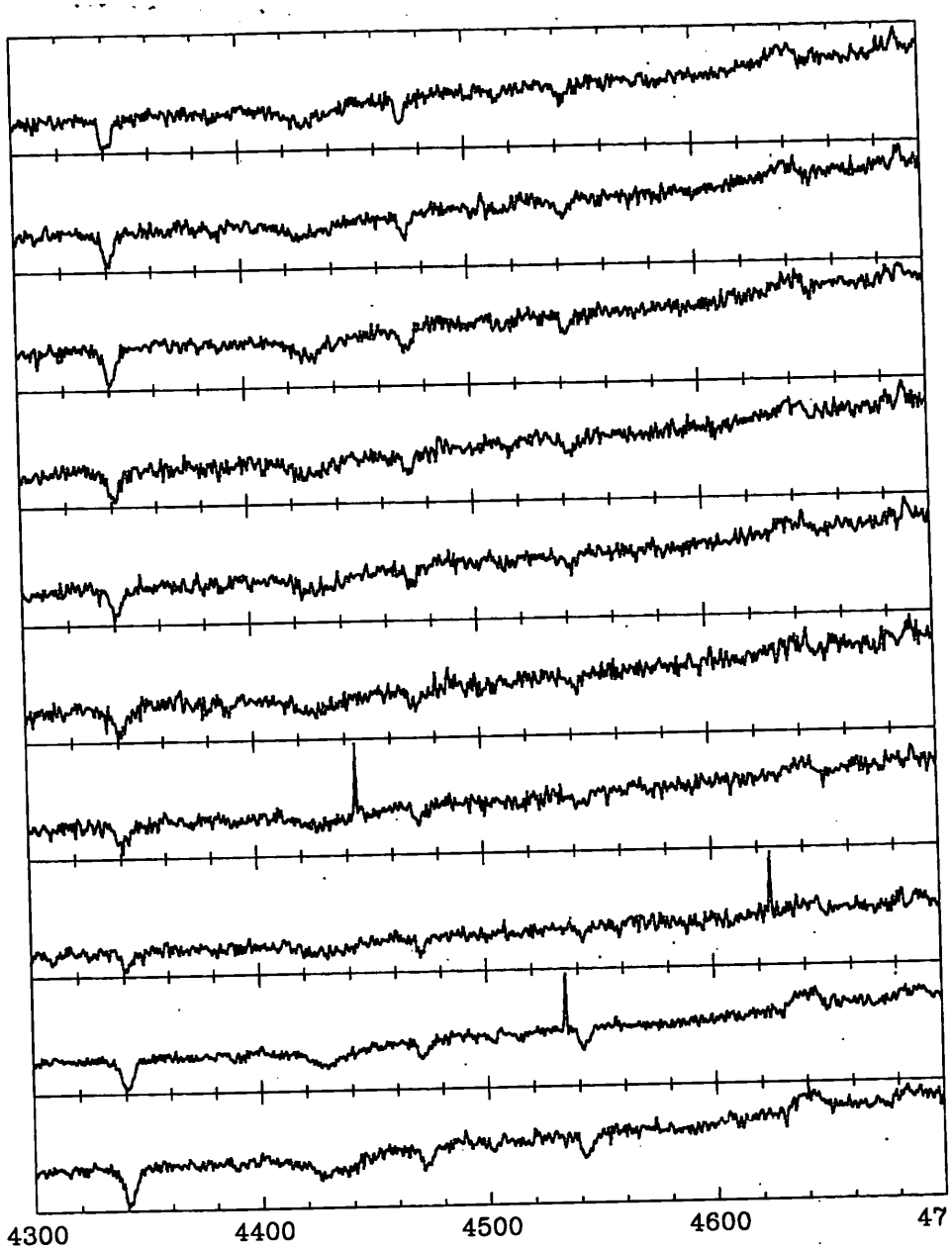

Figure 2.12 Cen X-3 spectra (March 1990) continued

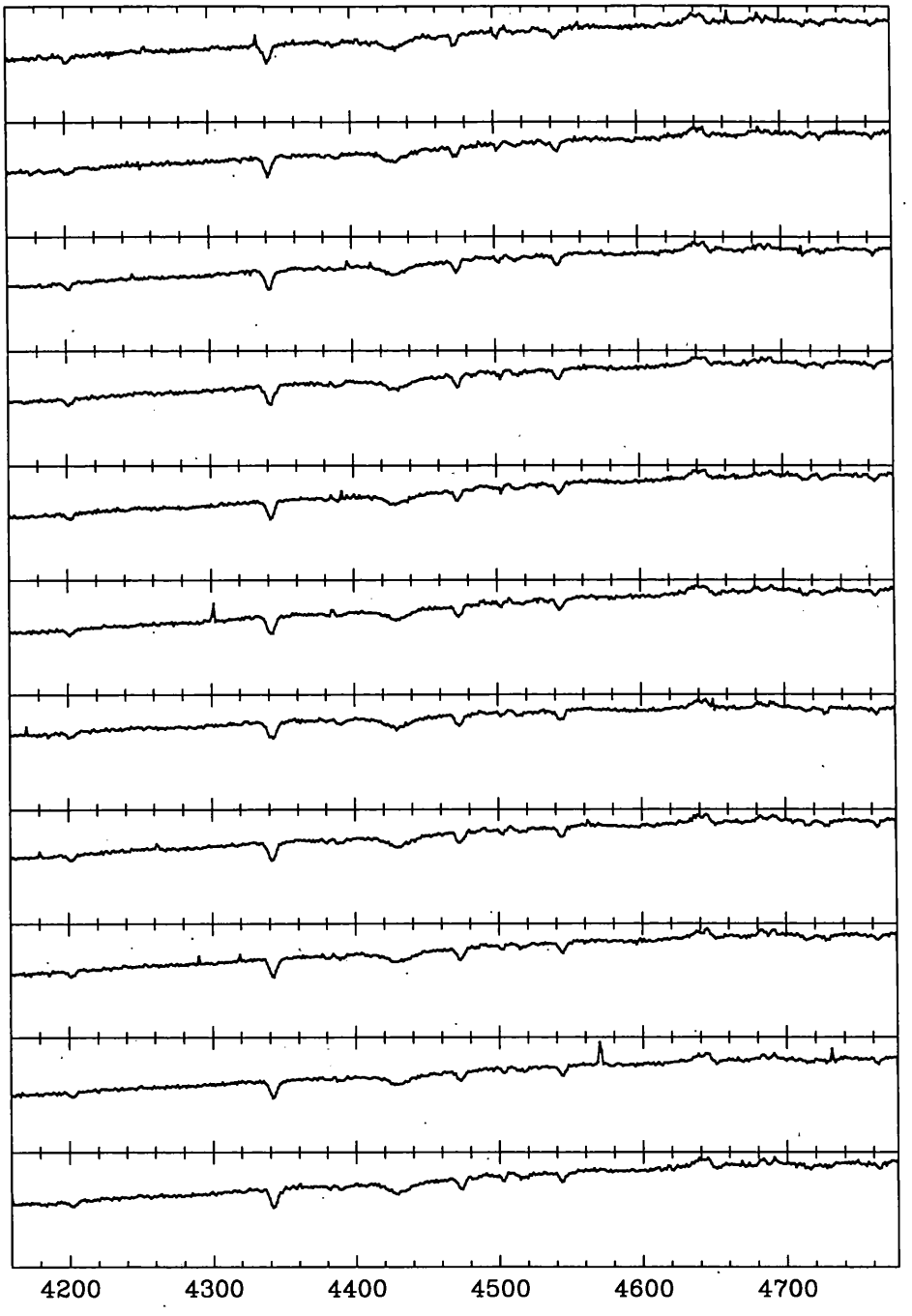

Figure 2.13 Cen X-3 spectra (February 1994)

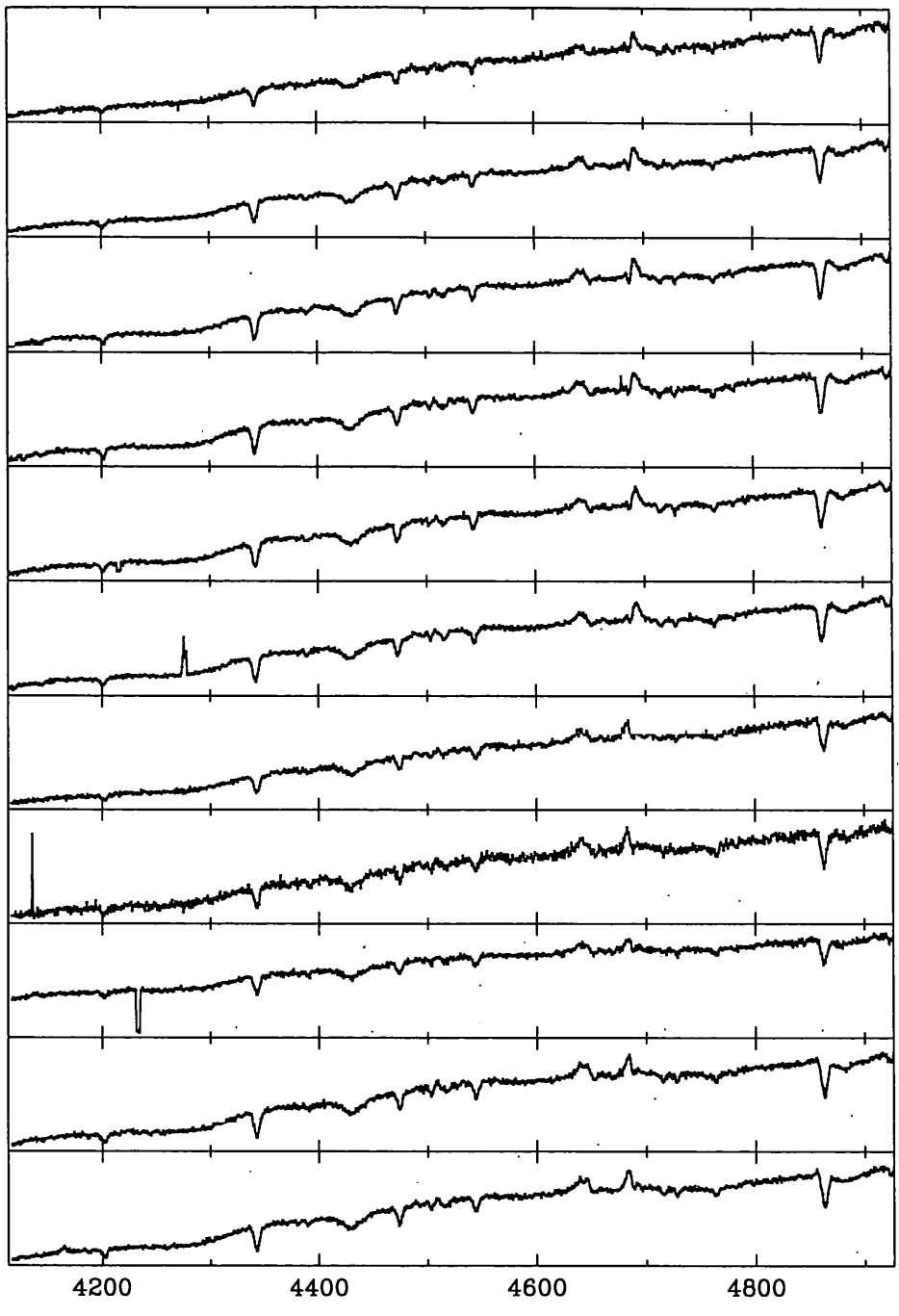

Figure 2.14 Cen X-3 spectra (May 1997)

Chapter 3

Radial velocity studies of Vela X-1

"The fault, dear Brutus, is not in our stars, but in ourselves ..."

William Shakespeare; Julius Caesar

3.1 Summary

This chapter deals with observations of Vela X-1 using the echelle spectrograph on the 74-inch telescope at Mount Stromlo Observatory. The historical background is reviewed, and echelle spectrographs are discussed in general. The observations and data reduction will be described, followed by a discussion of the resulting analysis and conclusion.

3.2 Historical background

3.2.1 X-Ray Observations and Optical Identification

Vela X-1 was first detected by a rocket-borne experiment consisting of a pair of proportional counters (Chodil et al 1967). Subsequent observations (see, for example, Giacconi et al 1972), suggested that the source was highly variable. Using data from the OSO-7 satellite, Ulmer et al (1972), demonstrated evidence for periodic intensity variations. The period of these variations, which were interpreted as eclipses, was around 9 days. An optical counterpart, HD 77581, a B0.5 giant with a relatively bright visual magnitude of 6.8 (ie almost visible to the naked eye) was identified by Brucato & Kristian (1972) and Hiltner et al (1972), based on its ultra-violet excess and radial velocity variations.

An X-ray pulse period of 283s was discovered using the SAS-3 satellite (Rappaport & McClintock 1975, McClintock et al 1976). Timing observations of these pulses by Rappaport et al (1976) allowed the radial velocity semi-amplitude of the X-ray component, K_x, to be

measured as 273 ± 9 km s^{-1}, and the eccentricity of the system, e, as ~ 0.1. More recent work (Deeter et al 1987a), quotes a value of 113.0 ± 0.4 light seconds for the projected semi-major axis, which corresponds to a K_x of 275 ± 1 km s^{-1}, and a value of 0.089 ± 0.03 for e, the eccentricity.

The X-ray eclipse duration appears to be quite variable, and somewhat energy dependent: Watson & Griffiths (1977) quote a value of $\theta_e = 33°.8 \pm 1°.3$. This is in contrast to previous determinations, for example Forman et al (1973) who obtained a value of $\theta_e = 38° \pm 1°$ using the Uhuru satellite, and Charles et al (1976) who obtained a value of $\theta_e = 39°.8 \pm 0°.4$ using the Copernicus satellite. However both these experiments were at much softer energies than Watson & Griffiths observed, and softer X-rays are much more likely to be absorbed by circumstellar material, thus extending the observed eclipse time.

As we saw in Chapter 1, these values can be combined with the radial velocity semi-amplitude of the supergiant, K_o, to yield mass estimates for the two components.

3.2.2 Optical Radial Velocity Observations

Early determinations of K_o were made by Wallerstein (1974) who obtained K_o = 37-45 km s^{-1}, and Zuiderwijk et al (1974) who obtained $K_o = 26 \pm 0.7$ km s^{-1}. As regular X-ray pulsations had yet to be discovered at this point, assumptions had to be made about the mass of the optical component in order to estimate the mass of the compact object. Zuiderwijk et al (1974) obtained a value of $M_x < 2.5 \pm 0.3 M_\odot$, and suggested that such a large mass coupled with the lack of regular pulsations indicated that the compact object was a black hole.

The discovery of regular X-ray pulsations provided a means of determining the masses of both components directly, and also ruled out the possibility of the compact object being a black hole. Van Paradijs et al (1976) combined the K_x value of Rappaport & McClintock (1975), with a K_o value of 20 ± 1km s^{-1} obtained from optical observations. From the X-ray eclipse data, they determined that the inclination, i, was $> 74°$, and thus arrived at a mass of $1.6 \pm 0.3 M_\odot$ for the neutron star.

Rappaport & Joss (1983) revised K_o to 22 ± 1km s^{-1} and the mass estimate to $1.9^{+0.4}_{-0.3} M_\odot$ by combining data from a number of sources, including Watson & Griffiths (1977), and Rappaport et al (1980), and performing a Monte Carlo analysis to estimate the uncertainties.

More recently, van Kerkwijk et al (1995) made further optical observations of Vela X-1, and discovered strong deviations from a pure Keplerian velocity curve, which were auto-correlated within a single night, but not from one night to another. It was suggested that

the variable gravitational force exerted by the neutron star as it travels around in its eccentric orbit excites short-lived pulsations on the surface of the optical component which affect the measured radial velocity. Van Kerkwijk et al (1995) obtained $K_o = 18.0 - 28.2\text{km s}^{-1}$, and $M_x = 1.9^{+0.7}_{-0.5}\text{M}_\odot$.

A significantly lower value for K_o of $17.8 \pm 1.6\text{km s}^{-1}$ was obtained from observations using the International Ultraviolet Explorer (IUE) by Stickland et al (1997). This corresponds to a value for M_x of between $1.34\text{M}_\odot$ and $1.53\text{M}_\odot$, depending on the inclination value adopted.

3.2.3 Eccentricity

Vela X-1 is unique amongst supergiant HMXRBs in that its orbit has a significant eccentricity. It is thought that tidal forces between the two components of such a close system would act to circularise the orbit on a short timescale. Either not enough time has elapsed for the circularisation to be complete, or some mechanism has delayed or prevented it.

The angle of the long axis of an eccentric orbit to the observer's line of sight is known as ω. Apsidal motion, or the rate of change of ω with time, $\dot{\omega}$, is a consequence of the binary components being extended objects rather than idealised point masses. The value of $\dot{\omega}$ depends on the radius and mass ratios, the rotational velocities, the orbital eccentricity, e, and the internal structure constants of the stars (Claret & Gimenez 1993). As a neutron star is essentially a point mass on the scale of a supergiant, the Vela X-1 system would appear to offer an opportunity to probe the internal structure of the optical component. However, $\dot{\omega}$ has been measured as $\leq 1^\circ.6\text{yr}^{-1}$ (Deeter et al 1987b) for Vela X-1, a value which cannot be used to constrain the internal structure in any meaningful way.

3.3 Echelle Spectrographs

As we saw in Chapter 1, standard spectrographs use a dispersing element (ie a grating or a prism) to produce a single spectrum of an illuminated slit. A much higher spectral resolution and wavelength coverage can be achieved by the use of an echelle spectrograph. The resolving power of a grating is given by:

$$\frac{\Delta\lambda}{\lambda} = \frac{1}{mn} \tag{3.1}$$

where λ is the wavelength, m is the order number, and n is the number of rulings on the grating (see, for example, Hecht 1987). A high spectral resolution can thus be attained by

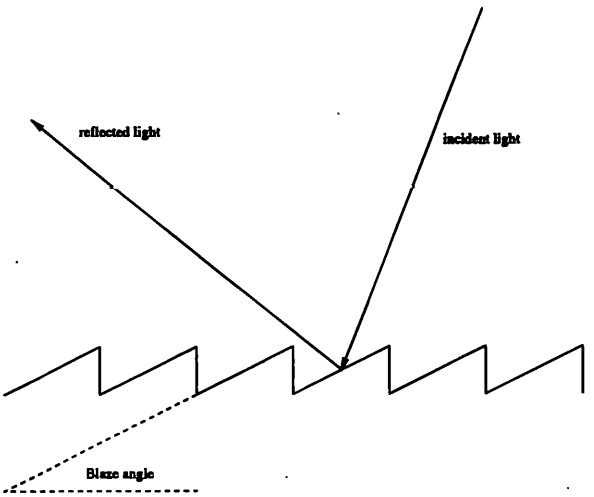

Figure 3.1 Schematic showing the operation of a blazed grating.

observing high orders, using a coarsely-ruled, high-angle grating. The blaze of a grating can be chosen so as to concentrate the diffracted light into the desired orders (see Figure 3.1).

However, there is the problem of free spectral range. The free spectral range is a measure of what extent lines from different orders will overlap, and is given by:

$$(\Delta\lambda)_{fsr} = \frac{\lambda}{m} \tag{3.2}$$

As the free spectral range is inversely proportional to the order number, high orders will be characterised by a very short free spectral range, or in other words, a number of overlapping orders. This problem is overcome in echelle spectrographs by use of a low-order cross-dispersing element. This device disperses the light diffracted by the first grating in a direction perpendicular to the first grating's dispersion direction. This has the effect of seperating the orders. The end result is a series of roughly parallel high-dispersion spectra. The echelle is usually designed so that the wavelength coverage in an order overlaps the coverage of adjacent orders. Using a detector, almost always a CCD camera, the various spectral orders can be recorded.

The advantages of echelle spectrographs are that a high spectral resolution can be combined with a wide wavelength coverage. In addition, as CCD detectors are generally square, good use of made of the available detecting area, in comparison to a traditional spectrograph. The disadvantages include the fact that the incident light from the observed object is

spread much more thinly than in a standard spectrograph. This means exposure times must be much longer to achieve an equivalent signal-to-noise ratio, degrading the time resolution. The reduction of echelle data is much more complex than traditional data for a number of reasons, for example: there is simply more data to deal with; accurate sky-subtraction can be difficult if the orders are close together; broad absorption lines can make determining the continuum level problematic; and the individual orders need to be merged to produce a spectrum covering the whole wavelength range.

3.4 Echelle Data Reduction

3.4.1 Bias subtraction

As with traditional CCD spectroscopic data (see Chapter 1), the first step in the reduction process is bias-correction. A number of CCD images with zero exposure are obtained during the observation. These images are then combined, by taking either the median or mean value for each pixel. The final bias frame is then subtracted from each object, arc, and flat frame.

3.4.2 Order Identification

The next step is to identify the approximate orientation of the orders across the CCD - whether the wavelength increases or decreases from left to right along the order, and the direction of increasing wavelength from order to order (taking the example of a echelle image where the orders are running approximately horizontally). This reduction software may be able to pick up this information from the header of the image file.

The reduction software can now attempt to identify the approximate position of each order on the frame. This is done by selecting a few central columns (or rows, depending which is perpendicular to the orders), combining them, and assigning each peak (representing an order) an order number. Figure 3.2 shows this process taking place. This means the software can be instructed to only reduce certain orders, in order to save time and computing resources.

3.4.3 Order Tracing

Once the software has identified the approximate position of each order, and the orders which are to be reduced, the appropriate orders can be traced. This process involves sampling the order at points along its length (ie in the dispersion direction), and attempting to find the

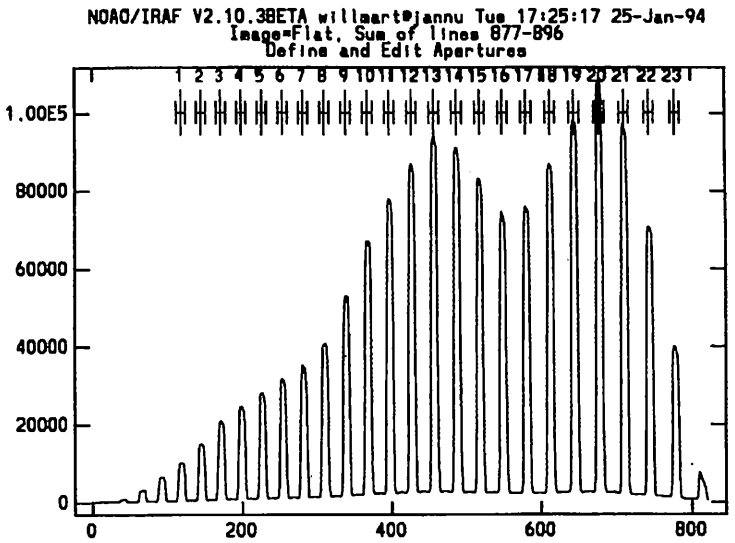

Figure 3.2 A cross-section of an echelle frame, showing the numbered orders.

centre of the order at each of these points. The software then attempts to fit a curve to these points in order to model the path of the order across the CCD frame. Problems often encountered at this stage are cosmic ray strikes, which appear as very localised areas (usually a single pixel) of very high signal. These tend to bias the calculated order centre away from the actual centre of the order. The software can also run into trouble if the order is not very bright, is strongly curved or contains strong absorption features. In these cases, it is common for the trace to "jump" from one order to the next, particularly if the orders are closely packed.

The usual procedure is to trace the orders for the object frame, then apply these traced orders to the associated flat and arc frames. If the object orders are too faint to trace, then a frame of a bright reference star could be used. Although flat frames would appear ideal for order tracing, their order profiles are flat due to the uniform illumination of the slit by the flat-field lamp, and this makes determining the centre of the order difficult.

3.4.4 Slit Definition - Order Profiling

When the orders of interest have been traced satisfactorily, the software needs to be informed of the position of the object and the inter-order background in the cross-dispersion, or spatial, direction (ie at right angles to the direction in which the order runs). This is usually done semi-automatically, as the software attempts to choose suitable object and background regions. Closely packed orders can cause problems in finding a reasonably large background region to sample. Note that scattered light from the echelle provides a large contribution

to the background level, whereas in traditional spectrographs, the sky provides most of the background light.

3.4.5 Flat Fielding

In standard echelle reduction, the pixel-to-pixel response variation of the CCD is now corrected for. For non-stable systems such as Cassegrain-mounted instruments, flat-fields must be taken immediately before or after the object frame, as the path of the orders will shift slightly as the telescope slews across the sky. For stable systems, such as a Coude-mounted instrument, flat-frames can be taken at the beginning or end of the night, just as for traditional spectrographic observations.

In either case, however, polynomials are fitted to the shape of the flat frame orders in the dispersion direction. The flat-field frame can then be normalised using the fitted polynomials, removing brightness variations due to the echelle itself (the blaze function - see later), leaving behind only the pixel-to-pixel variation. Pixels between the orders are set to one. This means that when the object frames are divided by the flat-field frames, the orders in the object frames are corrected for the pixel-to-pixel response variation, while the inter-orders regions remain unchanged. Note that for the reduction of our Vela X-1 data, the flat-fielding was performed in a different way to the above (see later).

3.4.6 Order Extraction

As we now have a model of each order of interest's path across the frame, a model of its profile in the cross-dispersion direction, and a model of the background signal, the software can now use an extraction algorithm to produce a spectrum from each order of interest. As with traditional CCD spectral frames, spectral extraction can be done using a linear extraction method, or an optimal extraction method. Linear methods simply sum all of the object pixels along the cross-dispersion direction to produce a value for the intensity at that wavelength. Optimal extraction, on the other hand, takes into account that pixels towards the edge of the order will have a smaller signal-to-noise ratio, and weights such pixels accordingly. Although this is much more computationally intensive, the resulting spectra will have a better signal-to-noise ratio than spectra extracted using a linear method, especially for relatively faint objects. Another advantage of optimal extraction is that it allows cosmic rays strikes to be automatically detected and removed from the resulting spectrum. However, for the extraction of arc frames, linear, not optimal, extraction should be used, as the emission features which an arc spectrum consists of are very similar to cosmic

ray strikes, and this confuses optimal extraction routines.

3.4.7 Wavelength Calibration

Assuming we now have a number of extracted objects and arc orders, the next step is wavelength calibration. The first task is to identify some features of known wavelength in the arc extracted orders. This can be problematic since each extracted arc order only covers a relatively short wavelength region, and so may not contain many emission features. Once several lines have been identified in a number of orders, a wavelength calibration model can be constructed for the entire echelleogram. This means wavelength calibration can be performed for all orders, regardless of whether they contain any identified lines. Once a satisfactory wavelength solution has been found, it may be copied to the object orders. *IRAF* allows the user to specify two bracketing arc frames per object frame, and interpolates a wavelength solution depending on the relative observation time of the three frames. This is especially useful for Cassegrain mounted echelles, as there is significant instrumental flexure as the telescope tracks across the sky.

3.4.8 Blaze correction

The next step is to correct for the "blaze" of the instrument. An echelle spectrograph directs relatively more light towards the centre of an order, and relatively less towards the edges, and the function describing this intensity variation is known as the blaze. To get flat spectra, this effect must be corrected for by fitting a curve to the continuum of each object order. The fitted curve is then subtracted from the object order to flatten out the spectrum. Difficulties can arise when observing objects with broad absorption lines, as there may not be much continuum in certain orders. In these cases a blaze function can sometimes be constructed by interpolating the fitted curves on either side of the affected order. Note that in our reduction process, we followed a non-standard routine to correct for the blaze function. This will be described later in the chapter.

3.4.9 Scrunching and Merging

The spectra may now need to be "scrunched" or re-binned to a fixed wavelength scale. For radial velocity work involving cross-correlation, the spectra will need to be re-binned to a fixed velocity interval. The *IRAF* package fxcor performs this step automatically, prior to the cross-correlation.

For some purposes, it may be necessary to merge the separate orders into a single high dispersion spectrum covering a wide wavelength region. As echelles are designed so that the edges of orders overlap to some extent, this can be done almost automatically by the software, but problems can occur when the blaze function of the echelle is not very bright at the order edges, causing poor signal-to-noise in the regions where the separate orders need to be joined together. This can lead to a highly variable signal-to-noise ratio across the final merged spectrum.

3.5 Observations

The observations were made using the 74-inch telescope at Mt Stromlo Observatory, Canberra, Australia. The echelle and CCD camera were mounted at the Coudé focus, which remains motionless however the telescope is orientated. This greatly aids instrumental stability, which is of particular concern for wavelength calibration. In turn, accurate wavelength calibration is crucial for measuring relatively small radial velocity shifts. A characteristic of Coudé focii is that the image formed appears to rotate as the telescope tracks across the sky. However, as HD77581 is a totally unresolved object this did not affect our observations. The 31.6 groove echelle grating, the 81.3 cm camera, and the thinned 2kx2k Tektronix CCD were used for all observations. The resolving power of the spectrograph was quoted as 53,333, which corresponds to 0.075Åper CCD pixel. The wavelength region covered was from approximately 3800-5200Å, though the signal-to-noise ratio rapidly decreased towards these two extremes. Around 70 seperate echelle orders fell onto the detector. To save disk space and shorten the readout time, 2x1 binning was used in the spatial direction on the CCD. Although, Mt Stromlo is no longer an ideal observing site due to light pollution from nearby suburbs, HD77581, the optical counterpart to Vela X-1, is bright enough at around 7 magnitudes for this to be a minor problem.

Twenty-one continuous nights (in order to cover two full orbits) were spent observing Vela X-1, by Ash, Fender, Quaintrell, Baldry, and Bedding. Ash was present throughout. Only two nights were completely lost to bad weather, although a few nights were affected by cloud to a lesser extent. An average of four sets of three spectra were obtained each night.

3.6 Analysis and Results

3.6.1 Reduction

The *IRAF* software package was chosen to perform the reduction and analysis steps. For each night's spectra, a bias frame was constructed by averaging the observed bias frames. The resulting average bias frame was subtracted from the arc, flat and object frames. After the approximate orientation of the orders on the frame had been specified, the software automatically detected the position of each order. The software also attempted to detect background regions, but due to the closely-packed nature of the orders, the results were unsatisfactory, and the background regions had to be indicated by hand. At this stage, it was decided to ignore the orders at the extreme edges of the echelle as they appeared to have a very poor signal-to-noise ratio.

Once the software knew the approximate position of each order, it could perform the order tracing almost unaided. Vela X-1 frames were chosen for the tracing process, as the object was relatively bright, and its early-type spectra does not contain many large absorption features which could complicate the tracing process. Again, the closely-packed orders caused the package a few problems, and the trace tended to "jump" from the correct order to an adjacent one. By monitoring the tracing process, it was possible to spot these errors and correct them.

Once the tracing was complete, the spectra were extracted. An optimal extraction algorthim was chosen to extract the object spectra to maximise the signal-to-noise ratio. This had the added advantage that cosmic ray strikes would be dealt with automatically. The arc and flat frames were extracted using a simple extraction algorthim, for the reasons outlined in Section 3.4.6 for the former, and simply to save time in the case of the latter. The flat frames were produced using an internal arc-light, and so had very high signal levels. The signal-to-noise ratio obtained using a simple extraction was more than adequate for our purposes, and the additional time required for optimal extraction would not be well spent.

The extracted arc frames were then wavelength calibrated. Although we were only interested in those orders which contained the absorption lines to be cross-correlated over, a wavelength calibration solution was found for the whole echelle frame (see Section 3.4.7). Because these spectra were to be used for the measurement of small radial-velocity shifts, this step was performed extremely carefully, and as many arc lines as possible were identified, to minimise the effect a mis-identification would have. It was also decided to take advantage of *IRAF*'s bracketing arc frame facilty (see Section 3.4.7) to minimise errors due to the movement and flexure of the telescope and spectrograph, even though the spectrograph

used was mounted at the Coudé focus, usually a very stable postion. Once the arc frames had been suitably calibrated, the wavelength solution was transferred to the object and flat frame orders.

At this point, the object orders containing the lines of interest (Hγ (4340Å), Hβ (4861Å), HeI (4026Å), and HeI (4471Å)), were identified. From this point on, only these orders were processed, in order to save time and computing power.

The flat-fielding and blaze-correction were performed in a single step, by dividing each object order by the corresponding flat frame order. This unusual method overcame a number of problems that had been encountered when attempting the more traditional technique described in Sections 3.4.5 and 3.4.8. Fitting polynomials to the object orders proved to be troublesome as a broad absorption line could dominate an entire order and make determining the continuum impossible. There was also concern that any emission features in close proximity with absorption lines would also make determining the continuum difficult. Fitting polynomials to the flat frame orders was easier, but still difficult due to the precision required.

The flattened orders resulting from this method were somewhat noisy towards the extreme edges, where the signal of the object and the signal from the arc lamp are both low, but as I had selected orders with the lines of interest more-or-less centred, this wasn't a great problem.

3.6.2 Analysis

As the all the observations were made on a single telescope run, it was decided not to calculate orbital phases for each observation. The radial velocity curve could be constructed by plotting the radial velocity measurements against time of observation. This approach had the advantage that any variability in the shape of the radial velocity curve from orbit to orbit would be more apparent.

The object spectra were cross-correlated using the *IRAF* package fxcor. It was hoped at first that a number of orders could be merged (see Section 3.4.9), so that a number of lines originating from the same ion could be cross-correlated over at once. Unfortunately, *IRAF* has a built-in limit to the number of pixels a single-order spectrum may contain of 8192. Each order contained up to 2000 pixels, and so only only around four or five contiguous orders could be merged. None of our desired line combinations (either the Balmer series, or the HeI series) were compatible with this somewhat arbitary restriction, and so it was reluctantly decided to cross-correlate over single lines only.

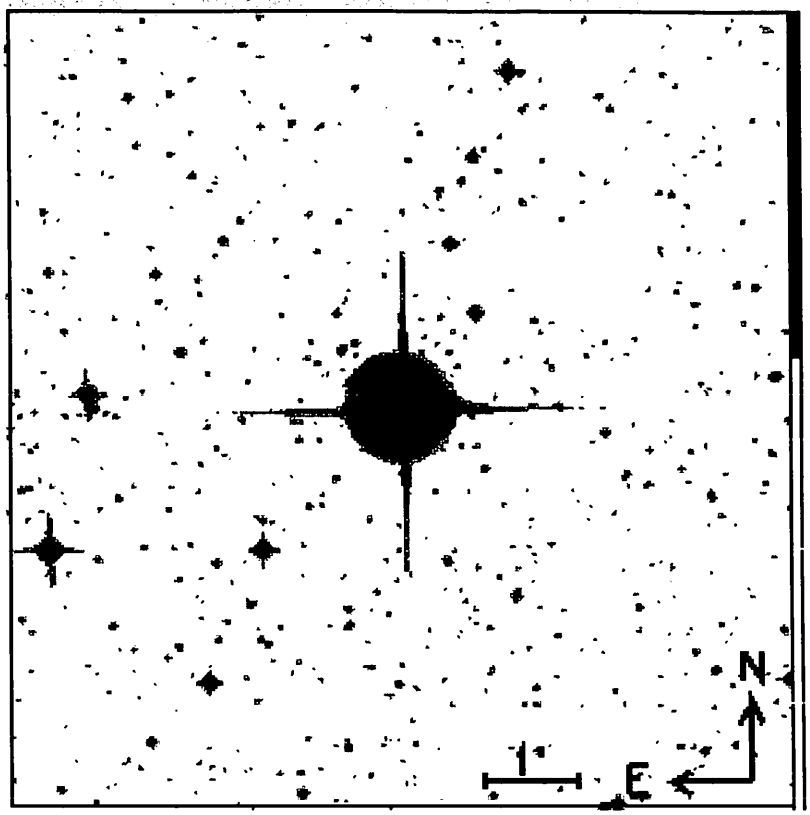

Figure 3.3 Optical finding chart for Vela X-1.

Before proceeding with the main cross-correlation, it was decided to check the stability of the detection system by cross-correlating the various spectra of the radial velocity standard HR 1829 against each other. As HR 1829 was known to have a stable radial velocity (relative to the barycentre of the solar system), the resulting radial velocity graph should be flat. For the orders that contained the lines of interest in Vela X-1, an average spectrum for HR 1829 was created. The individual HR 1829 spectra were then cross-correlated against this average, using the whole spectrum (in contrast to homing in on individual lines, as planned for the Vela X-1 spectra.) The resulting radial velocity graph (Figure 3.5) shows that a small, but potentially significant radial velocity drift was present.

The cause of this variation is still unknown, but as HR 1829 was a well-known radial velocity standard, it was assumed that the variation was not intrinsic to the star itself, but was an artifact introduced by some very slight variation in the telescope or detection system. It was also assumed that the drift would be present in the Vela X-1 spectra, and so would have to be corrected for.

Using a least-square fitting routine, a straight line was fitted to the HR 1829 radial velocity graph, and it was determined that the radial velocity drifted by 0.47km s^{-1} per

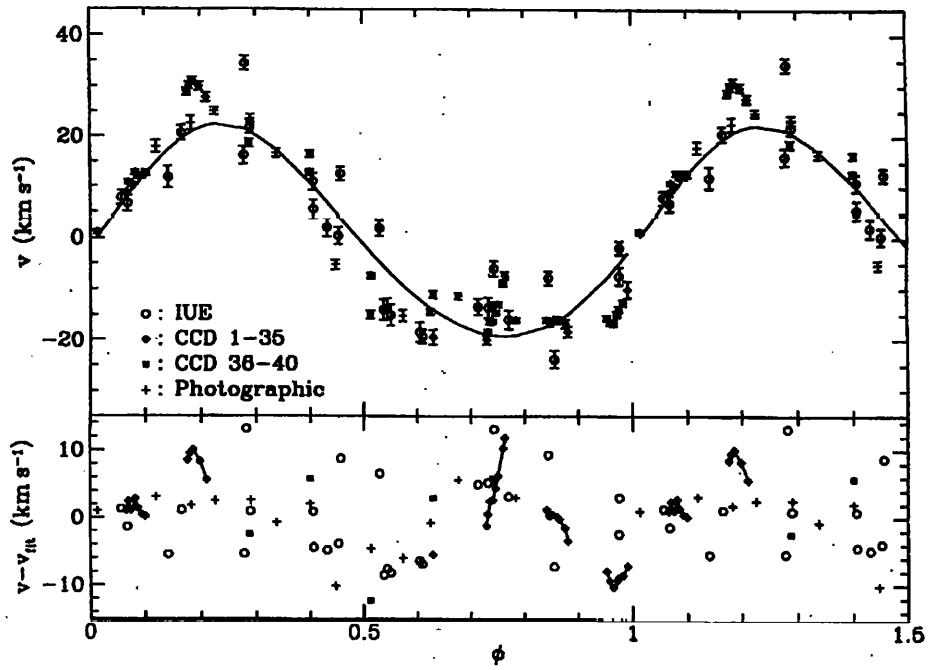

Figure 3.4 Radial velocity graph for Vela X-1 (van Kerkwijk et al 1995) showing velocity excursions.

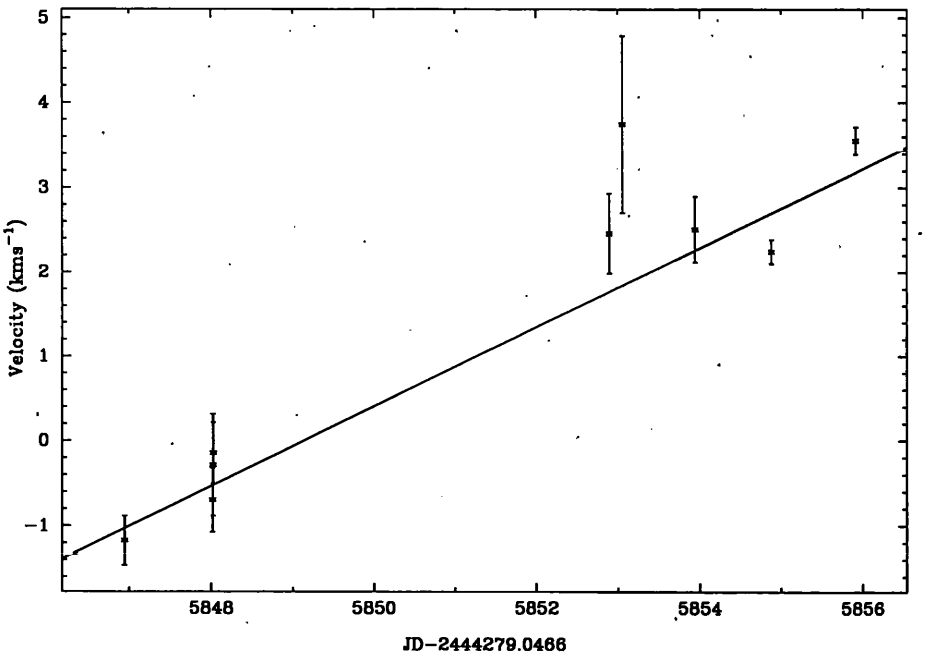

Figure 3.5 Radial velocity graph for radial velocity standard HR 1829 showing a small drift.

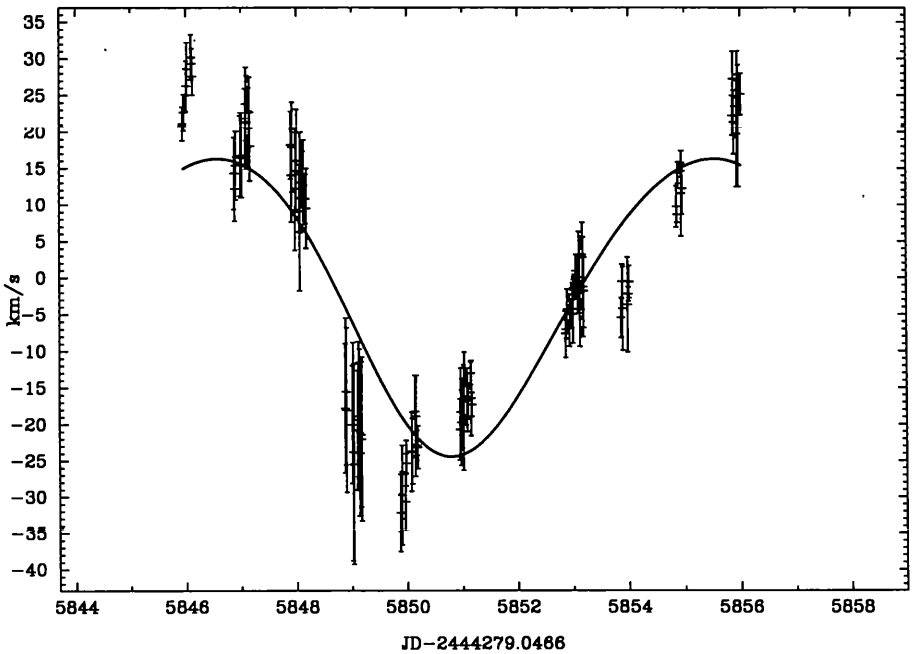

Figure 3.6 Radial velocity graph for Hγ(4340Å) showing fitted curve.

day. This drift was subsequently removed from all the Vela X-1 radial velocity results before any other analysis.

Radial velocity graphs were produced for Hγ (4340Å), Hβ (4861Å), HeI(4026Å), and HeI(4471Å). These are shown in Figures 3.6-3.9.

Because Vela X-1 has a significant eccentricity, simply fitting sinusoidal radial velocity curves to the cross-correlation results would not be satisfactory, as an eccentric orbit will show deviations from a pure sinusoid. Some means of fitting the eccentric orbit radial velocity curves must be found:

Consider an object in an elliptical orbit about a fixed point. The distance, r, from the object to the focus is given by:

$$r = \frac{a(1-e^2)}{1+e\cos\nu} \tag{3.3}$$

where a is the semi-major axis of the ellipse, e is the eccentricity, and ν is the true anomaly, the angle between the major axis and r. We are interested in radial motion, and so it can be shown geometrically that, z, the projection of r onto the line of sight (LOS) is given by,

$$z = r\sin(\nu+\omega)\sin i \tag{3.4}$$

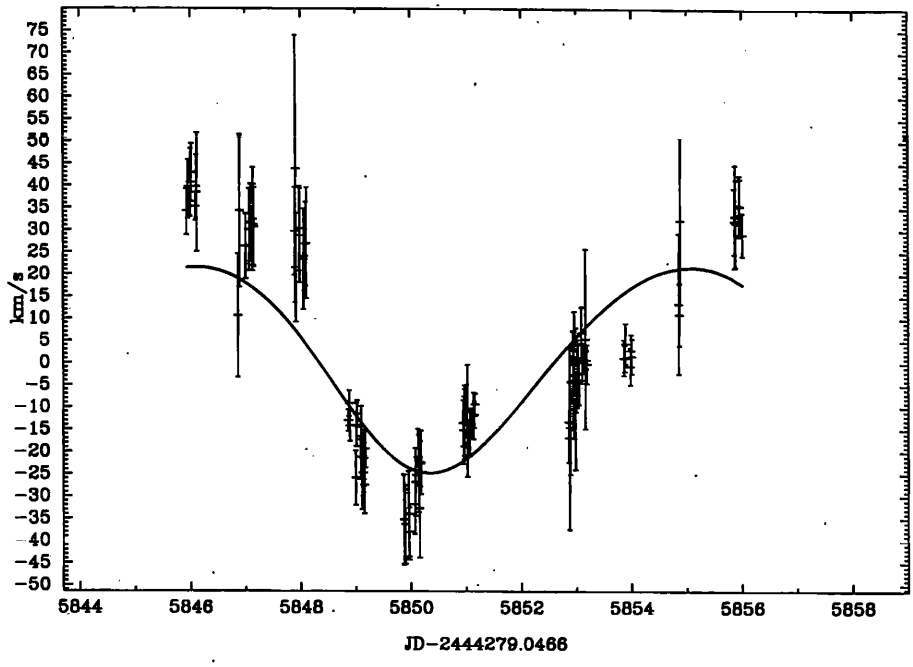

Figure 3.7 Radial velocity graph for Hβ(4861Å) showing fitted curve.

where ω is the angle between the LOS and the major axis of the orbit, and i is the angle between the normal to the plane of the orbit and the LOS. The observed radial velocity, v, will thus be given by,

$$v = \gamma + \frac{dz}{dt} \tag{3.5}$$

where γ is the radial velocity of the centre of mass of the binary system. Thus,

$$v = \gamma + \frac{d}{dt}\left(\frac{a(1-e^2)}{1+e\cos\nu}\sin(\nu+\omega)\sin i\right) \tag{3.6}$$

After much manipulation, we obtain:

$$v = \gamma + \frac{4\pi a \sin i}{P(1-e^2)^{\frac{1}{2}}}\left(\frac{e\cos\omega + \cos(\nu+\omega)}{2}\right) \tag{3.7}$$

where P is the orbital period. The true anomaly, ν, is related to the eccentric anomaly, E, by:

$$\tan\left(\frac{\nu}{2}\right) = \left(\frac{(1+e)}{(1-e)}\right)^{\frac{1}{2}}\tan\left(\frac{E}{2}\right) \tag{3.8}$$

E is the angle between the major axis of the ellipse and the line joining the position of the

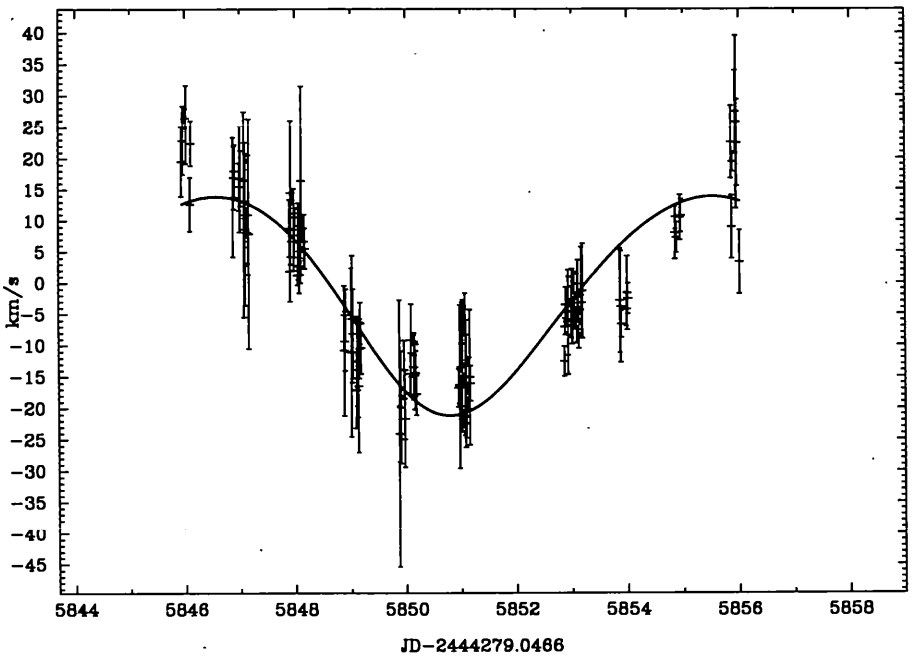

Figure 3.8 Radial velocity graph for HeI(4026Å) showing fitted curve.

object and the centre of the ellipse. In turn, E can be related to M, the mean anomaly, by Kepler's Equation:

$$E - e\sin E = \frac{2\pi}{P}(t - T) = M \tag{3.9}$$

M is equivalent to the orbital phase. This equation can be solved by the use of Bessel functions (it was in fact for this purpose that Bessel functions were developed), but it can also be solved numerically using, for example, Newton's Method:

$$x_{new} = x_{old} - \frac{f(x_{old}) - a}{f'(x_{old})} \tag{3.10}$$

Thus for a given set of system parameters, and a given orbital phase, the radial velocity of the orbiting object can be calculated.

Because each point on the model radial velocity curves has to be calculated separately, the least-squares curve fitting technique used in Chapter 2 for the Cen X-3 data is not suitable. It was decided instead to generate a number of model radial velocity curves with varying parameters and then measure how well each model curve described the actual radial velocity data.

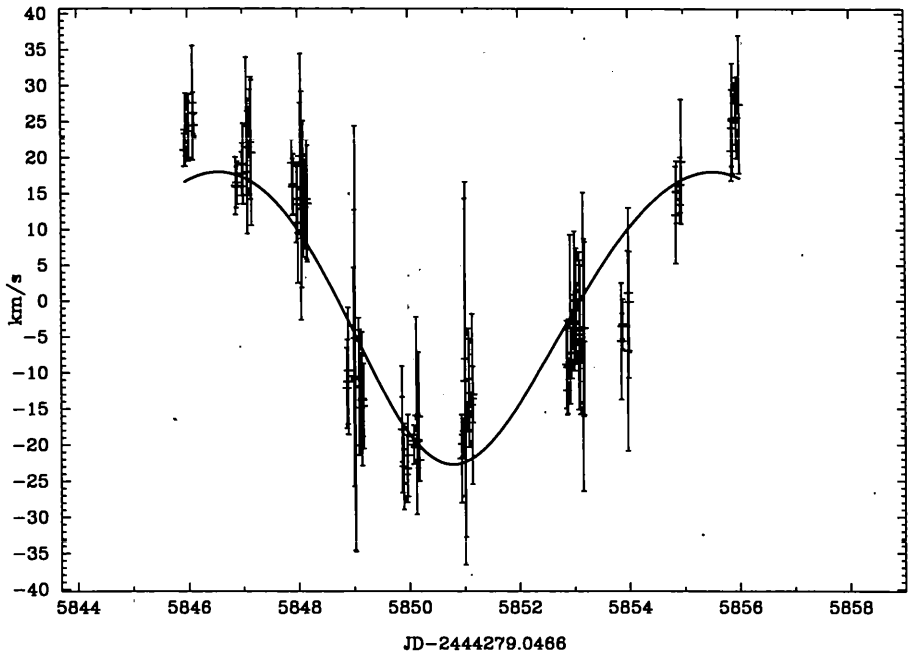

Figure 3.9 Radial velocity graph for HeI(4471Å) showing fitted curve.

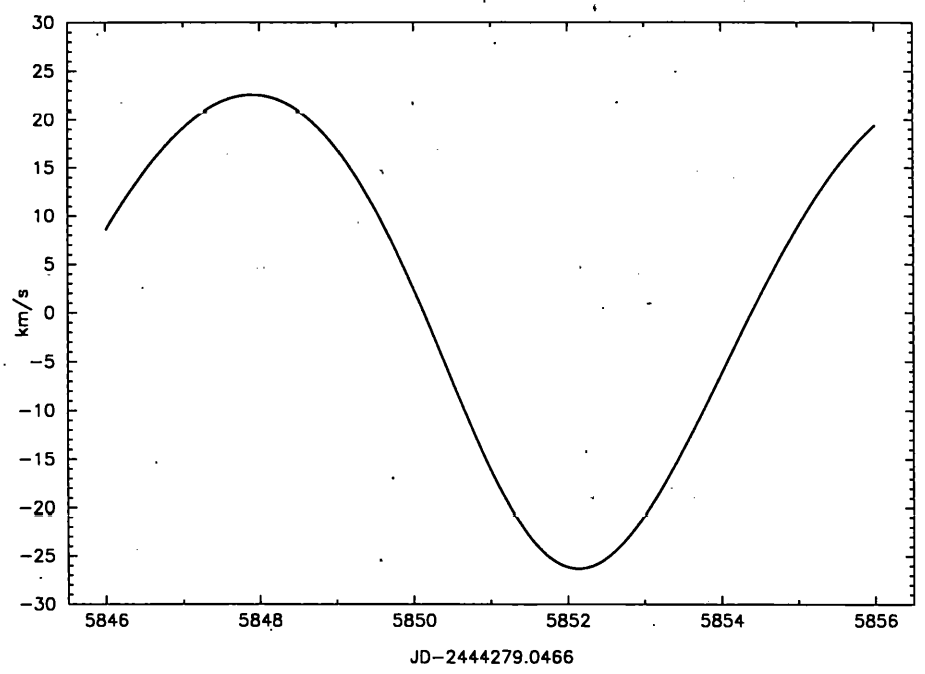

Figure 3.10 Model radial velocity curve: $a \sin i = 3 \times 10^6$km, phase offset $= 0.25$.

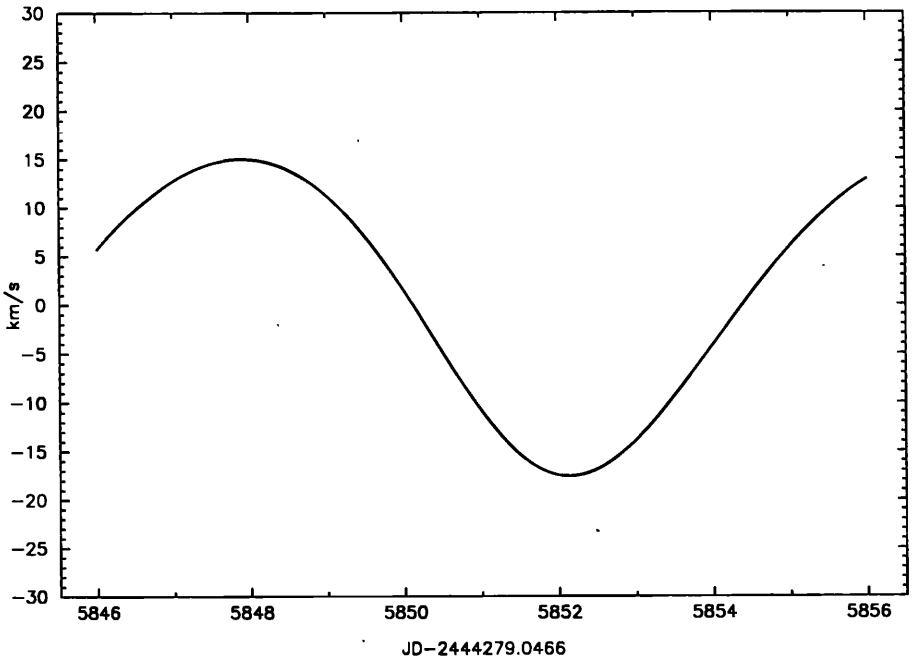

Figure 3.11 Model radial velocity curve: $a \sin i = 2 \times 10^6$km, phase offset = 0.25.

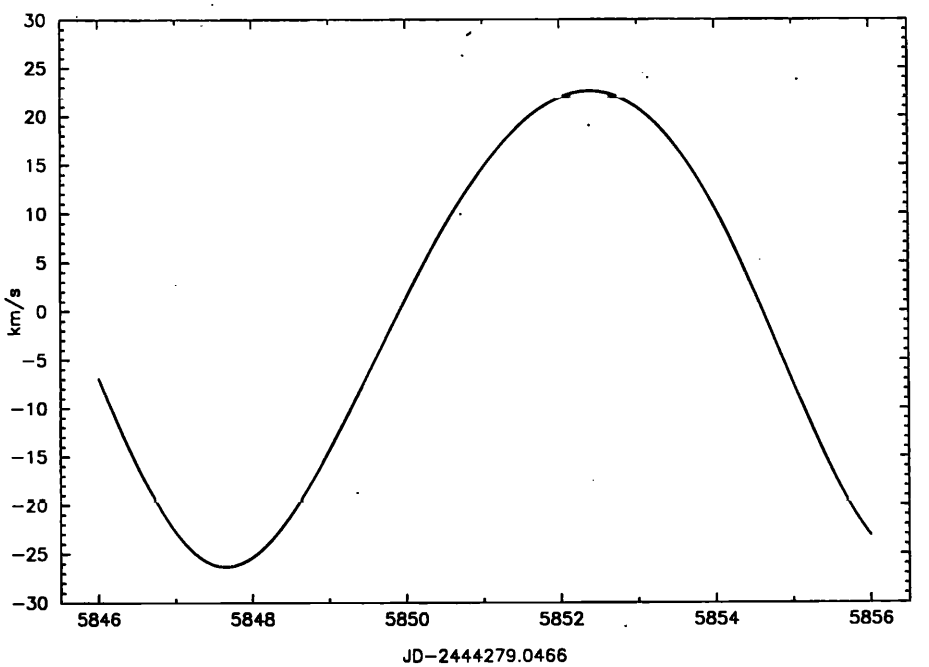

Figure 3.12 Model radial velocity curve: $a \sin i = 3 \times 10^6$km, phase offset = -0.25.

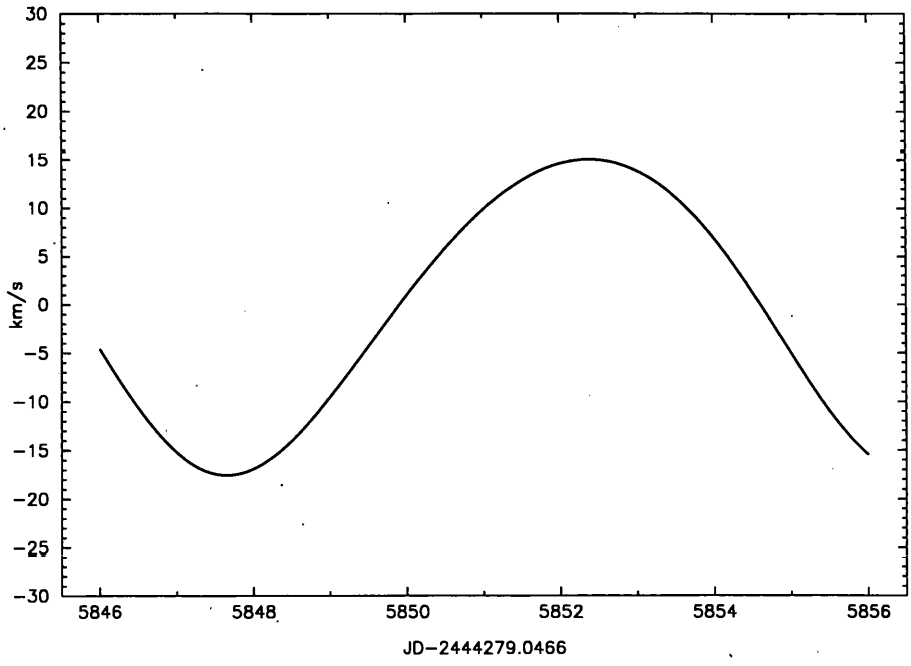

Figure 3.13 Model radial velocity curve: $a \sin i = 2 \times 10^6$km, phase offset = -0.25.

Three parameters were varied: $a \sin i$, from 1.5×10^6km to 3.2×10^6km in steps of 5×10^4km; a bias velocity, from -8km s^{-1} to 2km s^{-1} in steps of 0.1km s^{-1}, and a phase offset, which was varied from -0.5 to -0.5 in steps of 0.05. A three-dimensional grid of model radial velocity curves was thus generated. Four sample model curves are shown in Figures 3.10-3.13. The code written for this purpose can be found in at the end of this chapter.

To measure how well each model curve fitted the actual data, χ^2 was calculated in each case, (see Chapter 2 for further details.) The model curve with the lowest χ^2 was deemed to be the best-fit. The error bars were then re-scaled in order to achieve a χ^2 of 1, so that the error bars more accurately reflected the quality of the fit (see Chapter 2). To make an estimate of the uncertainties in the best-fit parameters, it was decided to use a Monte-Carlo technique similar to the one described in Chapter 2. For each actual radial velocity curve, 100 new radial velocity curves were generated by randomly choosing points with in the error bars of the existing points. These curves were then each fitted to the three-dimensional grid of models as described above, and the spread of the resulting best-fit parameters taken as the uncertainty in the best-fit parameters of the actual data. See Table 1 for the parameters obtained for each line. In the case of the phase offset, each of the 100 fitted curves for each

Table 3.1 Orbital parameters obtained for Vela X-1.

Line	$a \sin i \times 10^6$km	bias velocity(km s^{-1})	phase offset	K_o(km s^{-1})	mean K_o
Hγ	2.5±0.2	-2.5±0.2	0.4±0.025	20.4±1.6	20.10
Hβ	2.85±0.7	-1.1±3.0	0.4±0.025	23.2±5.7	23.79
HeI(4026Å)	2.15±3.5	-2.3±1.2	0.4±0.025	17.5±2.8	17.28
HeI(4471Å)	2.5±0.3	-0.8±1.4	0.4±0.025	20.4±2.6	20.69

Table 3.2 Orbital parameters obtained for Vela X-1.

Line	K_o(km s^{-1})	q	β	i	M_o(M$_\odot$)	M_x(M$_\odot$)
Hγ	20.4±1.6	$13.5^{+1.1}_{-1.0}$	0.932 ± 0.068	$77^{\circ}{}^{+13}_{-12}$	$23.6^{+5.5}_{-1.9}$	$1.77^{0.53}_{-0.27}$
Hβ	23.2±5.7	$11.9^{+3.9}_{-2.3}$	0.940 ± 0.060	$79^{\circ}{}^{+11}_{-14}$	$23.7^{+5.7}_{-2.2}$	$2.02^{+0.94}_{-0.64}$
HeI(4026Å)	17.5±2.8	$15.7^{+3.0}_{-2.2}$	0.924 ± 0.076	$76^{\circ} \pm 14$	$23.5^{+6.7}_{-2.1}$	$1.51^{+0.63}_{-0.38}$
HeI(4471Å)	20.4±2.6	$13.5^{+2.0}_{-1.5}$	0.932 ± 0.078	$77^{\circ} \pm 12$	$23.6^{+5.7}_{-2.1}$	$1.77^{+0.63}_{-0.36}$

line had a phase offset of 0.4, and so uncertainty was taken to be the size of a single step. The mean K_o is a mean of the K_o for all 100 fitted curves (for each line). It is included as a crude indication of the distribution of fitted solutions. In each case, it is very close to the best-fit value, demonstrating that the distribution is at least somewhat symmetrical.

3.7 Results

The masses of the two components were calculated according to the method described in Chapter 2. A value of $33^{\circ}.8 \pm 1.5^{\circ}$ was adopted for the eclipse half-angle, θ_e from Watson & Griffiths (1977). This value was also used by Wilson & Terrel (1998) for their unified analysis of Vela X-1. A value of 0.67 ± 0.04 was adopted for the co-rotation factor, Ω, obtained from comparison of Vela X-1 spectra with model line profiles by van Kerkwijk (1993). A value for β, the ratio of the radius of the supergiant to the radius of its Roche lobe, cannot be obtained from independent observations. As the neutron star does not seem to be accreting material via Roche-lobe overflow, the supergiant cannot be overfilling its Roche lobe, and so $\beta \leq 1.0$. There must also be some lower limit to β, as the supergiant must have a radius large enough to produce the observed eclipses. Using a value of 275 ± 1km s^{-1} for K_x (Deeter et al 1987), q was calculated using Equation 1.1. Using Equation 1.40, and assuming the limiting case where $i = 90^{\circ}$, lower limits to β were found for each measured line. Note that β is unlikely to have a fixed value as the size and shape of the Roche lobes of both components will vary as the separation between the components varies as they orbit eccentrically.

Values for the mass of the optical component, M_o, the mass of the neutron star, M_x, and the inclination, i, were obtained from Equations 1.18,1.19, and 1.40-1.41. The results are shown in Table 3.2.

A final value of $K_o = 20.4 \pm 1.8$km s^{-1}, by calculating the mean for the results for the individual lines. For $K_x = 275 \pm 1$km s^{-1} (Deeter et al 1987), this results in a mass ratio, q of 13.5 ± 1.2 from Equation 1.1. Using this value for q, and a value of $33°.8 \pm 1°.3$ for θ_e (Watson & Griffiths 1987), a value for $\beta = 0.865 - 1.000$ was obtained from Equations 1.40-1.44. Now, again using Equations 1.40-1.44, a value of $i = 77^{\circ}_{-12}{}^{+13}$ was obtained.

Thus, from Equation 1.19, a value of $23.6^{+5.5}_{-2.0}$M$_\odot$ for M_o, the mass of the optical companion is obtained. Similarly, from Equation 1.18, a value of $1.77^{+0.55}_{-0.29}$M$_\odot$ is obtained for M_x, the mass of the neutron star.

3.8 Conclusion

Our value for K$_o$ of 20.4 ± 1.8km s^{-1} is comparable to those quoted by other recent authors: van Kerkwijk (1995) gives a value of 20.8 ± 2.7km s^{-1}, and Stickland et al (1997) give a value of 17.8 ± 1.6km s^{-1}. Our result of $1.77^{+0.55}_{-0.29}$M$_\odot$ for the neutron star mass is compatible with van Kerkwijk's 1995 mass value of $M_x = 1.9^{+0.7}_{-0.5}$M$_\odot$, but is somewhat larger than the value of between 1.34M$_\odot$ and 1.53M$_\odot$ determined by Stickland et al (1997).

Our results therefore appear to support the view that the neutron star in Vela X-1 is significantly more massive than the canonical value of 1.4M$_\odot$. However, there are a number of potential sources of systematic error, some of which were discussed in Chapter 2. A number of these will be examined below. As Vela X-1 is an early-type star, it has a significant stellar wind. As we saw in Chapter 2, a strong and variable stellar wind can have disasterous consequences when making radial velocity measurements, especially over an extended period of time. In the case of Vela X-1, however, the supergiant is of later type (B0) than that of Cen X-3 (O6-7), and thus has a weaker wind. Additionally, as the observations were made over a relatively short time period, the potential effect of long-term wind variation will be less than if the observations were spread over a number of years, as in the case of Cen X-3. In other words, although the effect of the supergiant's stellar wind cannot be discounted, its effect should be less than its effect on our Cen X-3 results.

As with Cen X-3, X-ray heating is not expected to be significant. Although the Vela X-1 supergiant has a lower surface temperature than the Cen X-3 supergiant, in the case of Vela X-1, the supergiant and the neutron star are more widely seperated. Van Kerkwijk (1995) quotes a, the semi-major axis of the orbit, as $53.1^{+2.0}_{-1.0}$R$_\odot$, and R$_{opt}$, the radius of the supergiant as $30.3^{+2.0}_{-2.2}$R$_\odot$ for Vela X-1. In the case of Cen X-3, the figures are $a = 18.7^{+1.2}_{-0.7}$R$_\odot$ and R$_{opt} = 11.1^{+1.9}_{-1.2}R_\odot$. Ideally, the possibility of X-ray heating in Vela X-1 would have been pursued further by making plotting equivalent width measurements against

phase, but this is left as a future exercise because of the sheer size of the dataset.

Another source of error Vela X-1 has in common with Cen X-3 is the tidal deformation of the supergiant. In Vela X-1 this problem is much more complex, as there as ample evidence (van Kerkwijk 1993) that the supergiant "wobbles" due to the varying gravitational force exerted by the neutron star. This effect appears to manifest itself as deviations from a pure Keplerian radial velocity curve. These deviations do not seem to last longer than a single night, and it has been suggested that they are the result of short-lived, high-order pulsations of the photosphere. As well as introducing another source of error into our attempts to measure the radial velocity of the centre of mass of the supergiant, the "wobbles" cause another problem. If the shape of the star is constantly changing, this would affect the extent to which the star fills its Roche lobe. Additionally, the size and shape of the Roche lobe itself will vary with phase, as the two components orbit each other in eccentric orbits.

Although the optical component in Vela X-1 is of later type than that in Cen X-3, and so has a weaker stellar wind, other effects may introduce a significant systematic error. In particular, the velocity deviations observed by van Kerkwijk(1993) could easily have biased our results as they only span just over a single orbit. In addition, if the optical component is moving in a "wobbly" fashion as van Kerkwijk suggests, this would have a complex effect on the shape of its Roche lobe, which could invalidate the approximation used to model it (see Equations 1.40-1.44).

Other sources of error are not intrinsic to the system itself, but are due to the manner in which it was observed. There was not a very clear objective when the observations were being made, and so it was decided to observe as large a wavelength region as possible. This meant fitting as many orders as possible onto the CCD. This in turn meant there was very little space between the orders, and often little or no sky background to subtract from the stellar spectra. Mt Stromlo is relatively badly affected by light pollution, and there is no real way of gauging the effect of this on the signal-to-noise ratio of our spectra.

However, can our results for the mass of the neutron star be used to draw any inferences about it ? Salgado et al (1994) detail a number of different equations of state for neutron star matter. Two of these models have maximum masses comparable to our result. These are the PandN model, where the neutron star is composed of pure neutron matter whose interaction is described by the Reid soft core potential (Pandharipande 1971), and the Glend2 model, where the neutron star is composed of nucleons, hyperons, and Δ-particles whose interaction is described by an effective Lagrangian (Glenndenning 1985). The maximum mass of the PandN model is between 1.66 and 1.93 $M_{\odot}$, depending on the rotational velocity, while the maximum mass of the Glend2 model varies from 1.78 to 2.09 $M_{\odot}$, again depending on the

rotational velocity.

Our neutron star mass results do not appear to be able to rule out either of these models.

Appendix - Cross-correlation results for all datasets.

Table 3.3 Cross-correlation results for all datasets. Uncertainties quoted are the raw uncertainties returned from the cross correlation, and have not been rescaled to force the reduced χ^2 of the fit to unity.

Date	JD	Radial velocities (km s^{-1})			
		H_γ	H_β	HeI (4026Å)	HeI (4471Å)
11 Feb 1996	10124.98	21.1± 2.3	34.2± 5.4	19.5± 5.6	21.1± 2.3
11 Feb 1996	10125.00	22.7± 2.5	39.2± 6.6	22.9± 5.5	23.9± 5.1
11 Feb 1996	10125.05	26.3± 3.4	40.7± 7.7	26.5± 1.5	23.7± 4.1
11 Feb 1996	10125.06	28.7± 3.6	43.0± 6.5	25.5± 6.2	24.5± 4.4
11 Feb 1996	10125.14	30.3± 3.1	35.4± 3.2	12.7± 4.3	27.7± 7.9
11 Feb 1996	10125.15	29.4± 2.1	39.9± 7.1	22.50± 3.6	26.3± 2.9
11 Feb 1996	10125.16	27.7± 2.6	38.6± 13.4	–	24.6± 1.5
12 Feb 1996	10125.92	14.7± 4.9	11.1± 14.0	14.2± 9.6	16.5± 4.0
12 Feb 1996	10125.93	12.6± 4.4	34.8± 17.2	17.4± 5.1	16.3± 2.9
12 Feb 1996	10125.94	15.8± 4.7	–	18.4± 4.2	17.0± 3.0
12 Feb 1996	10126.03	17.2± 5.5	–	16.0± 3.8	18.2± 3.0
12 Feb 1996	10126.04	17.3± 5.8	–	17.2± 8.6	19.5± 3.0
12 Feb 1996	10126.06	16.9± 5.4	26.9± 7.3	17.4± 4.5	19.7± 5.6
12 Feb 1996	10126.12	21.2± 5.2	30.6± 9.2	11.5± 16.5	24.9± 9.6
12 Feb 1996	10126.13	24.3± 5.0	–	17.1± 6.1	18.5± 8.5
12 Feb 1996	10126.14	21.8± 6.4	32.2± 8.7	9.2± 12.2	22.0± 6.7
12 Feb 1996	10126.18	21.1± 5.5	33.0± 11.6	8.7± 5.0	22.7± 7.3
12 Feb 1996	10126.19	23.2± 4.8	31.7± 9.1	11.5± 9.6	23.3± 8.5
12 Feb 1996	10126.20	18.6± 4.8	31.3± 8.9	8.5± 18.4	21.3± 10.1
13 Feb 1996	10126.94	19.1± 4.6	30.6± 9.9	9.7± 4.6	20.2± 3.3
13 Feb 1996	10126.95	14.9± 6.4	44.7± 30.1	2.8± 4.8	16.9± 3.9
13 Feb 1996	10126.96	18.8± 6.1	22.4± 12.3	15.4± 11.5	17.2± 4.3
13 Feb 1996	10127.02	13.2± 8.5	31.3± 9.6	9.6± 6.6	14.4± 5.3
13 Feb 1996	10127.03	15.6± 5.3	29.7± 10.6	8.7± 3.6	15.2± 4.7
13 Feb 1996	10127.04	17.0± 7.0	–	11.6± 1.5	11.9± 8.4
13 Feb 1996	10127.09	11.9± 4.6	–	2.2± 1.6	21.2± 7.4
13 Feb 1996	10127.10	10.1± 10.9	24.4± 11.3	7.7± 6.2	16.9± 18.5
13 Feb 1996	10127.12	14.1± 6.9	25.1± 7.8	3.6± 4.2	16.5± 13.6
13 Feb 1996	10127.14	15.2± 4.3	27.9± 9.4	6.1± 5.1	16.6± 9.5
13 Feb 1996	10127.16	14.5± 3.8	28.1± 12.5	17.5± 15.1	17.3± 4.2
13 Feb 1996	10127.17	13.7± 6.2	–	9.8± 1.9	14.1± 5.7
13 Feb 1996	10127.20	11.8± 3.3	–	7.7± 4.3	15.3± 8.3
13 Feb 1996	10127.22	10.6± 5.5	–	6.6± 3.3	14.6± 8.1
14 Feb 1996	10127.92	−16.4± 8.9	−11.5± 2.5	−9.4± 10.4	−10.7± 5.6
14 Feb 1996	10127.93	−14.1± 10.0	−7.7± 2.9	−7.9± 4.7	−9.9± 5.9
14 Feb 1996	10127.95	−16.7± 11.3	−12.7± 3.5	−3.8± 4.2	−8.3± 8.8
14 Feb 1996	10128.05	−18.6± 8.1	−24.4± 6.1	−9.6± 13.5	−9.1± 15.2
14 Feb 1996	10128.06	−22.3± 15.0	−12.5± 4.9	−4.3± 10.1	−9.5± 23.7
14 Feb 1996	10128.08	−24.0± 13.8	−10.0± 3.0	−6.6± 7.1	−3.7± 29.6
14 Feb 1996	10128.14	−19.3± 8.2	−19.7± 4.6	−15.6± 6.0	−10.4± 9.5
14 Feb 1996	10128.15	−17.9± 7.8	−15.7± 7.5	−11.0± 7.1	−10.5± 8.0
14 Feb 1996	10128.17	−17.4± 10.2	−24.7± 6.7	−12.4± 7.6	−13.3± 5.9
14 Feb 1996	10128.18	−19.7± 11.4	−23.2± 5.3	−15.0± 10.5	−12.3± 6.1
14 Feb 1996	10128.20	−22.4± 8.6	−20.0± 6.3	−9.0± 4.7	−12.1± 9.3
14 Feb 1996	10128.21	−19.9± 10.0	−26.0± 6.4	−4.9± 3.3	−12.3± 5.1
14 Feb 1996	10128.22	−20.5± 11.3	−17.9± 4.2	−8.9± 4.1	−13.1± 5.9

Table 3.4 Cross-correlation results for all datasets. Uncertainties quoted are the raw uncertainties returned from the cross correlation, and have not been rescaled to force the reduced χ^2 of the fit to unity.

Date	JD	Radial velocities (km s^{-1})			
		H_γ	H_β	HeI (4026Å)	HeI (4471Å)
15 Feb 1996	10128.92	−30.3± 5.3	−33.4± 10.2	−22.2± 21.3	−16.0± 8.8
15 Feb 1996	10128.93	−30.3± 2.6	−33.4± 10.0	−21.9± 4.4	−15.8± 4.5
15 Feb 1996	10128.95	−27.9± 3.2	−34.4± 8.8	−18.0± 1.8	−21.1± 5.9
15 Feb 1996	10128.96	−27.9± 6.9	−34.4± 7.8	−17.8± 8.9	−21.1± 2.3
15 Feb 1996	10129.01	−28.7± 3.8	−32.1± 9.6	−12.0± 4.7	−21.4± 4.7
15 Feb 1996	10129.02	−23.4± 3.1	−36.1± 6.3	−19.8± 3.3	−19.6± 2.6
15 Feb 1996	10129.03	−23.4± 1.3	−36.1± 5.6	−20.1± 7.7	−19.5± 5.6
15 Feb 1996	10129.12	−21.8± 5.4	−29.9± 6.7	−12.6± 3.3	−17.5± 0.9
15 Feb 1996	10129.13	−21.7± 4.5	−24.8± 7.6	−7.2± 5.8	−18.0± 2.7
15 Feb 1996	10129.18	−16.2± 5.0	−19.2± 6.3	−11.5± 5.2	−13.9± 13.7
15 Feb 1996	10129.19	−22.3± 2.9	−22.9± 8.7	−7.8± 1.8	−17.5± 3.1
15 Feb 1996	10129.20	−16.9± 5.6	−30.8± 11.1	−12.8± 5.4	−17.5± 3.8
15 Feb 1996	10129.22	−20.9± 2.1	−20.7± 5.1	−12.4± 3.6	−14.1± 9.0
15 Feb 1996	10129.23	−21.1± 2.9	−20.4± 7.2	−15.7± 3.4	−20.1± 2.8
16 Feb 1996	10129.99	−18.4± 4.2	−11.2± 5.2	−14.4± 3.0	−19.6± 6.1
16 Feb 1996	10130.01	−15.9± 6.0	−12.8± 7.7	−14.0± 2.9	−17.5± 1.8
16 Feb 1996	10130.02	−17.3± 6.0	−11.0± 8.4	−14.2± 2.7	−16.2± 2.3
16 Feb 1996	10130.03	−17.3± 4.4	−10.9± 7.5	−14.1± 13.0	−16.0± 1.8
16 Feb 1996	10130.06	−16.7± 7.2	−7.8± 5.4	−11.0± 10.3	−8.7± 25.5
16 Feb 1996	10130.07	−12.4± 4.6	−10.6± 12.6	−7.3± 7.0	−5.7± 24.7
16 Feb 1996	10130.11	−13.8± 3.9	−13.5± 5.1	−10.6± 11.4	−13.7± 2.1
16 Feb 1996	10130.13	−14.2± 4.4	−11.4± 3.1	−13.7± 10.2	−8.5± 7.1
16 Feb 1996	10130.14	−14.4± 2.4	−11.2± 3.4	−14.0± 8.2	−10.4± 7.5
16 Feb 1996	10130.18	−10.6± 1.5	−9.4± 5.3	−13.6± 4.1	−12.0± 1.7
16 Feb 1996	10130.19	−13.9± 5.2	−9.2± 3.0	−12.6± 10.8	−11.2± 11.8
16 Feb 1996	10130.21	−14.8± 1.6	−6.8± 2.4	−13.6± 2.8	−10.6± 3.9
18 Feb 1996	10131.91	−4.3± 3.3	−10.0± 9.0	−9.3± 2.4	−5.6± 6.1
18 Feb 1996	10131.92	−3.8± 1.3	−13.6± 20.7	−3.7± 1.3	−9.2± 3.4
18 Feb 1996	10131.93	−1.3± 3.0	−11.2± 10.5	−0.2± 2.8	−6.0± 6.4
18 Feb 1996	10131.98	−2.5± 3.6	3.7± 6.9	−1.4± 6.8	0.8± 11.8
18 Feb 1996	10131.99	−1.1± 1.4	−2.7± 9.0	−3.5± 7.8	−4.9± 1.0
18 Feb 1996	10132.00	−1.6± 1.2	0.7± 14.4	0.0± 0.5	−3.9± 3.6
18 Feb 1996	10132.03	−0.9± 2.6	−4.7± 16.0	−1.2± 3.9	0.1± 1.5
18 Feb 1996	10132.04	−1.7± 3.9	−3.8± 3.9	0.1± 5.5	0.5± 3.9
18 Feb 1996	10132.05	1.9± 1.5	1.0± 7.6	−2.9± 3.5	3.4± 9.7
18 Feb 1996	10132.07	2.7± 1.1	0.9± 6.7	−2.6± 1.6	2.1± 2.6
18 Feb 1996	10132.08	3.1± 0.8	3.6± 4.4	0.8± 4.3	3.5± 7.2
18 Feb 1996	10132.09	4.3± 2.2	−1.1± 4.9	−1.0± 2.7	0.2± 5.6
18 Feb 1996	10132.13	1.2± 2.7	10.3± 5.8	−0.7± 5.5	−0.8± 11.0
18 Feb 1996	10132.15	6.6± 3.1	3.7± 4.2	3.2± 3.8	−1.3± 10.4
18 Feb 1996	10132.17	1.5± 7.5	4.1± 3.0	−2.9± 4.1	−2.0± 10.4
18 Feb 1996	10132.21	6.2± 4.8	8.9± 20.3	2.0± 7.1	−2.2± 20.8
18 Feb 1996	10132.22	2.2± 6.8	4.2± 2.1	0.3± 1.2	−0.3± 12.4
18 Feb 1996	10132.23	1.6± 5.0	3.3± 4.4	2.2± 7.6	−0.4± 12.1
19 Feb 1996	10132.91	−1.7± 2.7	5.0± 4.1	0.9± 8.4	−1.9± 8.1
19 Feb 1996	10132.92	3.3± 2.3	4.9± 3.0	−0.0± 8.9	0.2± 1.8
19 Feb 1996	10132.94	−0.4± 5.7	8.2± 4.6	−2.8± 2.2	0.5± 3.5
19 Feb 1996	10133.02	0.1± 6.5	3.1± 4.2	−0.4± 2.7	−3.1± 13.9
19 Feb 1996	10133.04	1.6± 1.0	6.7± 3.6	2.2± 5.9	5.0± 11.9
19 Feb 1996	10133.05	3.3± 2.2	5.3± 4.0	1.3± 2.4	3.7± 7.0

Table 3.5 Cross-correlation results for all datasets. Uncertainties quoted are the raw uncertainties returned from the cross correlation, and have not been rescaled to force the reduced χ^2 of the fit to unity.

Date	JD	Radial velocities (km s^{-1})			
		H_γ	H_β	HeI (4026Å)	HeI (4471Å)
20/2/96	10133.90	13.9±2.8	17.7±15.9	12.2±4.2	16.2±6.8
20/2/96	10133.91	12.9±1.1	15.2±7.0	14.8±2.0	19.4±4.3
20/2/96	10133.92	18.6±1.5	36.5±18.8	11.5±2.5	19.5±1.1
20/2/96	10133.97	18.8±0.8	–	–	17.7±2.6
20/2/96	10133.98	15.8±5.9	–	14.7±3.6	20.4±3.9
20/2/96	10134.00	16.5±3.5	–	15.0±2.6	23.7±8.7
21/2/96	10134.90	26.9±2.7	36.7±7.4	27.2±5.8	25.6±4.2
21/2/96	10134.92	31.9±3.8	37.8±11.6	13.6±5.1	28.8±5.3
21/2/96	10134.93	26.0±4.4	36.4±9.8	24.1±1.6	30.1±7.7
21/2/96	10134.98	24.4±7.3	38.2±2.1	32.1±6.6	32.3±2.7
21/2/96	10134.99	32.5±3.2	40.2±6.8	30.5±13.8	29.7±3.2
21/2/96	10135.01	25.5±8.3	40.1±6.2	27.2±6.9	30.3±5.7
21/2/96	10135.05	29.9±2.8	33.8±4.8	8.1±5.1	32.1±9.6

3.9 Appendix - Eccentric Orbit Fitting Code.

```
PROGRAM ECC_ORBIT
C
C     Intended to calculate observed radial velocities for
C     an eccentric binary system
C
C     Variables:
C     PERIOD = orbital period of system (in days)
C     E = eccentricity of system
C     OMEGA = angle of semi-major axis to the line of sight (radians)
C     T_ZERO = Start time of emphersis (JD)
C     ECC_ANAL = Eccentric anomaly
C     TIME = current time (JD)
C     PI - pi (!)
C     TRUE_ANOM = true anomaly
C     A1 = ABS MAX OF RADIAL VELOCITY (km per second)
C     B1 = ABS MIN OF RADIAL VELOCITY (km per second)
C     ASINI = Assumed projected semi-major axis (km)
C     GAMMA = Assumed bias velocity
C     V = Calculated radial velocity
```

```
C     STEPS = No of points calculated for each orbit
C     NPTS = No of actual data points
C     OFFSET = phase correction factor
C     SEMI_AMP= Semi-amplitude of radial velocity curve

PARAMETER (NMAX=1000)

      DOUBLE PRECISION PERIOD_DAYS, E, OMEGA,PI
      DOUBLE PRECISION ECC_ANAL_OLD,ECC_ANAL_NEW
DOUBLE PRECISION TIME,T_ZERO
DOUBLE PRECISION PERIOD_SECS

DOUBLE PRECISION TRUE_ANOM

DOUBLE PRECISION A1,B1,ASINI,GAMMA,V(NMAX)
DOUBLE PRECISION V_BSF(NMAX)

DOUBLE PRECISION XP(NMAX),YP(NMAX),YPVAR(NMAX)
DOUBLE PRECISION DUMMY(NMAX),CHISQ
DOUBLE PRECISION CURVE(NMAX)
DOUBLE PRECISION STEP

REAL OFFSET,CORRECTION_GRAD

REAL OFFSET_MIN,OFFSET_MAX,OFFSET_STEP,OFFSET_BSF
DOUBLE PRECISION ASINI_MIN, ASINI_MAX, ASINI_STEP
DOUBLE PRECISION GAMMA_MIN, GAMMA_MAX, GAMMA_STEP
DOUBLE PRECISION ASINI_BSF, GAMMA_BSF
DOUBLE PRECISION SEMI_AMP,SEMI_AMP_BSF
DOUBLE PRECISION CHISQR_BSF

      INTEGER COUNTER,I,J,NPTS

      PERIOD_DAYS=8.964416
PERIOD_SECS=PERIOD_DAYS*86400
```

```
        E=0.0885
        OMEGA=2.6284
        T_ZERO=2444279.0466
        ECC_ANAL_OLD=0.5
CORRECTION_GRAD=0.47

ASINI_MIN=2000000
ASINI_MAX=3000000
ASINI=ASINI_MIN

GAMMA_MIN=-8
GAMMA_MAX=2
GAMMA=0.0

OFFSET_MIN=-0.25
OFFSET_MAX=0.25
OFFSET=OFFSET_MIN

C       Open file for reading out data

OPEN(UNIT=5,FILE='CURVE',STATUS='NEW')

C Creates data for fitted curve and writes to file

WRITE(*,*)'Creating data for fitted curve'

STEP=(2450135.054-2450124.977)/NMAX

DO I=1,NMAX

   CURVE(I)=ECC_ORBIT_VEL(PERIOD_DAYS,
     &       PERIOD_SECS,2450124.977+I*STEP,T_ZERO,
     &       E,ASINI,OMEGA,GAMMA,OFFSET,SEMI_AMP)
```

```
   WRITE(5,*) (2450124.977+I*STEP)-T_ZERO,CURVE(I)

ENDDO

        END

DOUBLE PRECISION FUNCTION ECC_ORBIT_VEL
     &     (PERIOD_DAYS,PERIOD_SECS,
     &    XP,T_ZERO,E,ASINI,OMEGA,GAMMA,OFFSET,SEMI_AMP)

DOUBLE PRECISION PERIOD_DAYS,XP,T_ZERO
DOUBLE PRECISION PERIOD_SECS
DOUBLE PRECISION E,ASINI,OMEGA,GAMMA,SEMI_AMP
DOUBLE PRECISION ECC_ANAL_OLD,PI,ECC_ANAL_NEW
        DOUBLE PRECISION TRUE_ANOM,A1,B1
INTEGER COUNTER
REAL OFFSET

PI=3.1415927
ECC_ANAL_OLD=2.0

C       Finds the eccentric anomaly via Newton's method

DO 100,COUNTER=1,10

           ECC_ANAL_NEW = ECC_ANAL_OLD - (ECC_ANAL_OLD -
     &     E*SIN(ECC_ANAL_OLD) -
     &      (2.0*PI/PERIOD_DAYS)*
     &      (XP-T_ZERO+OFFSET*PERIOD_DAYS))/
     &      (1.0-E*COS(ECC_ANAL_OLD))

   IF (ECC_ANAL_OLD.EQ.ECC_ANAL_NEW) GOTO 200

           ECC_ANAL_OLD=ECC_ANAL_NEW
```

```
 100 CONTINUE

C Calculates the true anomaly

 200 TRUE_ANOM = 2* ATAN (((1+E)/(1-E))**0.5*TAN(ECC_ANAL_NEW/2.0))

C Calculates A and B

A1 = ((2*PI*ASINI)/(PERIOD_SECS
     &     *(1-E**2)**0.5))*(1+E*COS(OMEGA))
B1 = ((2*PI*ASINI)/(PERIOD_SECS
     &     *(1-E**2)**0.5))*(1-E*COS(OMEGA))

C       Calculates semi-amplitude of radial velocity curve

SEMI_AMP=(A1+B1)/2.0

C       Calculate V

ECC_ORBIT_VEL = GAMMA + (A1-B1+ (A1+B1)*COS
     &    (TRUE_ANOM+OMEGA))/2.0
END
```

Appendix - Individidual spectra for lines used in radial velocity analysis .

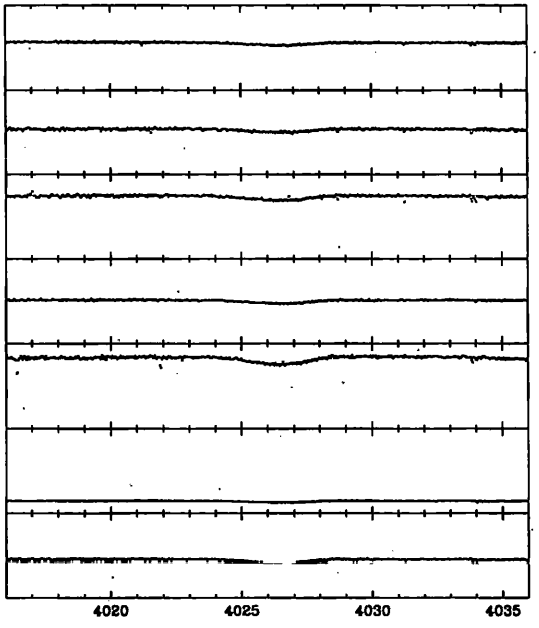

Figure 3.14 Spectra for HeI(4026Å) 11th Feb 1996.

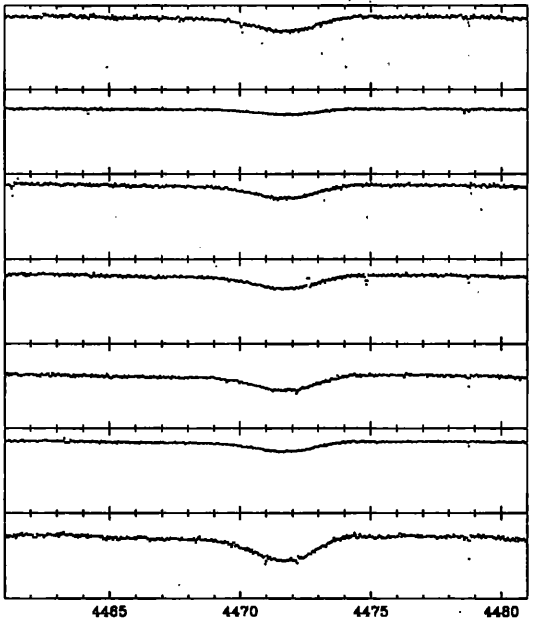

Figure 3.15 Spectra for HeI(4471Å) 11th Feb 1996.

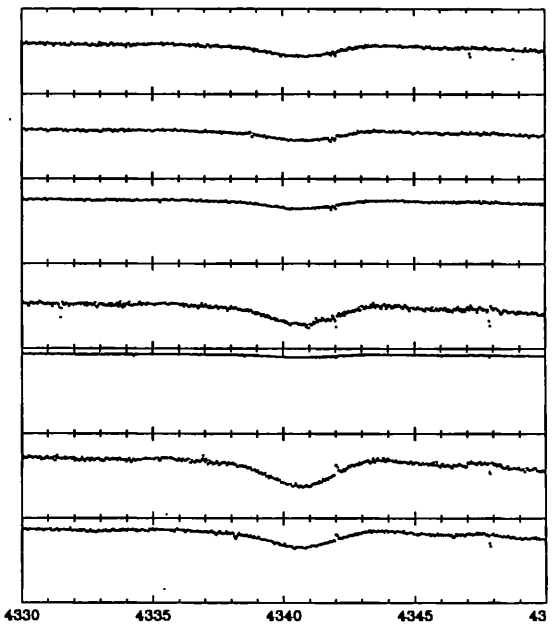

Figure 3.16 Spectra for Hγ(4340Å) 11th Feb 1996.

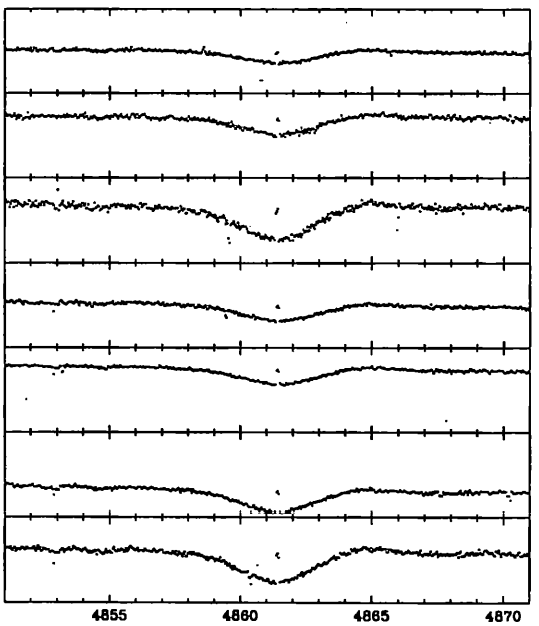

Figure 3.17 Spectra for Hβ(4861Å) 11th Feb 1996.

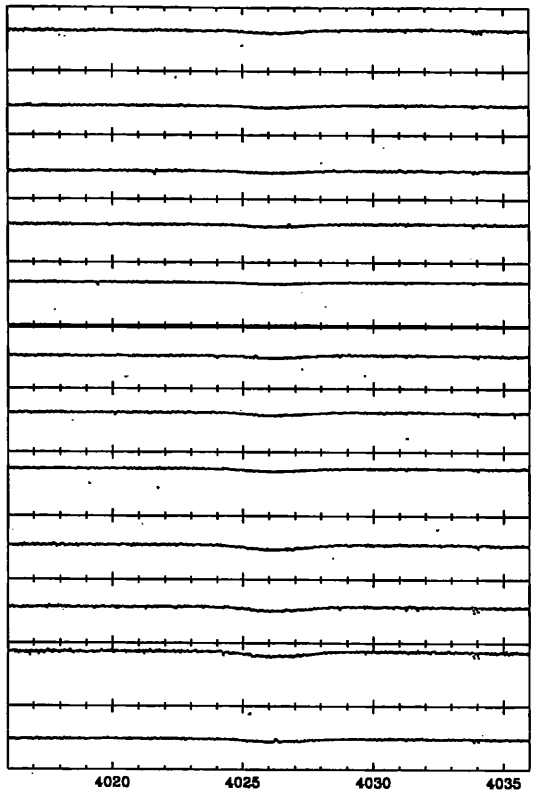

Figure 3.18 Spectra for HeI(4026Å) 12th Feb 1996.

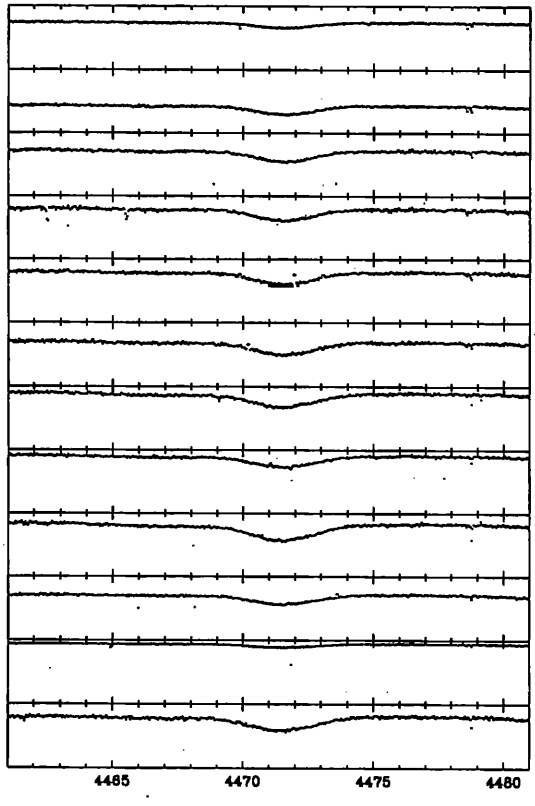

Figure 3.19 Spectra for HeI(4471Å) 12th Feb 1996.

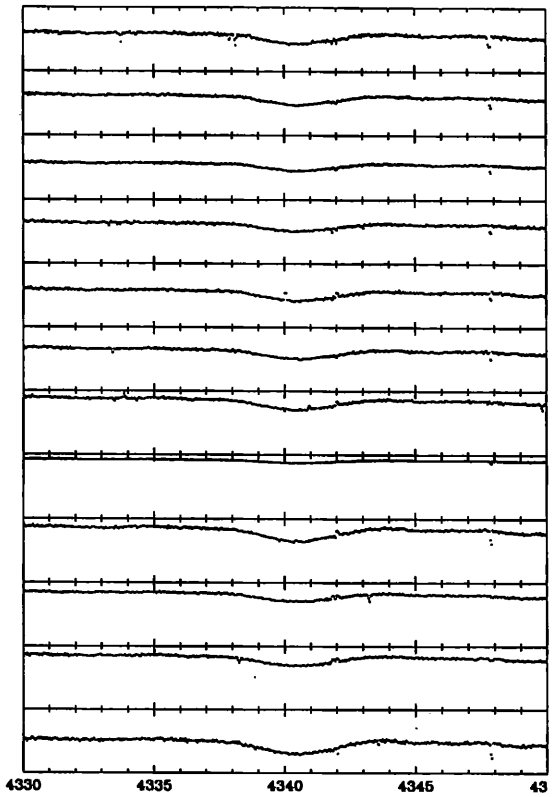

Figure 3.20 Spectra for Hγ(4340Å) 12th Feb 1996.

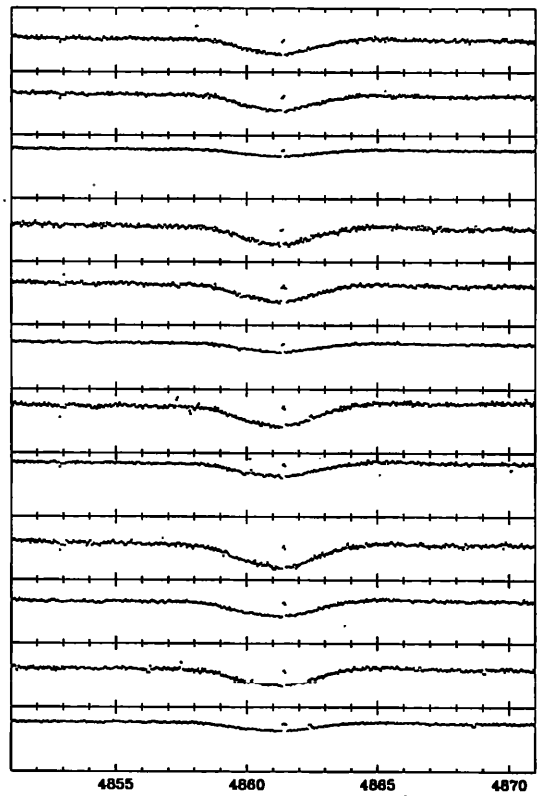

Figure 3.21 Spectra for Hβ(4861Å) 12th Feb 1996.

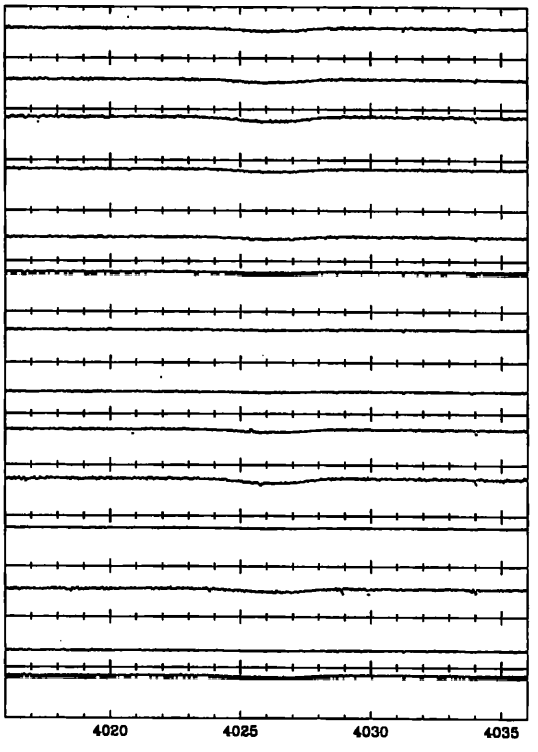

Figure 3.22 Spectra for HeI(4026Å) 13th Feb 1996.

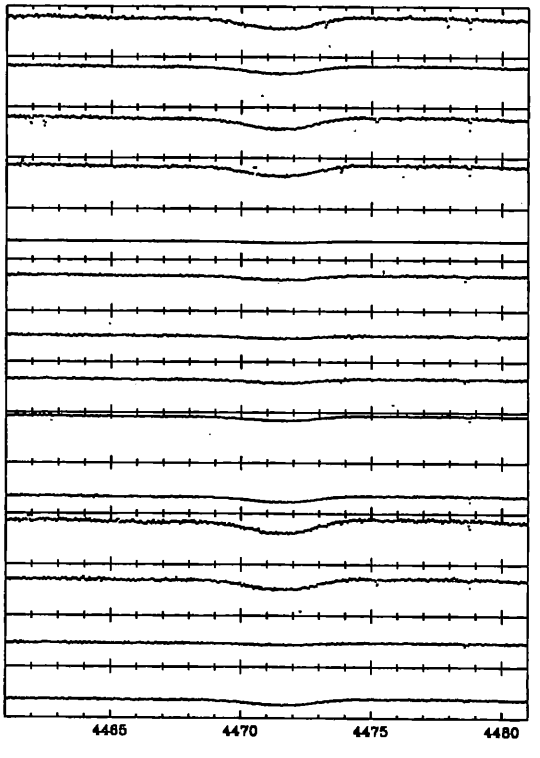

Figure 3.23 Spectra for HeI(4471Å) 13th Feb 1996.

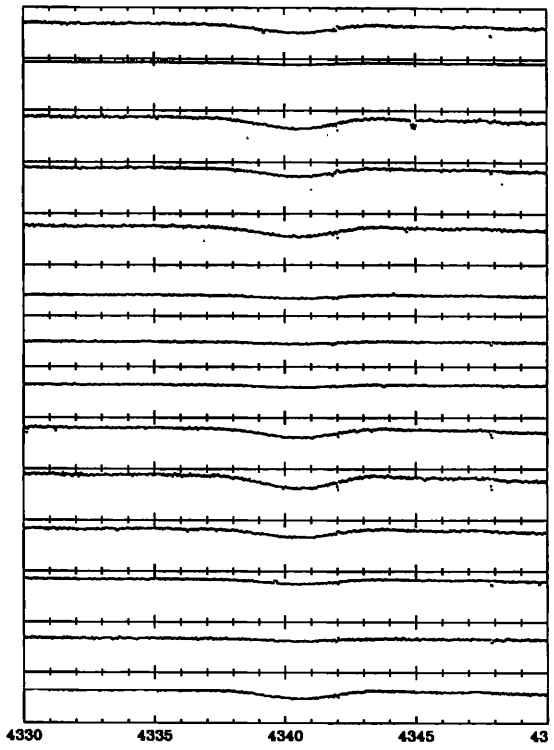

Figure 3.24 Spectra for Hγ(4340Å) 13th Feb 1996.

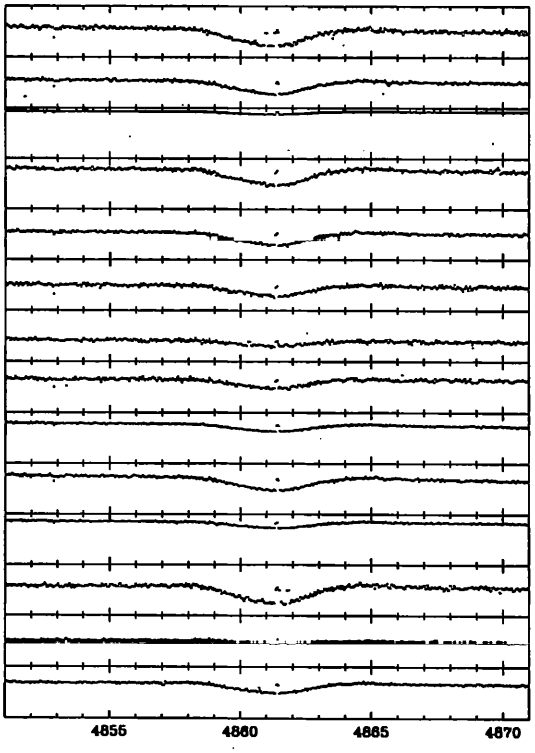

Figure 3.25 Spectra for Hβ(4861Å) 13th Feb 1996.

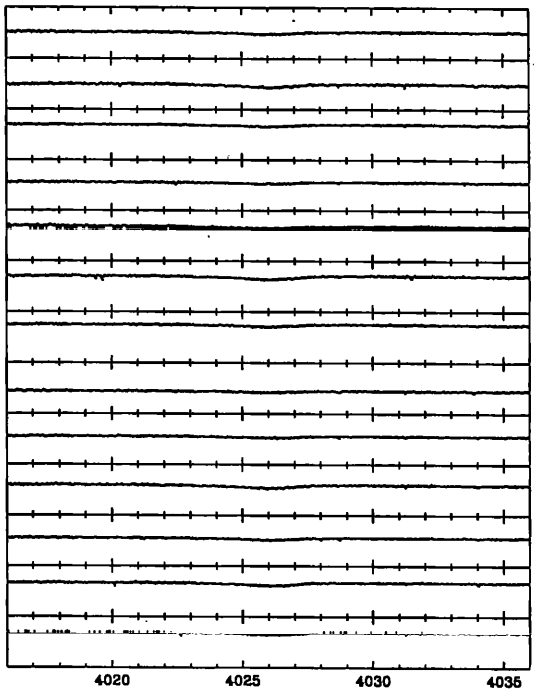

Figure 3.26 Spectra for HeI(4026Å) 14th Feb 1996.

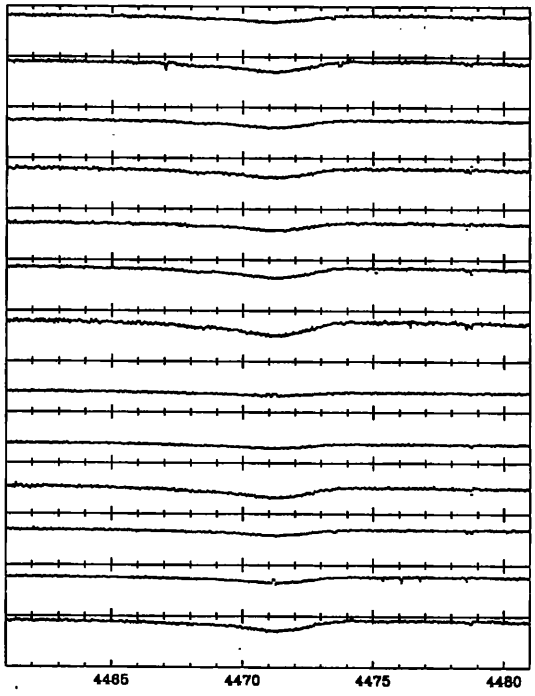

Figure 3.27 Spectra for HeI(4471Å) 14th Feb 1996.

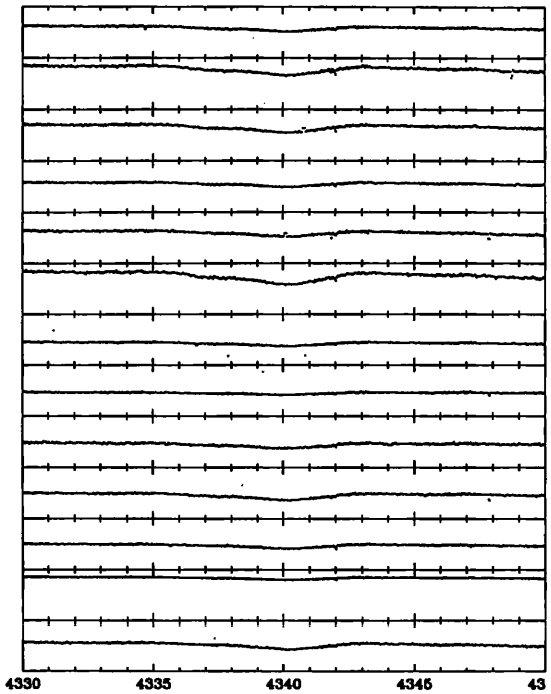

Figure 3.28 Spectra for Hγ(4340Å) 14th Feb 1996.

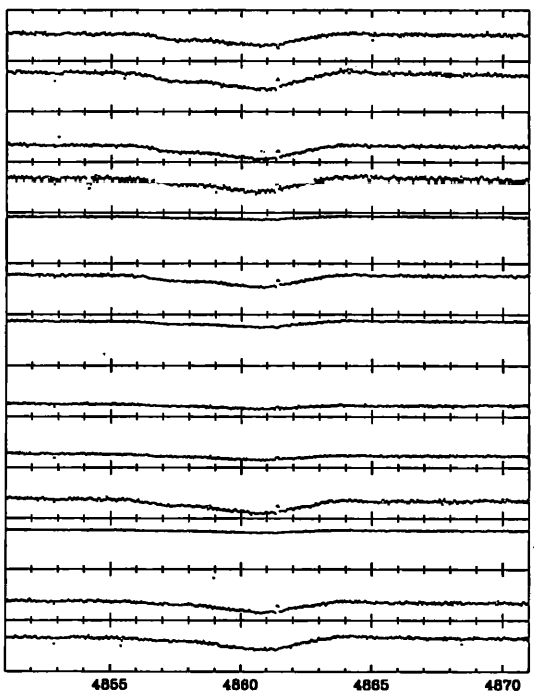

Figure 3.29 Spectra for Hβ(4861Å) 14th Feb 1996.

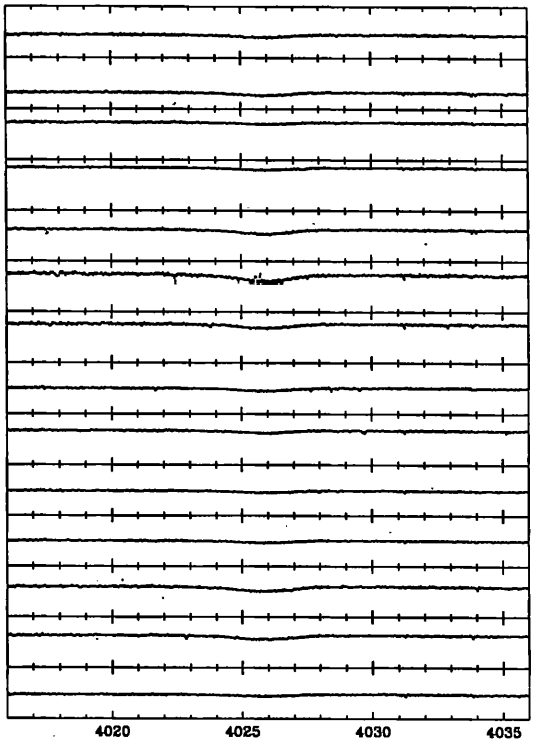

Figure 3.30 Spectra for HeI(4026Å) 15th Feb 1996.

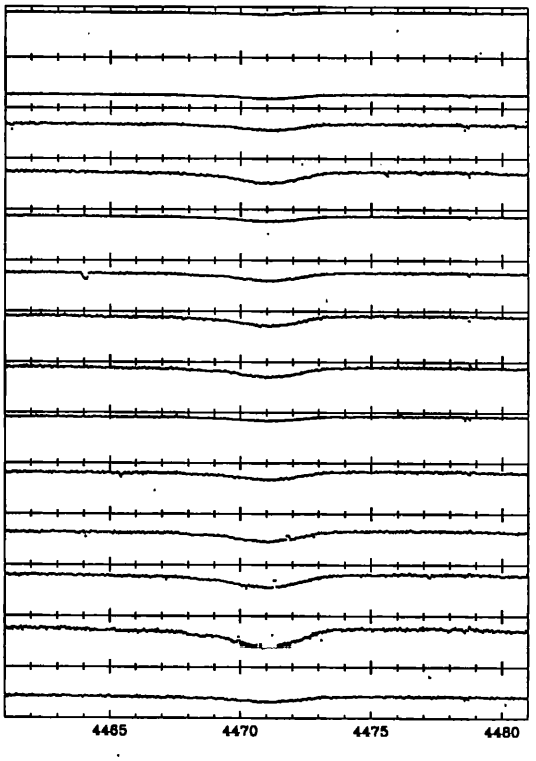

Figure 3.31 Spectra for HeI(4471Å) 15th Feb 1996.

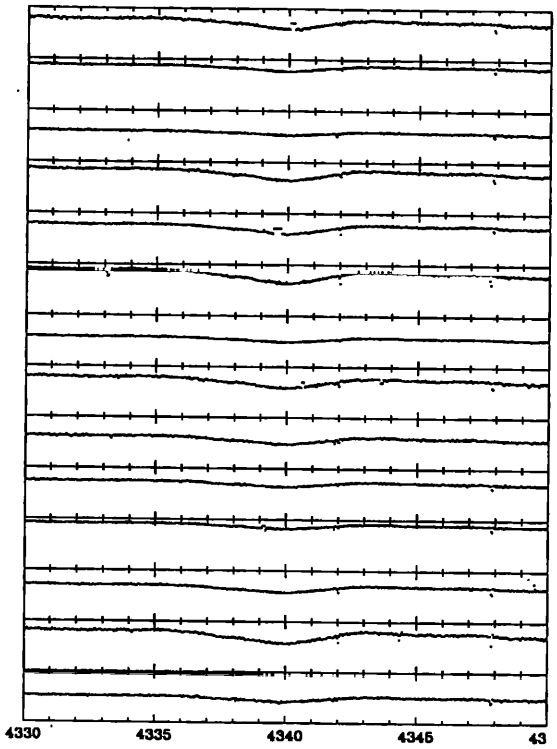

Figure 3.32 Spectra for Hγ(4340Å) 15th Feb 1996.

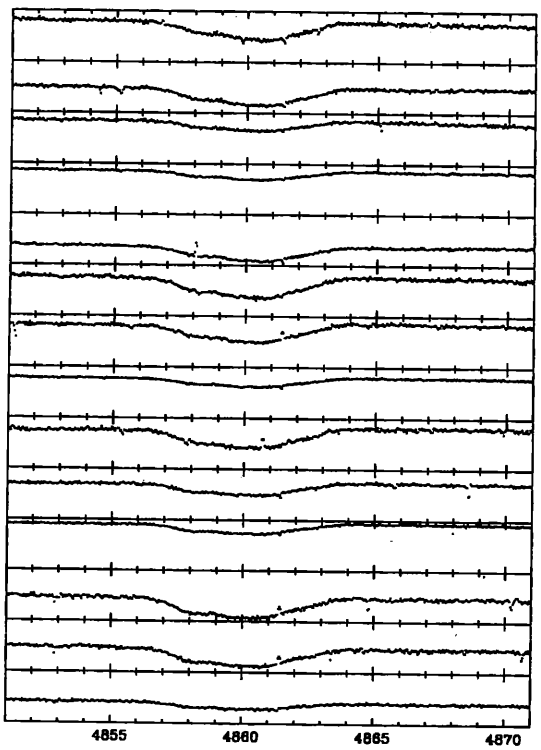

Figure 3.33 Spectra for Hβ(4861Å) 15th Feb 1996.

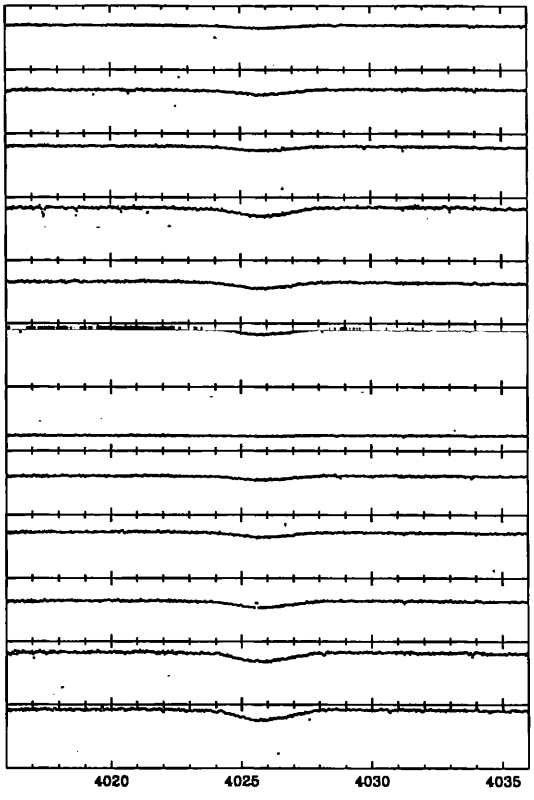

Figure 3.34 Spectra for HeI(4026Å) 16th Feb 1996.

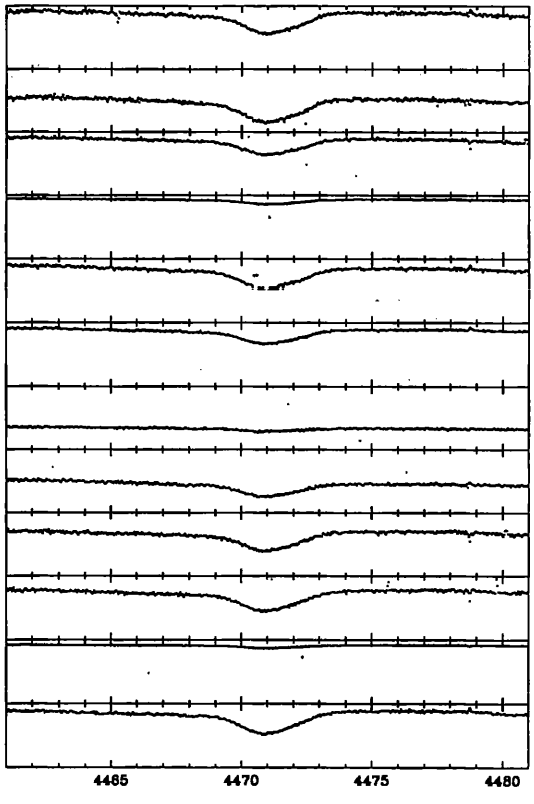

Figure 3.35 Spectra for HeI(4471Å) 16th Feb 1996.

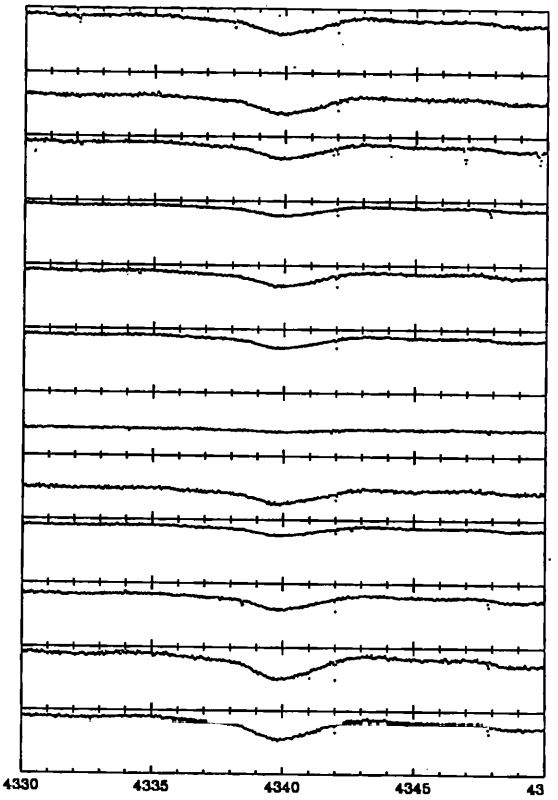

Figure 3.36 Spectra for Hγ(4340Å) 16th Feb 1996.

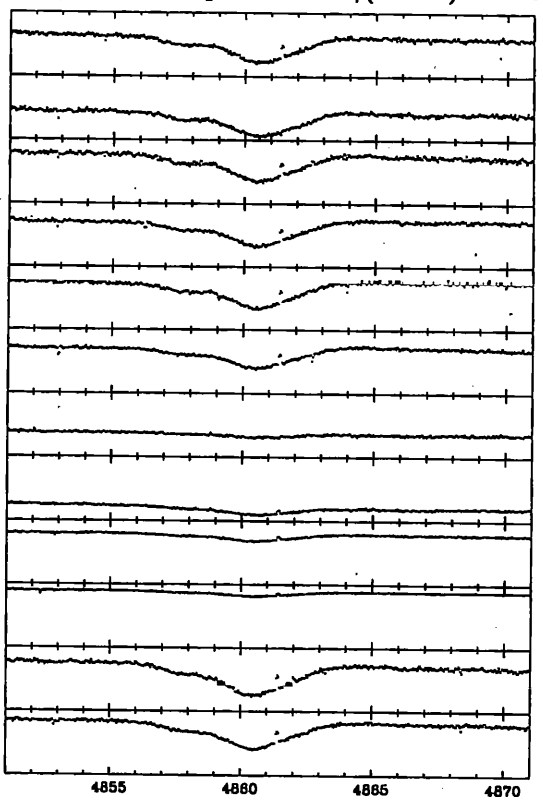

Figure 3.37 Spectra for Hβ(4861Å) 16th Feb 1996.

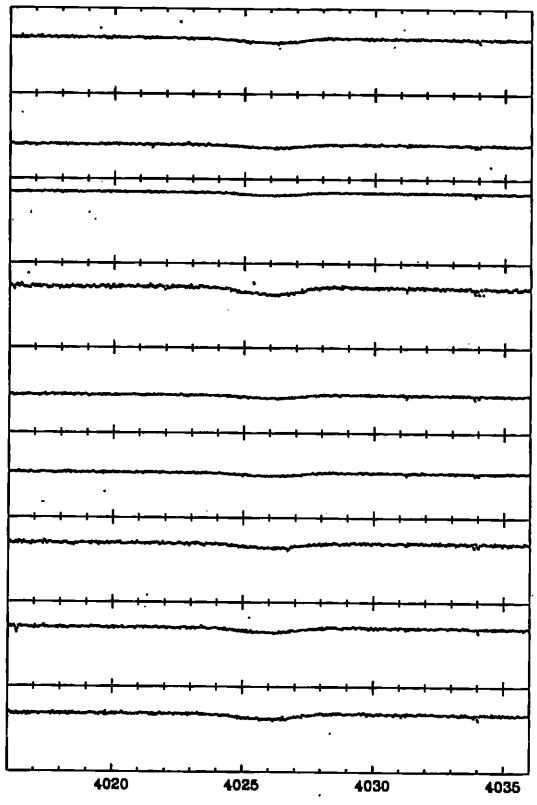

Figure 3.38 Spectra for HeI(4026Å) first half 18th Feb 1996.

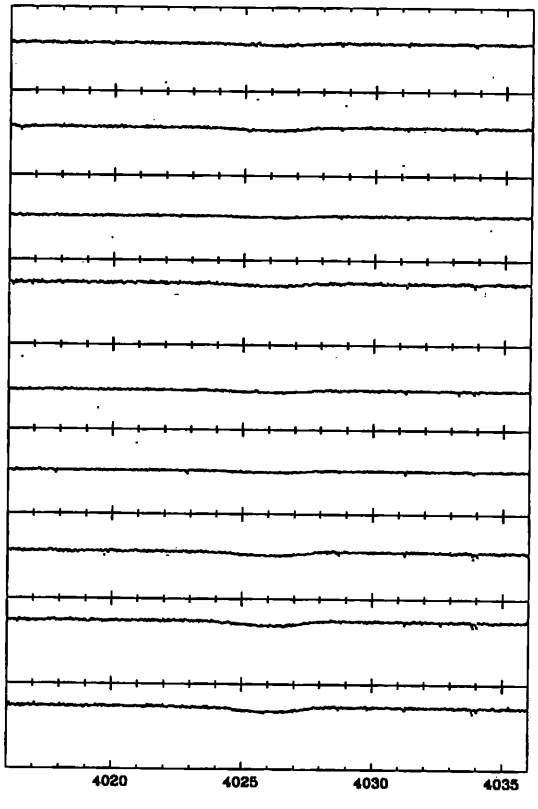

Figure 3.39 Spectra for HeI(4026Å) second half 18th Feb 1996.

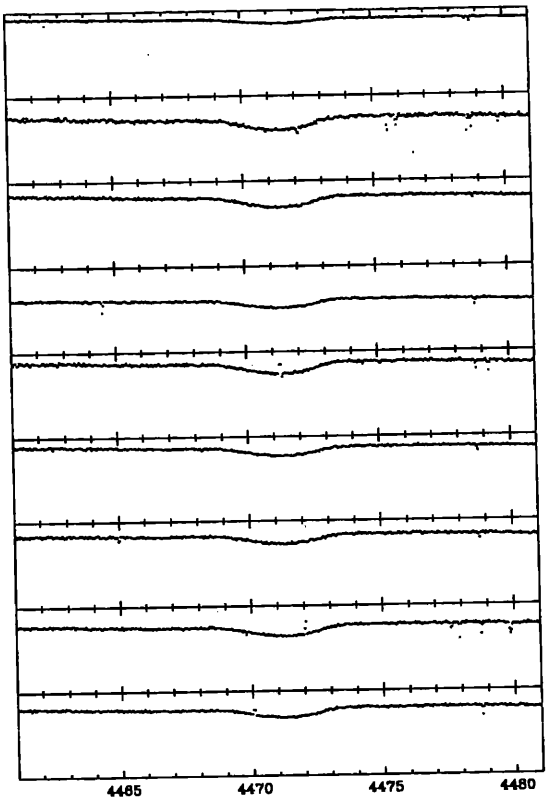

Figure 3.40 Spectra for HeI(4471Å) first half 18th Feb 1996.

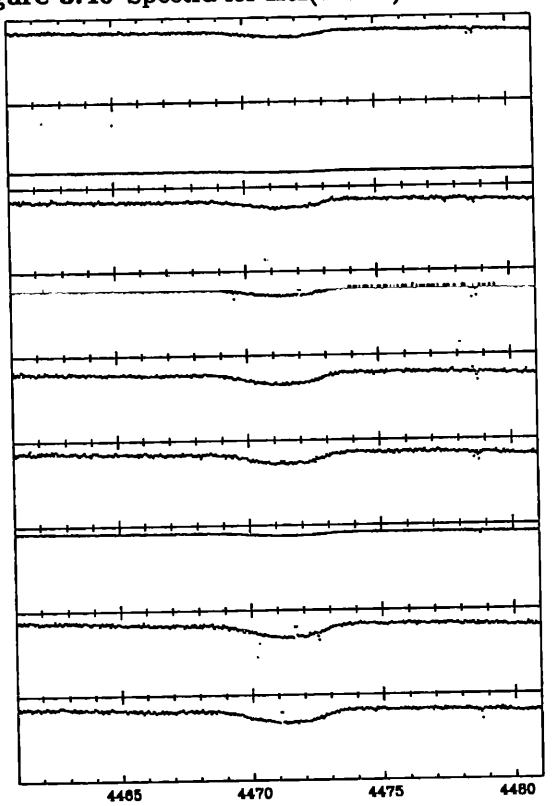

Figure 3.41 Spectra for HeI(4471Å) second half 18th Feb 1996.

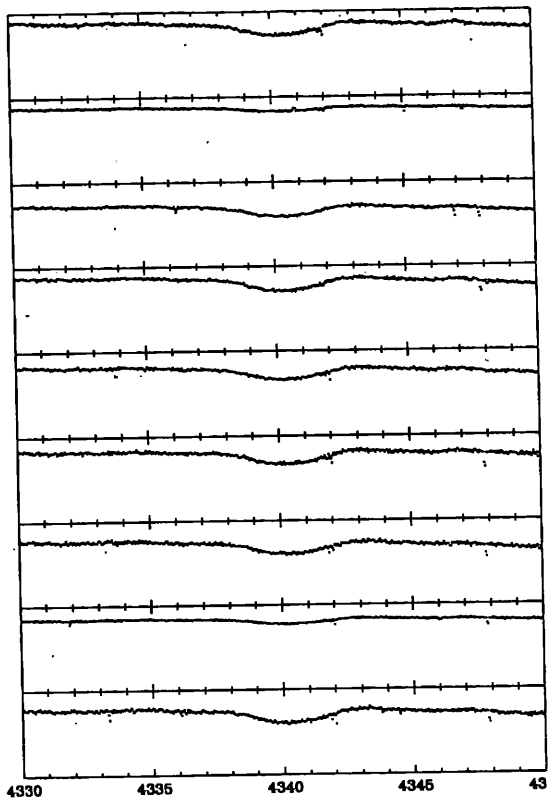

Figure 3.42 Spectra for Hγ(4340Å) first half 18th Feb 1996.

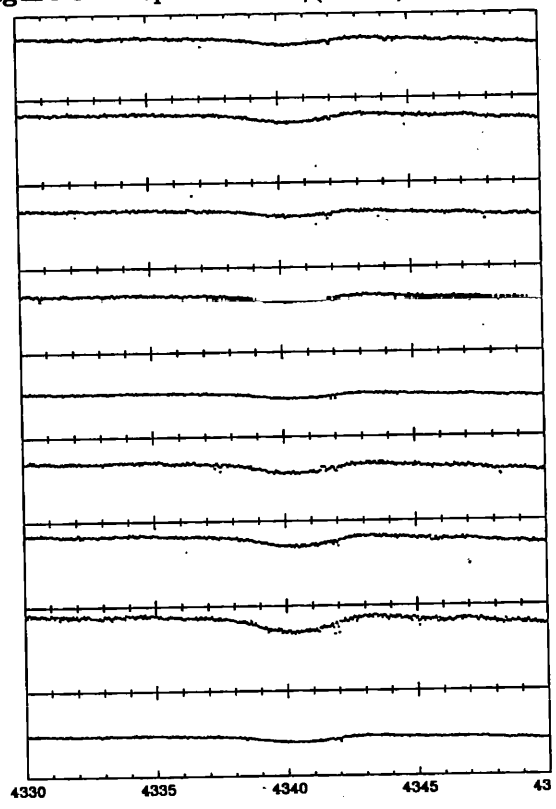

Figure 3.43 Spectra for Hγ(4340Å) second half 18th Feb 1996.

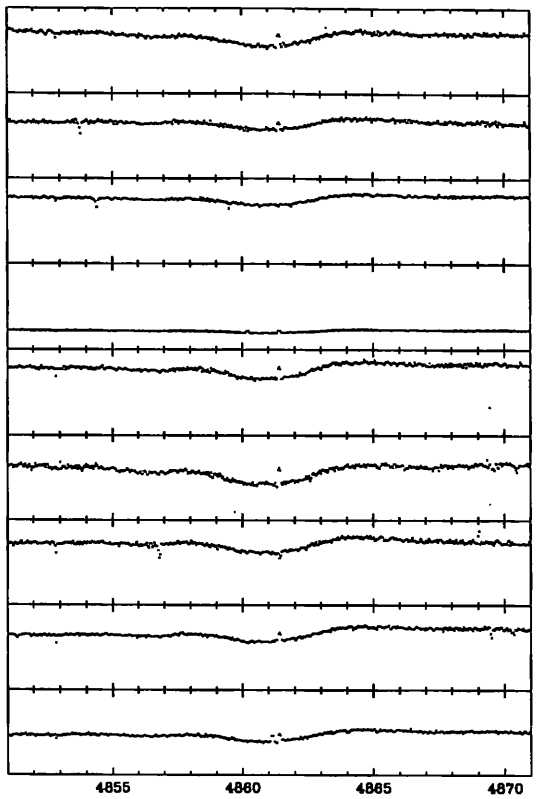

Figure 3.44 Spectra for Hβ(4861Å) first half of 18th Feb 1996.

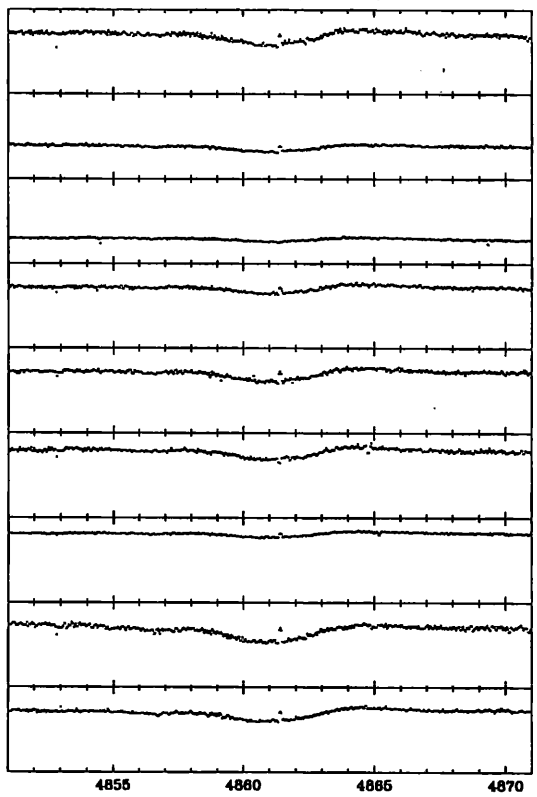

Figure 3.45 Spectra for Hβ(4861Å) second half of 18th Feb 1996.

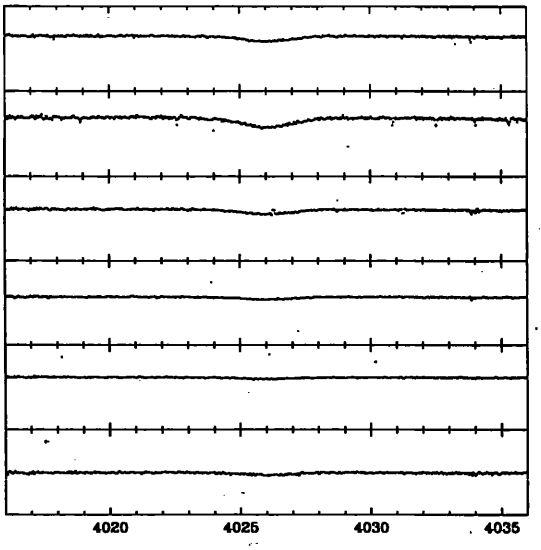

Figure 3.46 Spectra for HeI(4026Å) 19th Feb 1996.

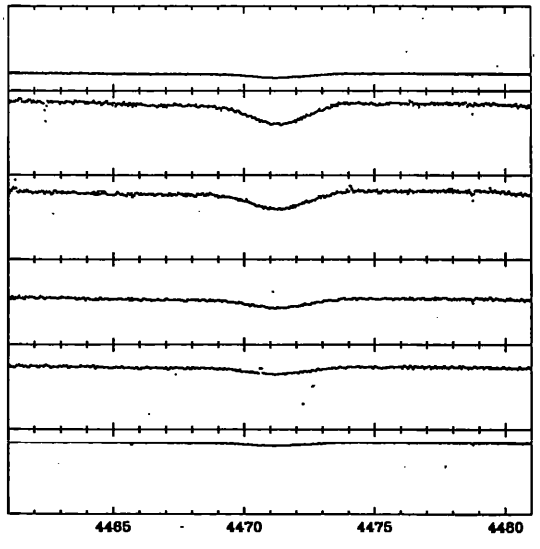

Figure 3.47 Spectra for HeI(4471Å) 19th Feb 1996.

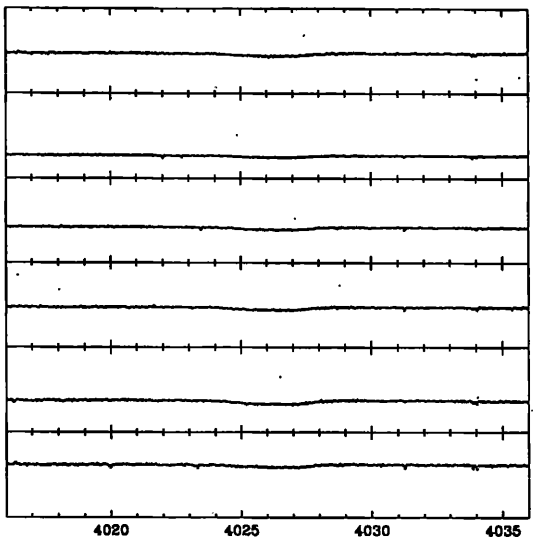

Figure 3.50 Spectra for HeI(4026Å) 20th Feb 1996.

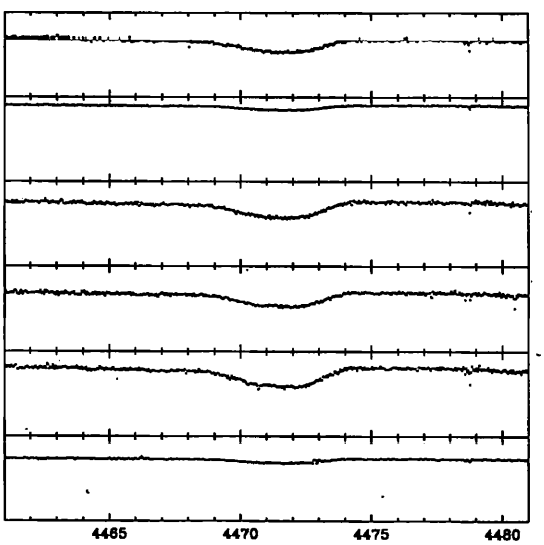

Figure 3.51 Spectra for HeI(4471Å) 20th Feb 1996.

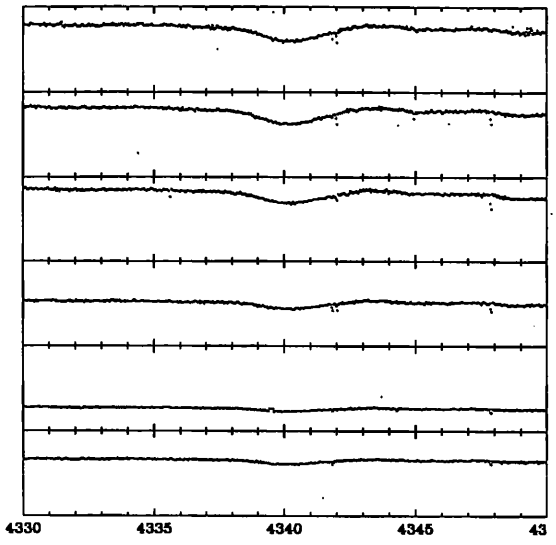

Figure 3.48 Spectra for Hγ(4340Å) 19th Feb 1996.

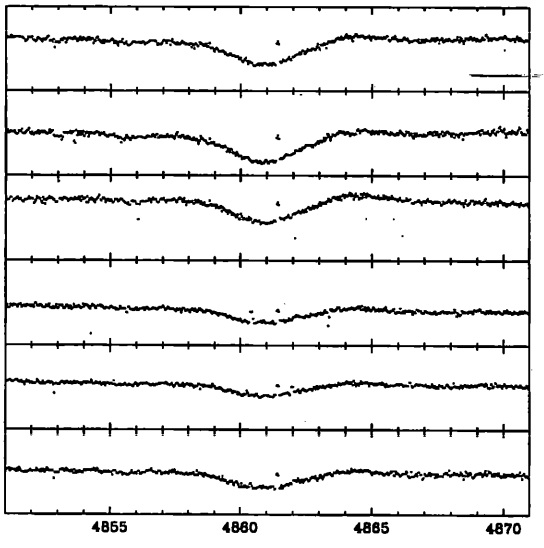

Figure 3.49 Spectra for Hβ(4861Å) 19th Feb 1996.

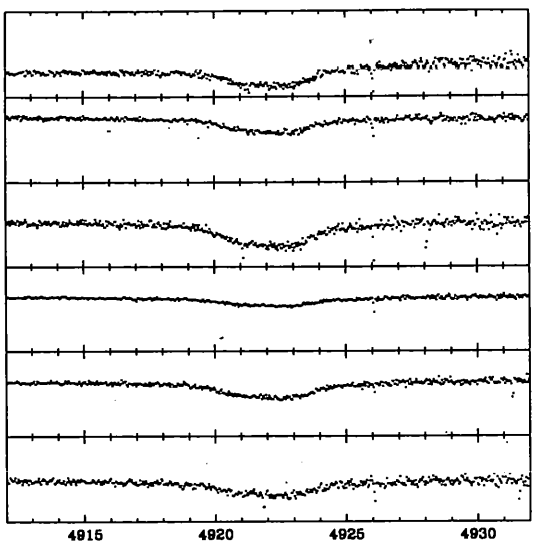

Figure 3.52 Spectra for HeI(4922Å) 20th Feb 1996.

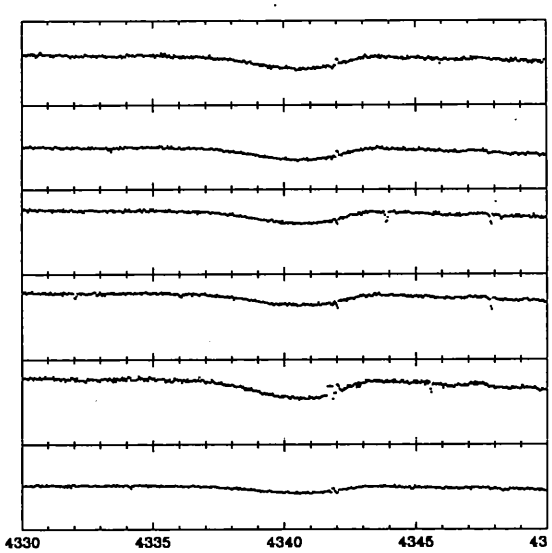

Figure 3.53 Spectra for Hγ(4340Å) 20th Feb 1996.

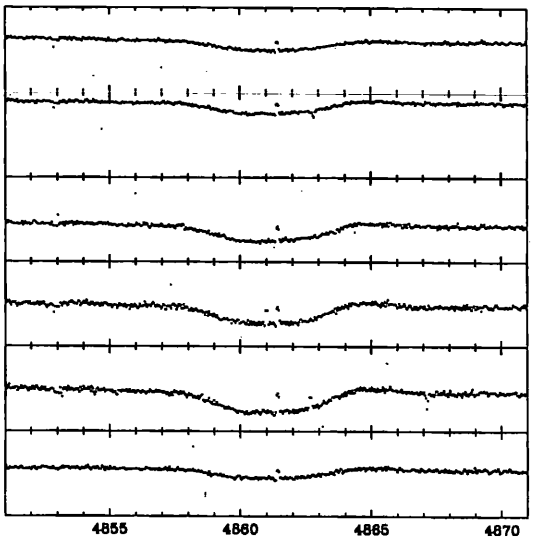

Figure 3.54 Spectra for Hβ(4861Å) 20th Feb 1996.

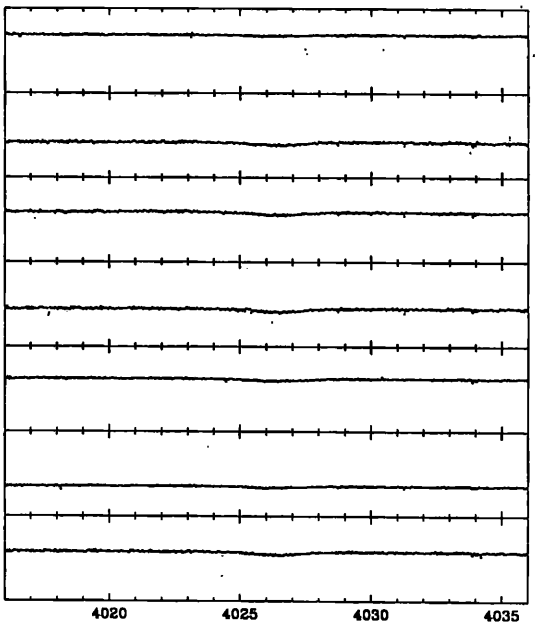

Figure 3.55 Spectra for HeI(4026Å) 21st Feb 1996.

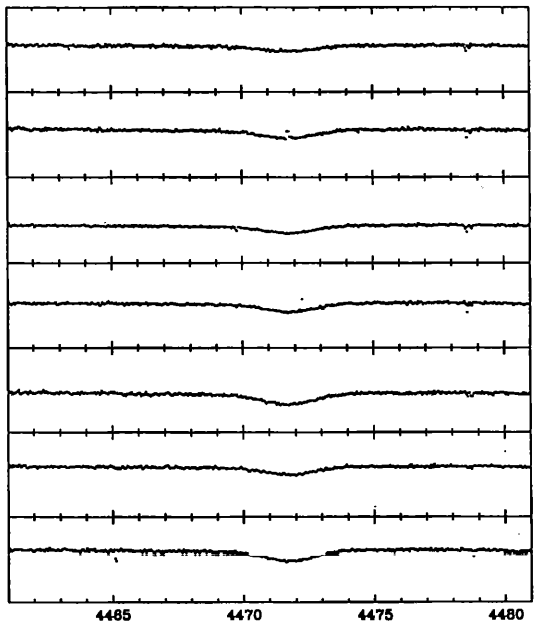

Figure 3.56 Spectra for HeI(4471Å) 21st Feb 1996.

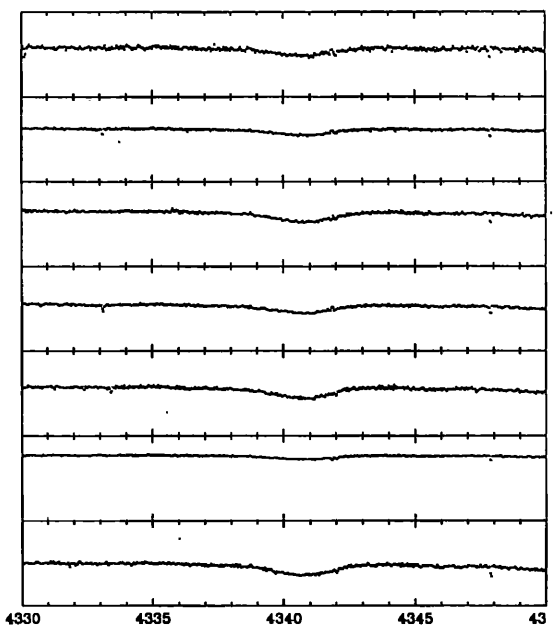

Figure 3.57 Spectra for Hγ(4340Å) 21st Feb 1996.

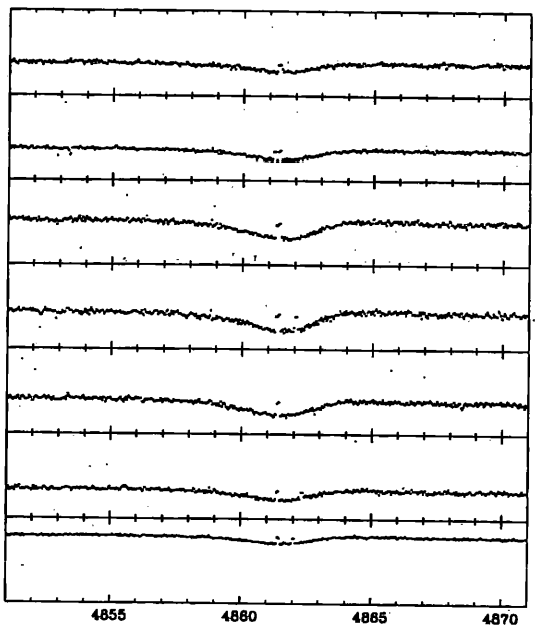

Figure 3.58 Spectra for Hβ(4861Å) 21st Feb 1996.

Chapter 4

Radio Observations of the Bow Shock Around Vela X-1

"They told me that you had gone totally insane and that your methods were unsound."

"Are my methods unsound?"

"I don't see any method at all, sir."

Martin Sheen and Marlon Brando; Apocalypse Now

4.1 Summary

This chapter deals with radio observations of the bow-shock around Vela X-1 using the Australia Telescope Compact Array. The motivation for this work is described, and although no radio emission was detected, the resulting conclusions are discussed.

4.2 Introduction

OB runaways are OB stars which are observed to have large space velocities, and appear to have travelled away from an OB association, in some cases well away from the Galactic plane, unusual for such short-lived stars. They also often have relatively high He abundances and/or rotational velocities (van Rensbergen et al 1996). Additionally, around a third of OB runaways are associated with bowshock structures which are caused by the interaction of the runaway's strong stellar wind with the interstellar medium (van Buren et al 1995).

Two main scenarios, the supernova hypothesis and the cluster ejection mechanism have been proposed to explain their origin.

Figure 4.1 Hα map of area around Vela X-1, showing bowshock.

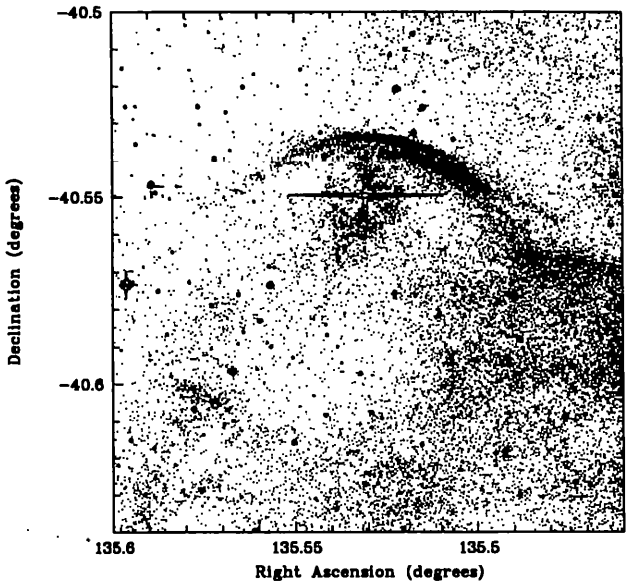

4.2.1 The Supernova Hypothesis

If the OB runaway had originally been the less massive member of a binary system, and its more massive companion had undergone a supernova explosion, this sudden release of energy could have imparted a large velocity to the more slowly evolving star, and transformed it into an OB runaway (Blaauw 1961). As we saw in Chapter 1, the evolution of close binaries often includes a period of mass transfer from the more massive star to its less massive companion. This means when the originally more massive star goes supernova, less than half the total system mass will be lost, and the system is likely to remain bound and receive a kick velocity. The remaining OB star will appear as an OB runaway.

Although searching known OB runaways for compact companions has been unsuccessful, there is some circumstantial evidence for the supernova hypothesis. It predicts that the mass transfer phase will transfer nuclear fusion products (ie He), and angular momentum onto the less massive star, causing it to display an enhanced He abundance, and increasing the rotational velocity. This agrees with the observed properties of OB runaways (see, for example Kaper et al 1997a).

4.2.2 The Cluster Ejection Mechanism

First proposed by Poveda et al (1967), this scenario suggests the runaways were ejected from their parent clusters via dynamical interaction during the cluster's early evolutionary stages.

This mechanism for the production of OB runaways is supported by the lack of observational evidence for runaways with compact companions, and the existence of two double-lined spectroscopic binaries, HD3950, and HD198846, whose origin cannot be explained using the supernova hypothesis (Gies & Bolton 1986).

4.3 A Bowshock Around Vela X-1

The supernova hypothesis received a boost when Kaper et al (1997a) discovered a bowshock around Vela X-1 (see Figure 4.1). As we saw above, bowshocks are a common feature of OB runaways, but this was the first time such a feature had been observed around a HMXRB. The bowshock demonstrated that Vela X-1 was moving with a supersonic velocity with respect to the interstellar medium, and so was a runaway. Additionally, from the symmetry of the bowshock, Kaper et al (1997a) determined the direction along which Vela X-1 had travelled. This path was consistent with the OB assocation, Vel OB1, being the parent association of Vela X-1. Instead of finding a compact companion around an OB runaway, Kaper et al (1997a) had shown that an OB star known to have a compact companion (which must have undergone a supernova explosion), was also a runaway.

Vela X-1 is the only HMXRB that has been shown to be an OB runaway, but it is thought that all HMXRBs are runaway systems. Based on the work of Van Buren et al (1995), who showed that around a third of OB runaways have an associated bowshock, Kaper et al (1997a) predict that at least a third of HMXRBs will exhibit bowshocks.

Chevalier & Ilovaisky (1998) claim that proper motion measurements made using the Hipparcos satellite do not support the conclusion that Vela X-1 could have originated from Vel OB1. However, they do not take into account that Vela X-1 changes position relative to Vel OB1 due to differential galactic rotation. When this is corrected for, the Hipparcos data actually confirm Kaper et al's original result (Kaper 1998).

4.4 Theoretical levels of radio emission from the bowshock

In order to decide if an attempt to detect radio emission from the bowshock was feasible, it was necessary to make some sort of estimate of the expected flux. A rough estimate of the bowshock's expected radio flux can by made by utilising the following equation for the free-free radio emision from the stellar wind of an early type star, derived from Wright &

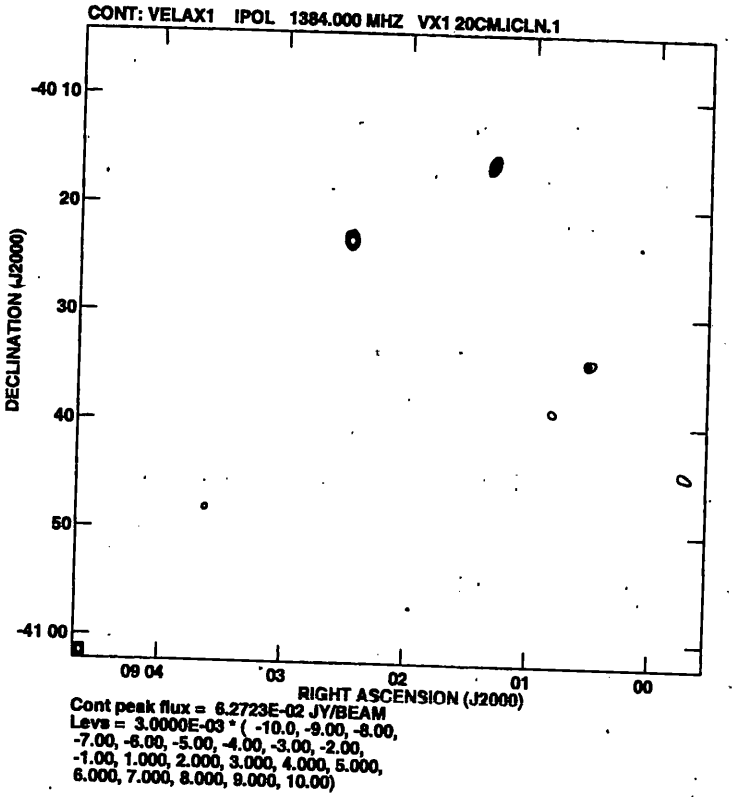

Figure 4.2 20cm map of region around Vela X-1.

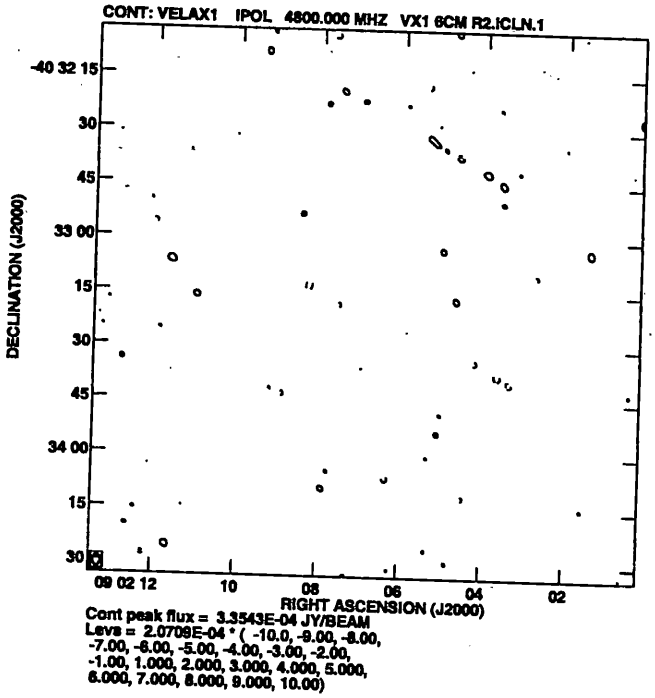

Figure 4.3 6cm map map of region around Vela X-1.

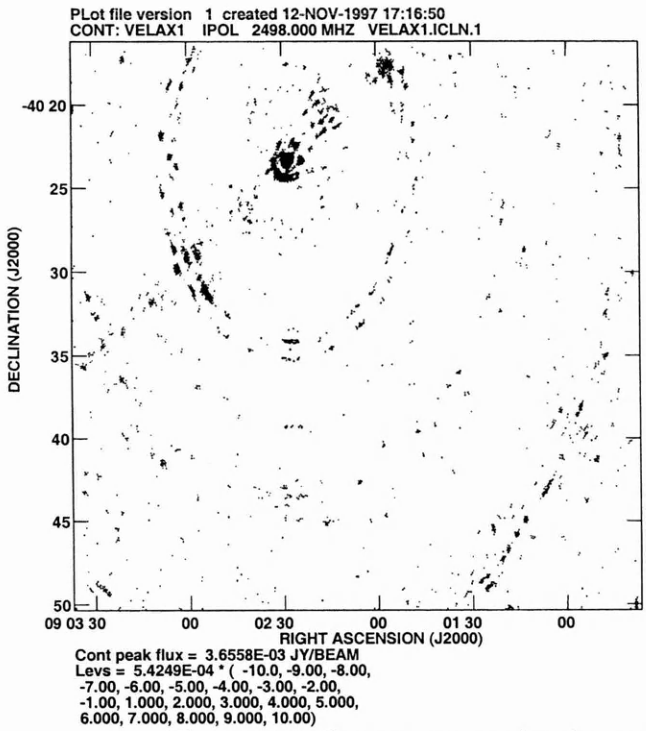

Figure 4.4 13cm map map of region around Vela X-1.

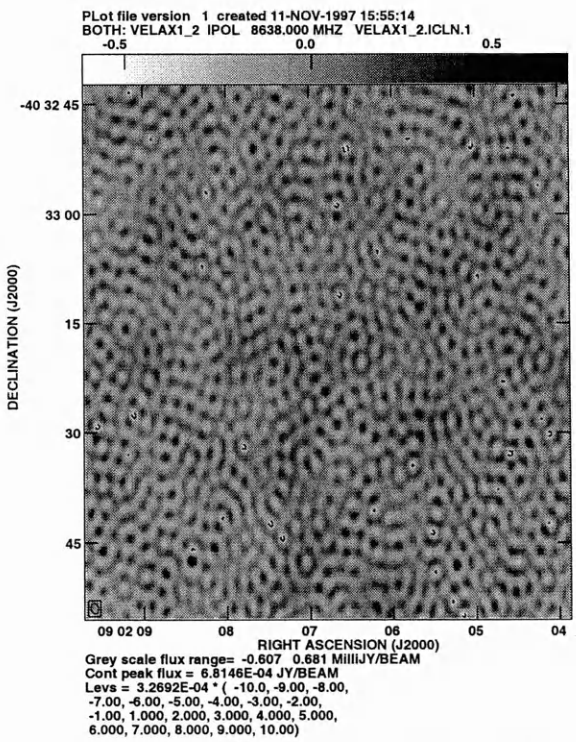

Figure 4.5 3cm map map of region around Vela X-1.

Table 4.1 Flux estimates and 3σ noise levels for the four wavelengths.

Wavelength	3 cm	6 cm	13 cm	20 cm
Flux estimate	19 μJy	13 μJy	8.3 μJy	5.7 μJy
Noise level	327 μJy	207 μJy	542 μJy	3000 μJy

Barlow (1975):

$$S_{\upsilon}^{\frac{3}{4}} = \frac{\dot{M}\upsilon^{\frac{1}{2}}G^{\frac{1}{2}}\gamma^{\frac{1}{2}}Z}{0.095\mu v_{\infty}D^{\frac{3}{2}}} \tag{4.1}$$

where S_{υ} is the radio flux in Jy, $\dot{M}$ is the mass loss in $M_{\odot}$/year, υ is the frequency in Hz, G is the Gaunt factor, v_{∞} is the terminal wind velocity in km/s, and D is the distance to the system in kpc. Assuming $\dot{M} = 10^{-6}$ (Dupree et al 1980), $G = 1$ (Böhm-Vitense 1989), $\gamma = 1$, $Z = 1$, $\mu = 1.26$ (Wright & Barlow 1975), $v_{\infty} = 1100$ (Prinja et al 1990), and D=1.8, (Sadakane et al 1985) we obtain the flux estimates in Table 1.

These flux levels would be undetectable using current technology. However, it was hoped that the piling-up of stellar wind and interstellar material at the bowshock would produce a much higher density for the incoming stellar wind particles to interact with. This could lead to a significantly higher, and potentially detectable, flux from this region.

4.5 Observations

Observations were made using the Australia Telescope Compact Array (ATCA), situated outside Narrabri in New South Wales, Australia. This facility comprises of six steerable radio dishes, five of which are mounted on a 3km east-west railway track, with the sixth dish 3km to the west (various authors, 1992). The optical position of Vela X-1 (together with a number of flux and phase calibrators) was observed for 12 hours for each of the four frequencies available at ATCA: 3, 6, 13, and 20 cm.

4.6 Analysis and Results

The data reduction and mapping were performed using AIPS (Greisen 1995). Unfortunately, the resulting maps (see Figures 4.2-4.5) show no radio emission from the bowshock above the 3σ noise levels given in Table 1.

4.7 Conclusions

Upper limits of 327μJy at 3cm, 207μJy at 6cm, 542μJy at 13cm, and 3000μJy were obtained for the bowshock's radio emission. Although a radio counterpart to the bowshock around Vela X-1 was not detected, these upper limits may allow constraints to be placed on the density of the shocked gas. Hydrodynamical simulations can be used to make predictions of the densities and velocities involved (Comerón & Kaper 1998, Kaper et al 1997b), which in turn can be fed into an emission model to predict the expected radio flux. Hopefully, these calculated fluxes will be compatible with the upper limits we have observed.

Chapter 5

Conclusions and future work

"There is one more thing ... it's been emotional."

Vinny Jones; Lock, Stock, and Two Smoking Barrels

5.1 Aims

When the work for this thesis was begun in October 1995, the eventual aim was somewhat ill-defined. Essentially, the plan was to observe two well-known systems with modern equipment and attempt to glean new and useful information about them. The first part of this has undoubtably been achieved, in that observations have been made of two high-mass X-ray binary systems, Cen X-3 (at optical wavelengths - Chapter 2) and Vela X-1 (at optical - Chapter 3, and radio wavelengths - Chapter 4). The information obtained can be summed up in a single sentence: the masses of the neutron stars in Cen X-3 and Vela X-1 are $1.21 \pm 0.21 M_{\odot}$, and $1.77^{+0.55}_{-0.29} M_{\odot}$ respectively, while the Vela X-1 bowshock does not emit detectable amounts of radio waves. In the following sections, I will attempt to summarise the conclusions reached in each chapter, and suggest avenues for future work.

5.2 Cen X-3

The great difficulty of these observations is illustrated by the fact that in the end, most of the data that had been gathered for this system was regarded as at best highly suspect, and at worst completely useless. Despite this, a value for the semi-amplitude of the radial velocity variation of the optical component, K_o=24.4±4.1kms^{-1} was obtained. When combined with existing X-ray data (Nagase et al 1992), a value of $20.5 \pm 0.7 M_{\odot}$ was calculated for the mass of the optical component, and a value of $1.21 \pm 0.21 M_{\odot}$ for the mass of the neutron star.

The inclination of the plane of the orbit to the line of sight was found to be $70^o.2 \pm 2^o.7$. This value for the mass of the neutron star has a smaller uncertainty than, but is consistent with that of Clark et al (1998) who quoted a value of $1.23 \pm 0.60 M_\odot$. Both values are also consistent with the canonical neutron star mass of $1.4 M_\odot$. It was also demonstrated that the sort of radial velocity measurement we made can be badly affected by variable stellar wind. One suggestion for future work would involve the construction of a more complete radial velocity curve. However, due to the 2 day orbital period, this would be difficult from a single site. Perhaps a coordinated multi-observatory campaign, Antarctic or space-based observations could overcome this. Work on modelling how wind variability affected observed radial velocities could also aid understanding of the system.

5.3 Vela X-1

An enormous amount of data was collected for this system, allowing an almost complete radial velocity curve to be constructed. A value of $20.4 \pm 1.8 \mathrm{kms}^{-1}$ was obtained for the semi-amplitude of the radial velocity variation of the optical component. When combined with existing X-ray data (Deeter et al 1987, Watson & Griffiths 1987), a value of $23.6^{+5.5}_{-2.0} M_\odot$ was calculated for the mass of the optical component, and a value of $1.77^{+0.55}_{-0.29} M_\odot$ for the mass of the neutron star. The inclination of the plane of the orbit to the line of sight was found to be 77^{o+13}_{-12}. This value for the mass of the neutron star is significantly larger than the canonical neutron star mass of $1.4 M_\odot$, and compatible with van Kerkwijk's 1995 value of $1.9^{+0.7}_{-0.5} M_\odot$. However, there are a number of potential sources of error, not least of which is the effect of the varying gravitational force exerted by the neutron star on the supergiant, on the consequences for the observed radial velocities. I would suggest that a theoretical exploration of this would help confirm or deny the apparently anomalous neutron star mass. If the neutron star mass is confirmed, we will be confronted with a system that is doubly unique in that it contains a unusally massive neutron star, and has a significant orbital eccentricity.

5.4 Radio counterpart to Vela X-1 bowshock

Richard Ogley and myself were privileged to be the first people to observe the Vela X-1 bowshock at radio wavelengths. Unfortunately, no radio counterpart to the Vela X-1 bowshock was detected. However, upper limits were obtained at four frequencies, and these may be useful for future modelling of the bowshock emission. Comerón & Kaper (1998)

have performed a series of semi-analytical simulations of bowshocks, and possible avenue for future work would be to extend these simulations to investigate the level of any radio emission.

Chapter 6

References

Ash et al, 1998, in "Neutron stars and pulsars, thirty years after the discovery", ed. Shibazaki et al (Tokyo: Universal Academy Press), p.511-514

Ash et al, 1999, MNRAS, accepted

Aslanov, & Cherepashchuk, 1982, Sov Astron, 26(2), 177

Barnes, 1993, A Beginner's Guide to Using IRAF Version 2.10, NOAO

Bergeron et al, 1991, ApJ, 367, 253

Bevington et al, 1992, "Data Reduction and error analysis for the physical sciences", (New York: Mcgraw Hill)

Blaauw, 1961, Bull. Astron. Inst. Netherlands, 15, 265

Böhm-Vitense, 1989, "Introduction to stellar atmospheres: Vol 2", (Cambridge: Cambridge University Press), p.71

Comerón & Kaper, 1998, A&A, 338, 273

Boldt et al, 1969, Nature, 223, 280

Bolton, 1972, Nature, 235, 271

Bradt & McClintock, 1983, ARA&A, 21, 13

Braes & Miley, 1971, Nature, 232, 246

Brucato & Kristian, 1972, ApJ, 173, L105

Charles et al, 1976, "X-ray binaries", NASA SP-389, 629

Chevalier & Ilovaisky, 1998, A&A, 330, 201

Chitre & Hartle, 1976, ApJ, 207, 592

Chodil et al, 1967, Phys Rev Lett, 19, 681

Claret & Gimenez, 1993, A&A, 277, 487

Clark et al, 1988, ApJ, 324, 974

Deeter et al, 1987a, AJ, 93, 877

Deeter et al, 1987b, ApJ, 314, 634

Dupree et al, 1980, ApJ, 238, 969

Fishman et al, 1969, ApJ, 158, L61

Forman et al, 1973, ApJ, 182, L103

Friedman & Ipser, 1987, ApJ, 314, 594

Fritz et al, 1971, ApJ, 164, L55

Giacconi et al, 1962, Phys Rev Lett, 9, 439

Giacconi et al, 1967, ApJ, 148, L129

Giacconi et al, 1971, ApJ, 167, L67

Giacconi et al, 1972, ApJ, 178, 281

Gies & Bolton, 1986, ApJS, 61, 419

Glendenning, 1985, ApJ, 293, 470

Greisen (ed), 1995, AIPS Cookbook, NRAO

Heap & Corcoran, 1992, ApJ, 387, 340

Hecht, 1987, "Optics", (Reading: Addison-Wesley), p.428

Hewish et al, 1968, Nature, 217, 709

Hiltner et al, 1972, ApJ, 175, L19

Hjellming & Wade, 1971, ApJ, 168, L21

Horne, 1986, PASP, 98, 609

Hutchings et al, 1979, ApJ, 229, 1079

Kalogera & Baym, 1996, ApJ, 470, L61

Kaper, 1998, private communication

Kaper et al, 1997a, ApJ, 475, L37

Kaper et al, 1997b, ESO Messenger, 89, 28

Kreminski, 1974a, IAUC 2612

Krzeminski, 1974b, ApJ, 192, L135

Levine et al, 1991, ApJ, 381, 101

Levine et al, 1993, ApJ, 410, 328

Makishima et al, 1987, ApJ, 314, 619

Massey, 1992, A User's Guide to CCD Reductions with Iraf, NOAO

Mauder, 1975, ApJ, 195, L27

McClintock et al, 1976, ApJ, 206, L99

Mouchet, 1980, A&A, 90, 113

Nagase, 1992, ApJ, 396, 147

Oppenheimer & Volkoff, 1939, Phys Rev, 55, 374

Pandharipande, 1971, Nucl. Phys. A, 207, 298

Petro, 1975, ApJ, 195, 709

Poveda et al, 1967, Bol. Obs. Tonantzintla Tacubaya, 4, 860

Prinja et al, 1990, ApJ, 361, 607

Rappaport et al, 1971, ApJ, 168, L17

Rappaport & McClintock, 1975, IAUC 2833

Rappaport et al, 1976, ApJ, 206, L103

Rappaport et al, 1980, ApJ, 235, 570

Rappaport & Joss, 1983, in "Accretion-Driven Stellar X-Ray Sources", ed. Lewin & van den Heuvel (Cambridge: Cambridge Univ. Press)

Reynolds, 1991, PhD thesis, University of St Andrews

Reynolds et al, 1992, MNRAS, 256, 631

Reynolds et al, 1993, MNRAS, 261, 337

Reynolds et al, 1997, MNRAS, 288, 43

Rhoades & Ruffini, 1974, Phys Rev Lett, 32, 324

Rubin et al, 1996, ApJ, 459, 259

Sadakane et al, 1985, ApJ, 288, 284

Salgado et al, 1994, A&A, 291, 155

Sandage et al, 1966, ApJ, 146, 316

Schreier et al, 1972, ApJ, 172, L79

Shortridge & Meyerdierks, 1996, Starlink User Note 86.11, Starlink project

Stickland & Lloyd, 1993, MNRAS, 264, 935

Stickland et al, 1997, MNRAS, 286, L21

Tananbaum et al, 1972, ApJ, 174, L143

Thorsett et al, 1993, ApJ, 405, L29

Thorsett, 1997, Phys Rev Lett, 77, 1432

Thorsett & Chakrabarty, 1999, ApJ, submitted

Tinney, 1996, AAO Observers's Guide 5th (HTML) edition, AAO Observatory (http://-www.aao.gov.au/local/www/cgt/obsguide/obsguide.html)

Tonry & Davis, 1979, AJ, 84, 1511

Tsunemi, 1989, PASJ, 42, 453

Tsunemi et al, 1996, ApJ, 456, 316